THE EFFECTS OF DIATOM SHAPE AND HEAT TREATMENT ON THE MECHANICAL PROPERTIES OF DIATOM-FRUSTULE-FILLED POLYMERIC MATRIX COMPOSITES

A Thesis Submitted to
the Graduate School of Engineering and Sciences of
İzmir Institute of Technology
in Partial Fulfillment of the Requirements for the Degree of

MASTER OF SCIENCE

in Materials Science and Engineering

by
Doğuş ZEREN

December, 2012
İZMİR

We approve the thesis of **Doğuş ZEREN**

Examining Committee Members:

Prof. Dr. Mustafa GÜDEN
Department of Mechanical Engineering
İzmir Institute of Technology

Assoc. Prof. Dr. Mustafa M. DEMİR
Department of Chemistry
İzmir Institute of Technology

Assoc. Prof. Dr. Uğur MALAYOĞLU
Department of Metallurgical and Materials Engineering
Dokuz Eylül University

14 December 2012

Prof. Dr. Mustafa GÜDEN
Supervisor, Department of Mechanical Engineering
İzmir Institute of Technology

Prof. Dr. Atakan SUKATAR
Co-Supervisor, Department of Biology, Ege University

Assoc. Prof. Dr. Mustafa M. DEMİR
Head of the Department of
Materials Science and Engineering

Prof. Dr. R. Tuğrul SENGER
Dean of the Graduate School of
Engineering and Sciences

ACKNOWLEDGEMENTS

I would like to thank and express my sincere gratitude to Prof. Dr. Mustafa GÜDEN and Prof. Dr. Atakan SUKATAR for their valuable advice, patience, motivation, effort and immense knowledge on my thesis. It was a pleasure for me to study under their supervising and guidance.

I gratefully thank to my colleagues, Umut SAVACI, Yiğit ATTİLA, Ali KARA, Kutlay ODACI, Cenk KILIÇASLAN, Kıvanç TURAN, Levent Yurdaer AYDEMİR, and Kutsal KESİCİ for their endless support and help. I would like to thank to my roommates, Eren UÇAR and Tuhfe GÖÇMEN, for their friendship, patience and support. I would like to thank to Asst. Prof. Dr. Elif Aras GÜLTÜRK for her help and guidance. Also I would like to thank to the IYTE-MAM and IYTE-BIYOMER employees.

I would like to thank to my family: my parents Ahmet ZEREN, Yasemen ZEREN and my brother Ege ZEREN, without their everlasting support and encouragement, I would never be as I am.

Last but absolutely not least, I would like to thank to a very special person, Esra TOPEL, for her huge support, patience and providing motivation during my thesis. I would like to thank to everyone who helped me during this thesis.

ABSTRACT

THE EFFECTS OF DIATOM SHAPE AND HEAT TREATMENT ON THE MECHANICAL PROPERTIES OF DIATOM-FRUSTULE-FILLED POLYMERIC MATRIX COMPOSITES

The effects of diatom frustule shape and heat treatment process on the compressive mechanical properties of an epoxy matrix were experimentally investigated. Different pennate diatoms reduced to exclusive species by isolating and culturing were used as filler in the epoxy matrix. A commercial diatomite was heat treated between 600^{o}C and 1200^{o}C to increase the crystallinity. Filling epoxy matrix with ~6 wt% of natural commercial diatomite and *Achnanthes taeniata* frustule increased the compressive strength from 60 MPa to 67 MPa and 79 MPa, respectively. A higher strengthening, ~10 MPa, and moduli with *Achnanthes taeniata* frustule addition was found. The heat treatment of natural diatomite frustules at 1000^{o}C increased both compressive strength and stress values of the epoxy matrices. The compressive strength increased from 60 to 90 MPa with the heat-treatment process, providing 50% of increase in the compressive strength of neat epoxy.

ÖZET

DİYATOM FRİSTÜL KATKILI POLİMERİK MATRİSLİ KOMPOZİTLERİN MEKANİK ÖZELLİKLERİNDE DİYATOMLARIN ŞEKİL VE IŞIL İŞLEM ETKİLERİ

Diyatome fristülü şeklinin ve ısıl işleminin epoksinin basma mukavemeti üzerindeki etkileri belirlenmiştir. İzole edilerek ve kültür ortamında çoğaltılarak tek türe indirgenmiş farklı türdeki pennat diyatomeler epoksi matriste katkı malzemesi olarak kullanılmıştır. Ticari bir diyatomit, kristalizasyon derecesi artırtılmak için 600^{o}C ve 1200^{o}C arasında ısıl işleme tabi tutulmuştur. Epoksi matrisin ağırlıkça ~%6 oranında doğal diyatomit ve *Achnanthes taeniata* fristülü katkısı basma mukavemetini 60 MPa' dan sırasıyle 67 MPa ve 79 MPa' ya yükseltmiştir. Daha yüksek bir mukavemet (~10 MPa) ve elastizite modülü artışının *Achnanthes Taeniata* katkısı ile sağlandığı bulunmuştur. Doğal diyatomitin 1000^{o}C'deki ısıl işlemi epoksi matrisin basma mukavemetini artırmıştır. Katkısız epoksinin basma mukavemeti bu ısıl işlem ile %50 artış sağlayarak 60 MPa'dan 90 MPa'ya yükselmiştir.

TABLE OF CONTENTS

LIST OF FIGURES

LIST OF TABLES

CHAPTER 1

INTRODUCTION

Polymers are widely chosen materials for a wide range of engineering applications due to their relatively low production cost and ease of processing. However, the relatively low strength compared to metals limits their applicability. To reach modified properties, different types of reinforcing materials are added into polymers. The most commonly used reinforcements include glass fibers, carbon/graphite fibers, organic fibers, boron, silicon carbide, fabrics, particles and whiskers. In recent years, natural reinforcements have taken considerable interest due to their abundance in nature, non-harmful processing parameters, being inexpensive, renewable and exhaustible resource and their good physical properties such as low density, good thermal properties and high specific strength. There are several studies on the use of using natural reinforcements in polymer matrices, including wood flour and fibers [1], lignocellulose fibers [2], flax [3], sisal [4], hemp fibers [5]. Generally, these reinforcements are used for enhancing the mechanical properties of polymers.

The expected features of reinforcements in polymer matrices are property modification or enhancement, no chemical reaction between filler and matrix, good filler/matrix adhesion, high surface area to volume ratio and lowering the cost of materials by replacing the more expensive material. Diatom frustules being silica based material have intricate morphology and the high surface area/volume ratio. They have small size, porous structure and very rough surface associate the high surface area. Thus, they may be used as the reinforcement in polymer matrices. In addition, regularly arranged micron or nano-sized pores on the walls of the frustules can provide the matrix penetration inside the wall and fulfill the good filler/matrix adhesion as a result of mechanical gripping. These potentials are the motivation of using diatom frustules for reinforcing material in polymers.

In the present study, the effect of diatom frustule shape and heat treatment on the compressive mechanical properties of epoxy was determined. For that, diatoms were reduced to exclusive species by isolating and culturing. Pennate diatoms, in fiber geometry of various aspect ratios, were used as filler. In the second part, the effect of heat treatment on the mechanical properties was investigated. For that, a commercial diatomite was heat treated at different temperatures to increase the crystallinity.

The content of the thesis is as follows: Chapter II summarizes polymer matrix composites and explains the importance of using natural reinforcements in polymer matrices generally. In Chapter III, the types and structures of diatoms and frustules are explained. Materials and testing methods are given in Chapter IV. Chapter V is the results and discussions. Conclusions are made in Chapter VI.

CHAPTER 2

POLYMER MATRIX COMPOSITES AND THEIR REINFORCEMENTS

Composite materials are composed of two different materials with macroscopically distinct properties. The matrix holds and transforms the load to the reinforcement and the reinforcement bears the load. Matrices and reinforcements can be made from polymers, ceramics or metals. The reinforcements may be in either fiber, particle or whisker form. Composites are categorized according to their matrix type as polymer, ceramic and metal matrix composites [6].

In early history, combinations of different materials were used in some structural applications. For example, mud bricks reinforced with straw were used in Egypt for creating building blocks. Asphalt mortars were engaged to joint bricks [7]. In Ancient Egypt, mummies were enfolded in linen cloth saturated with Dead Sea Salts, natural resins and honey in order to prevent the corruption of the body of the mummy [8]. Laminated metal composites were found in the Great Pyramid in 1837 [9]. The earliest man-made composite material is the concrete, a composite material which is widely used. While, the wood is the most known natural composite consisting of cellulose fibers in a lignin matrix [10].

Modern applications of composites have appeared in 1930s. Plastics such as vinyl, polystyrene, phenolic and polyester were developed in early 1900s. Nevertheless, plastics did not provide enough strength for structural applications. After the invention of glass fiber (also known as fiberglass, shown in Figure 2.1) in 1935, plastics were reinforced with fiberglass and the new resultant material was found to be stronger and at the same time lightweight. This development may be considered as the beginning of composite technology [11]. Today, composite materials are used in aircraft, aerospace, military, corrosion-resistant equipment processing, electric/electronic, marine equipment and biotechnology areas. The use of composites in the Boeing 757 aircraft is shown in Figure 2.2.

Figure 2.1. Glass fibers [12].

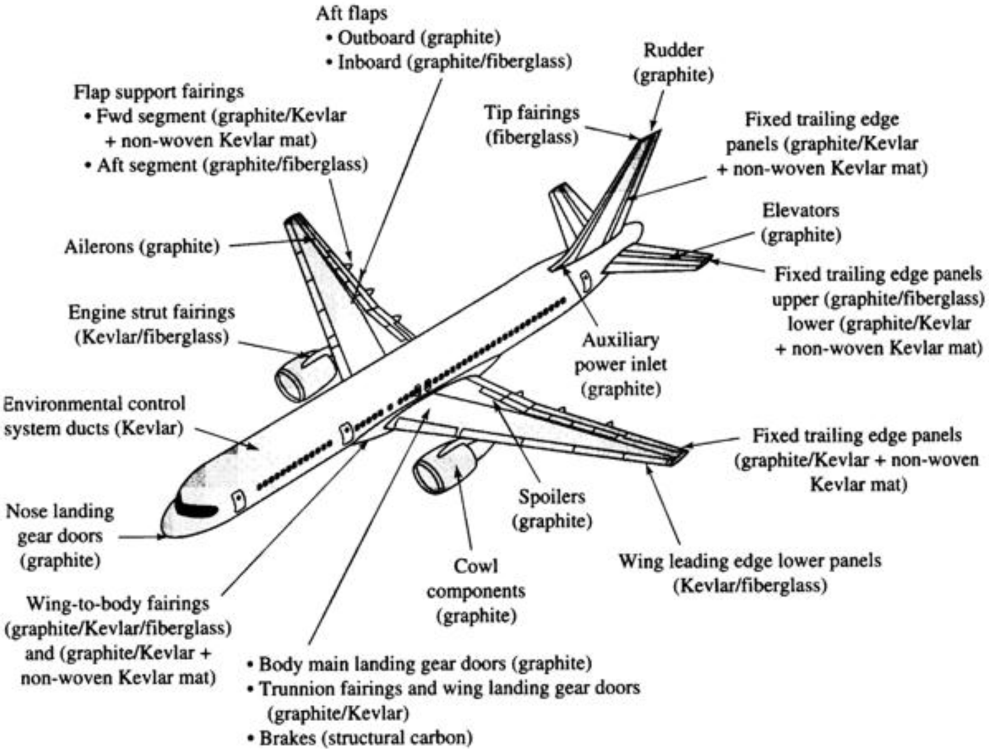

Figure 2.2. Composite parts in the Boeing 757-200 aircraft [13].

2.1. Polymer Matrix Composites

Polymer matrix composites are one of the most commonly used composite materials by the industry. Their production cost is relatively low and the production route is comparably easy. As the polymers are limited by their mechanical properties, such as relatively low strength and low impact resistance, reinforcements are added to the polymer matrices to increase the mechanical performance [14]. Essentially, polymers are divided into two groups: thermoplastics and thermosets. The main difference between thermoplastics and thermosets lies in their intermolecular structures. Thermoset are cross-linked and therefore burn rather than melting upon heating to elevated temperatures. The cross-linking is accomplished by heating and curing. On the other side, thermoplastic materials are linear polymers and can be re-melted and re-shaped by heating. The most common used thermosets include epoxy, polyester, phenolic resins and polyurethane. The most common thermoplastics are polyethylene, nylon, polypropylene, acrylic and polyvinyl chloride (PVC). The physical properties of typical thermoplastic and thermosetting polymers used in composite fabrication are tabulated in Table 2.1 and Table 2.2 respectively. As is seen in the same tables, thermosets have higher tensile strength and modulus than thermoplastics. Epoxy group of thermosets polymers are preferred matrices for fiber reinforcement as they have high specific strength, good adhesion properties, low shrinkage, and good corrosion protection [6].

Table 2.1. Physical properties of typical thermoplastic polymers used in composite fabrication [15]

Property	**PP**	**LDPE**	**HDPE**	**PS**	**Nylon 6**	**Nylon 6.6**
Density (g/cm^3)	0.899-0.920	0.910-0.925	0.94-0.96	10.4-1.06	1.12-1.14	1.13-1.15
Water Absorbtion-24h (%)	0.01-0.02	<0.015	0.01-0.2	0.03-0.10	1.3-1.8	1.0-1.6
Tg (°C)	-10 to 23	-125	-133 to -100	N/A	48	80
Tm(°C)	160-176	105-116	120-140	110-135	215	250-269
Heat deflection Temp (°C)	50-63	32-50	43-60	Max.220	56-80	75-90
Coefficient of thermal expansion (mm/mm/ °Cx10^5)	6.8-13.5	10	12-13	6-8	8-8.86	7.2-9
Tensile Strength (MPa)	26-41.4	40-78	14.5-38	25-69	43-79	12.4-94
Elastic Modulus (GPa)	0.95-1.77	0.055-0.38	0.4-1.5	4-5	2.9	2.5-3.9
Elongation (%)	15-700	90-800	2.0-130	1-2.5	20-150	35->300
Izod Impact Strength	21.4-267	>854	26.7-1068	1.1	42.7-160	16-654

Table 2.2. Physical properties of typical thermosetting polymers used in composite fabrication [15]

Property	**Polyester Resin**	**Vinyl Ester Resin**	**Epoxy**
Density (g/cm3)	1.2-1.5	1.2-1.4	1.1-1.4
Elastic modulus (GPa)	2-4.5	3.1-3.8	3-6
Tensile Strength (MPa)	40-90	69-83	35-100
Compressive Strength (MPa)	90-250	100	100-200
Elongation (%)	2	4-7	1-6
.Cure shrinkage (%)	4-8	N/A	1-2
Water Absorbtion-24h (%)	0.1-0.3	0.1	0.1-0.4
Izod Impact Strength (J/m)	0.15-3.2	2.5	0.3

2.2. Reinforcements for Polymer Matrices

Fiber reinforced composites are classified into two groups: short-fiber and continuous-fiber or long-fiber reinforced composites. Short fiber-reinforced composites are further divided into two groups: aligned short-fiber reinforced composites and randomly oriented short-fiber composites. Aligned short-fiber structures are highly anisotropic, while randomly oriented short-fiber structures are transversely isotropic or nearly isotropic depending on the fiber alignment in the 3rd axis.

Glass fibers, carbon fibers, aramid fibers and boron fibers are the most widely used reinforcements for polymer matrices [16]. There are mainly two types of glass fibers: E-glass and S-glass. The tensile strength of E-glass fiber is 3500 MPa, the Young Modulus is 80 GPa and the failure strain is about 5% [17]. S-glass fibers have higher mechanical strength than E-glass fibers as their structure is modified by silicate network. The tensile strength of S-glass fiber is 4600 MPa and the Young’s modulus is 90 GPa [17]. Few examples of glass fiber reinforced structural profiles with varying cross-sections are shown in Figure 2.3.

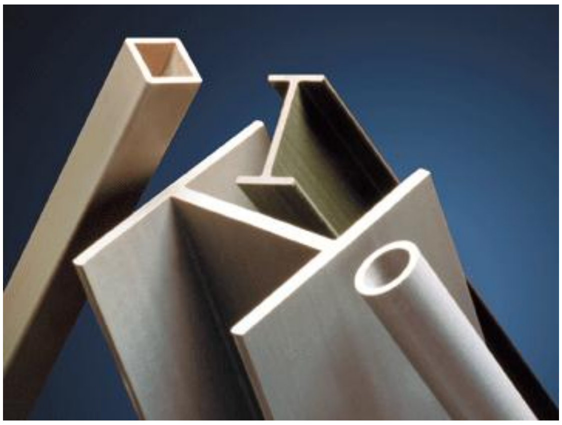

Figure 2.3. Glass fiber reinforced structural profiles [18].

High strength to weight ratio and high rigidity are the main properties of carbon fiber. Carbon fiber also provides good fatigue resistance to polymer matrices. Tensile strength of carbon fiber varies between 2000 to 7000 MPa and the Young’s modulus between 250 GPa to 550 GPa [17]. Carbon fiber is used for advanced applications including automobile racing parts, retrofitting in civil engineering, production of high-end sport equipment, aerospace engineering parts, mobile phone accessories, and musical instruments [17, 21]. Blackbird Guitars Company uses carbon fiber in their guitar productions. Carbon fiber provides better sound quality for guitars than wood material. The high strength of carbon fiber makes guitars very comfortable for travelling [22]. Some examples of carbon fiber reinforced polymer matrix composite products are shown in Figures 2.4(a-c).

(a) (b)

Figure 2.4. (a) Carbon fiber reinforced automobile engine cover [19] (b) Carbon fiber reinforced mobile phone case [20] (c) Carbon fiber reinforced Blackbird Guitars [21].

(cont. on next page)

(c)

Figure 2.4. (cont.)

The mechanical properties of aramid fibers are very much similar to those of glass fibers, except the elastic modulus is two times greater than glass fibers. Boron fibers have similar properties with carbon fibers and the elastic modulus can be five times greater than carbon fibers [17].

Particulate reinforcement addition of rigid particles to polymers both increases the stiffness and provides reduction in thermal expansion. Physical properties of resultant composite depend on the matrix, the reinforcement and the interfacial region between fiber and matrix. The mechanical properties of the particulate reinforced composites are affected by the size, shape, aspect ratio and distribution of the reinforcing particles in the matrix [22]. The experimental results have shown that the addition of short fiber form of silica increased the flexural and tensile strength of epoxy matric more than angular and spherical silica particles [23]. Carbon nanotubes are also used as reinforcement for polymers because of their high aspect ratio with a low density [24]. Carbon nanotubes with high aspect ratio were found to give additional increase in fracture toughness at higher filler contents [25].

The crystal structure of particles added into polymers is effective on the mechanical properties of resultant composites. In potassium titanate whisker, TiO_2 whisker and TiO_2 particle filled polytetrafluoroethylene composites, it was reported that different filler shapes did not affect the friction properties significantly but the crystal structure of filler affected the friction properties positively [26]. A similar result was shown for bioactive glass reinforcement in polysulfone matrices [27]. The reinforcing of crystallized silicate glass agents enhanced the mechanical properties more than the reinforcing of non-crystallized ones. Reinforcements used for polymers can be categorized as inorganic and organic as tabulated in Table 2.3 [28]. A further classification of the reinforcements is synthetic or natural.

Table 2.3. Categorization of Reinforcements used for polymers by their chemical family [29]

Chemical Family	**Examples**
Inorganics	
Oxides	Glass(fibers, spheres, flakes), MgO, SiO_2, Al_2O_3
Hydroxides	Al(OH)3, Mg(OH)
Salts	CaCO3, BaSO4, CaSO4, phosphates
Silicates	Talc, mica, kaolin, wollastonite, montmorillonite, nanoclays, feldspar
Metals	Boron, steel
Organics	
Carbon, graphite	Carbon fibers, graphite fibers and flakes, CNT, carbon black
Natural Polymers	Cellulose fibers, wood flour and fibers, flax, cotton, sisal, starch
Synthetic Polymers	Aramid, polyester, polyamide, polyvinyl alcohol fibers

2.3. Natural Reinforcements for Polymers

Environmental issues and need for more adaptable products of polymer based composites created a new research area of the reinforcement of polymers using natural particles or fibers [30]. The sources for the reinforcement include vegetables, animals and minerals. It is well known that the glass and glass fiber production requires a large amount of fossil fuels. Comparison between estimated non-renewable energy requirements for production of glass fibers and two natural fibers (flax fiber and China reed fiber) are tabulated in Table 2.4. The glass fiber, which is a synthetic fiber, requires 5-10 times more non-renewable energy than natural fiber production. Thus, it can be understood that production of synthetic fibers are damaging the environment more than production of natural fibers [31].

Table 2.4. Non-renewable energy requirements for production of different fibers (MJ/kg) [31]

Glass Fiber		**Flax Fiber**		**China Reed Fiber**	
Raw Materials	1.7	Seed production	0.05	Cultivation	
Mixture	1.0	Fertilizers	1.0	Transport plant	0.40
Transport	1.6	Transport	0.9	Fiber grinding	0.4
Melting	21.5	Cultivation	2.0	Transport fiber	0,26
Spinning	5.9	Fiber separation	2.7	Total	3.64
Mat production	23.0	Mat production	2.9		
Total	54.7	Total	9.55		

The most commonly used natural reinforcements for polymers include flax, hemp, jute, sisal, kenaf, coir, kapok, banana, henequen, corn stalk and grass fibers as depicted in Figure 2.5. The discrete advantages of natural fibers over glass fibers are further tabulated in Table 2.5 [32] and include low cost, low density, comparable specific tensile properties and low energy consumption for their production process, less health risk, renewability, recyclability and bio-degradability [15, 33].

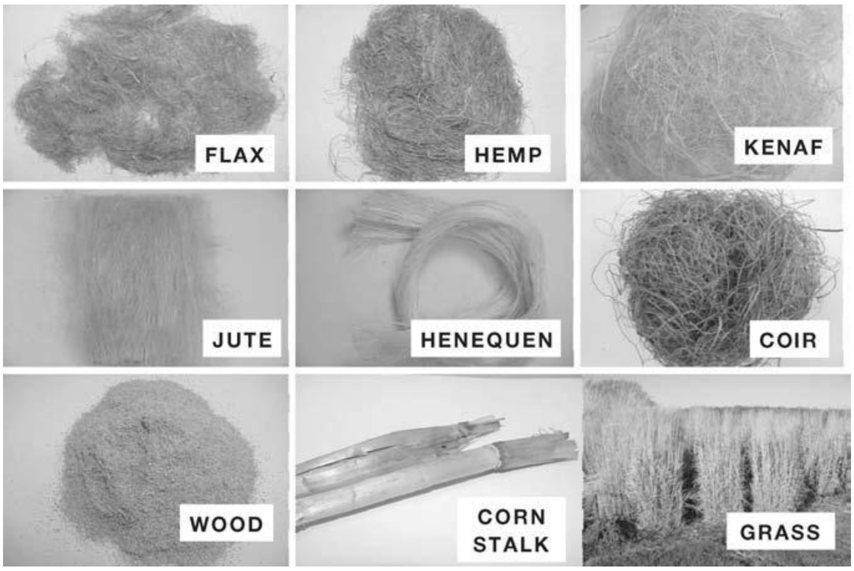

Figure 2.5. Photographs of some natural fibers and sources [33].

Table 2.5. Advantages of natural reinforcements over glass fibers [32]

Property	Natural fibers	Glass fibers
Density	Low	Twice that of natural fibers
Cost	Low	Low, but higher than NF
Renewability	Yes	No
Recyclability	Yes	No
Energy consumption	Low	High
Distribution	Wide	wide
CO_2 neutral	Yes	No
Abrasion to machines	No	Yes
Health risk when inhaled	No	Yes
Disposal	Biodegradable	Not biodegradable

The mechanical and physical properties of some selected natural and E-glass fibers are tabulated in Table 2.6. The specific strength and modulus of synthetic and natural fibers are further shown in Figures 2.6 (a) and (b), respectively [34]. It is noted in the same table and figures, some natural fibers have mechanical properties close to that of E-glass fiber. The main disadvantage of using natural reinforcements is the weak adhesion between reinforcement and matrix. Some chemical modifications have been applied to increase the bonding between fiber and matrix. Marais et al. [35] investigated the effect of plasma and autoclave treatment on the mechanical properties of flax fiber reinforced unsaturated polyester composites. The flax fibers were subjected to helium cold plasma and/or autoclave treatments for mechanical tests and water permeation measurements. The plasma treatment improved the matrix and fiber adhesion, while autoclave treatment decreased water solubility of the fibers. Singh et al [36] investigated the effect of treatments of sisal fibers with silane, titanate, and zirconate coupling agents and N-substituted methacrylamide on the mechanical properties of sisal fiber reinforced composites. The modification of sisal fibers provided better mechanical properties.

Table 2.6. Mechanical and physical properties of some selected natural fibers and E-glass [34]

Fibers	**Density (g/cm^3)**	**Diameter (mm)**	**Tensile Strength (MPa)**	**Young Modulus (GPa)**	**Elongation at break (%)**
Flax	1.5	40-600	345-1500	23-79	2.7-3.2
Hemp	1.47	25-250	550-900	38-70	1.6-4
Jute	1.3-1.49	25-250	393-800	13-26.5	1.16-1.5
Kenaf	1.5-1.6	2.6-4	350-930	40-53	1.6
Ramie	1.5-1.6	0.049	400-938	61.4-128	1.2-3.8
Sisal	1.45	50-200	468-700	9.4-22	3-7
Curaua	1.4	7-10	500-1100	11.8-30	3.7-4.3
Abaca	1.5	10-30	430-813	31.1-33.6	2.9
E-glass	2.55	15-25	2000-3500	70-73	2.5-3.7

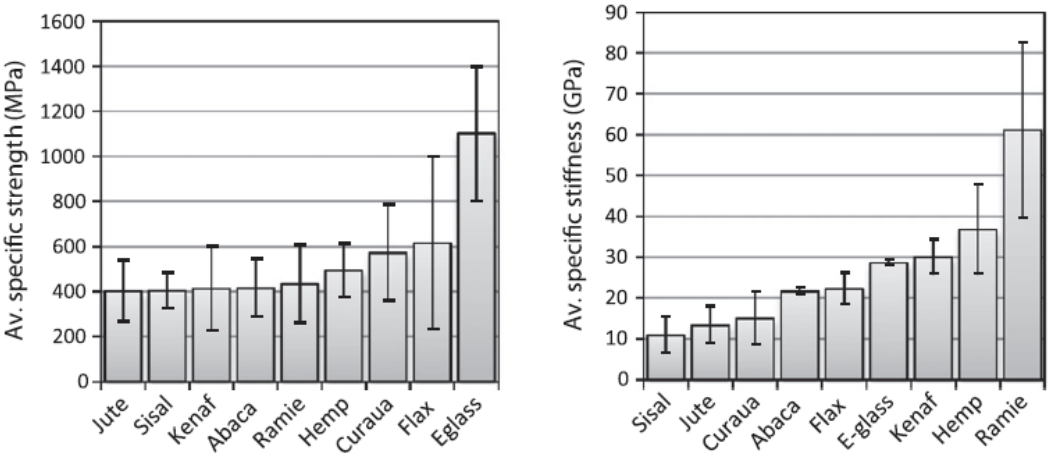

(a) (b)

Figure 2.6. Mechanical performances of some fibers [34].

Using of natural filler reinforced polymer composites for industrial applications is developing due to light weighting properties and abundance of natural fillers. Audi put an A2 car’s door trim panels were made of polyurethane reinforced with mixed flax and sisal [33]. Toyota used completely natural composite spare tire cover in RAUM 2003 model. The part was made of PLA matrix, which is from sugar cane and sweet potato, reinforced with kenaf fibers [33].

Minerals are also used as natural reinforcements for polymers. These natural reinforcements are produced from natural mineral sources by mining, followed by some processes like purification, calcination, drying and etc. Calcium carbonate, dolomite, clay, nano-clays, wollastonite, crystalline silicas, calcium sulfate, and huntite

/hydromagnesite etc. mixtures are the minerals used as reinforcements for polymers [29].

CHAPTER 3

DIATOMS AND THEIR APPLICATIONS

Diatoms are a group of unicellular chromophyte algae which colonize at the base of oceans. They are the most important group of eukaryotic phytoplankton and responsible for marine primary productivity at around 40%. In addition, diatoms have a significance role in the biochemical production of silica due to their cell wall biogenesis. There are more than 250 genera of diatoms and approximately 100000 species of diatoms in different shapes. Small-celled species of diatoms are 5-50 μm in size and large celled diatoms 2-5 mm in size. The biology of diatoms is not known very well. The siliceous cell walls of diatoms (Figure 3.1) are the biggest factor of their ecological success. They are also major players for production of atmospheric greenhouse gas photosynthetically [37]. Diatoms live in nature as benthic, attached to a sediment surface, and planktonic forms [38].

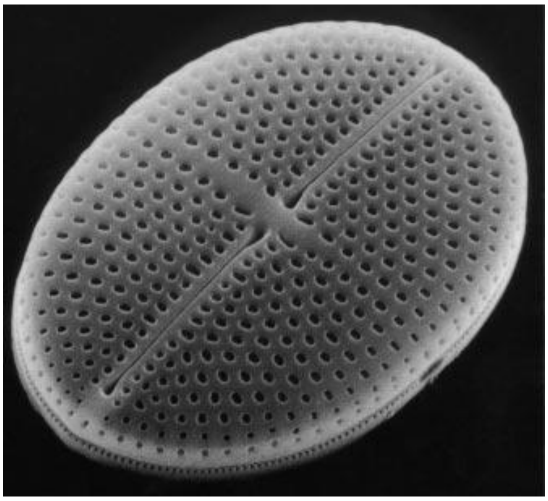

Figure 3.1. Scanning Electron Microscope Image of the diatom Mastogloia binotata (Grun) cl at 5800x magnification [37].

3.1. General Characteristics of Diatom Biology

Diatoms are consisted of an organic surface layer and a siliceous skeleton. The skeleton is known as frustule, which is an exclusive shaped external wall consisting of amorphous silica [$(SiO_2)n(H_2O)$]. The frustule is found in many different shapes as sheen in Figure 3.2 [37]. The frustule consists of two almost equal halves which are interlocking to each other like a Petri dish as depicted in Figure 3.3. The larger one of the halves is called epitheca and the smaller one is called hypotheca. Each theca is consisted of two parts: the valve which is the larger outer surface of the wall and a girdle which is a circular silica band attached to the valve [37].

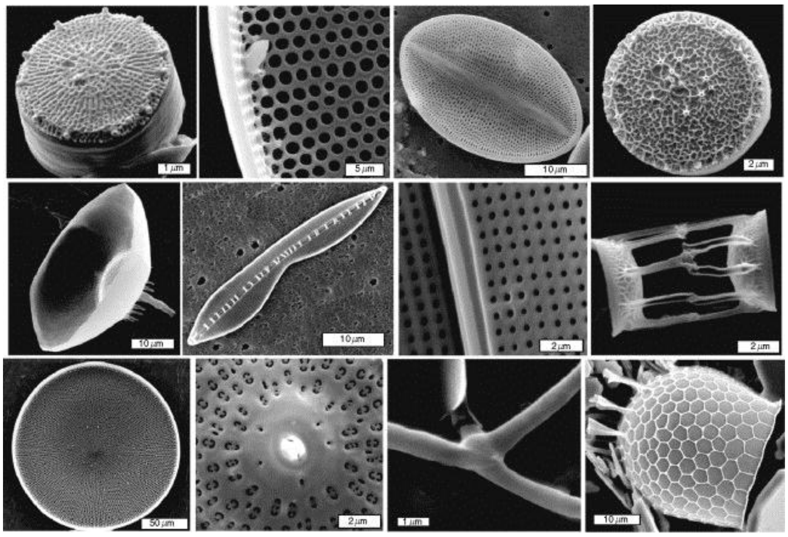

Figure 3.2. SEM images of different types of frustules [39].

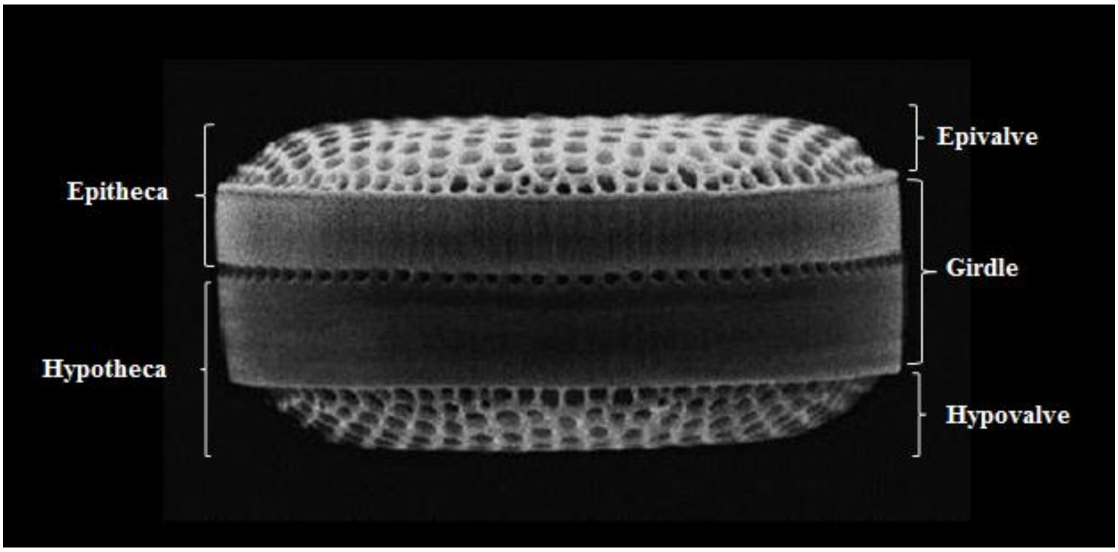

Figure 3.3. Frustule structure [40].

Diatoms are mainly categorized by the geometry of their frustules. There are two types of diatoms: centric diatoms (Figure 3.4(a)), which are radially symmetrical and circular shaped; pennate diatoms (Figure 3.4(b)) which are bilaterally symmetrical and elongated shaped [37]. Some diatoms exist in chains or aggregation of their species [41]. Frustules have regularly arranged pores, varying in the size of 10-200 nm, on their walls [42].

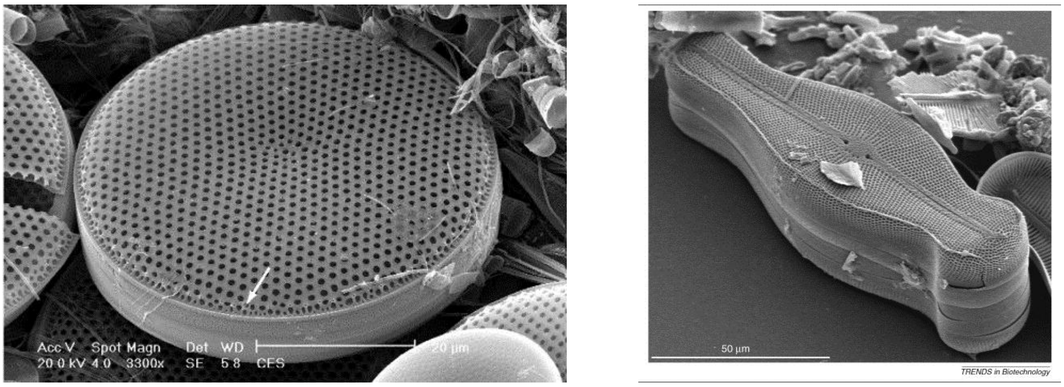

(a) (b)

Figure 3.4. (a) Centric diatom frustule (diatom, *Thalassiosira tumida*) [43] (b) Pennate diatom frustule(diatom, *Didymosphenia geminata* (Lyngbye)) [44].

Biosilica formation in the diatoms is a complex process and explained by the biomineralization. Biomineralization is the formation of inorganic minerals under the control of an organism in nature and primarily organized by aquatic livings such as diatoms, synurophytes, radiolaria and even multicellular sponges. Diatoms play a big role in this organization. Several plants like rice cereals, cucumber also deposit silica in order to strengthen their tissues. Some animals like mammals require silica for their growth of bone and cartilage. The formation of biosilica structures in diatoms occurs in a specific intracellular section which is called silica deposition vesicles (SDVs). Immediate precursor for biosilica formation inside SDV in not known precisely. However, $Si(OH)_4$ can be considered as the original source of the silica in biosilica formation. Furthermore, silica formation is catalyzed by silaffins and long-chain polyamins in diatoms. Two different types of SDVs are present at different stages of the cell cycle shown in Figure 3.5. When cell divison starts, a valve SDV is produced by each fraternal cell and more silica deposition occur. After the cell division ending, new biosilica structure occurs on the surface of the cell. Cell growth is provided by the increasing the distance between epitheca and hypotheca due to the stiffness of the biosilica wall. Thus, girdle bands are formed in each SDVs with cell growth process and released to the surface of the cell in order to avoid the formation of gaps. New cell division starts when the cell volume reaches to enough size [45].

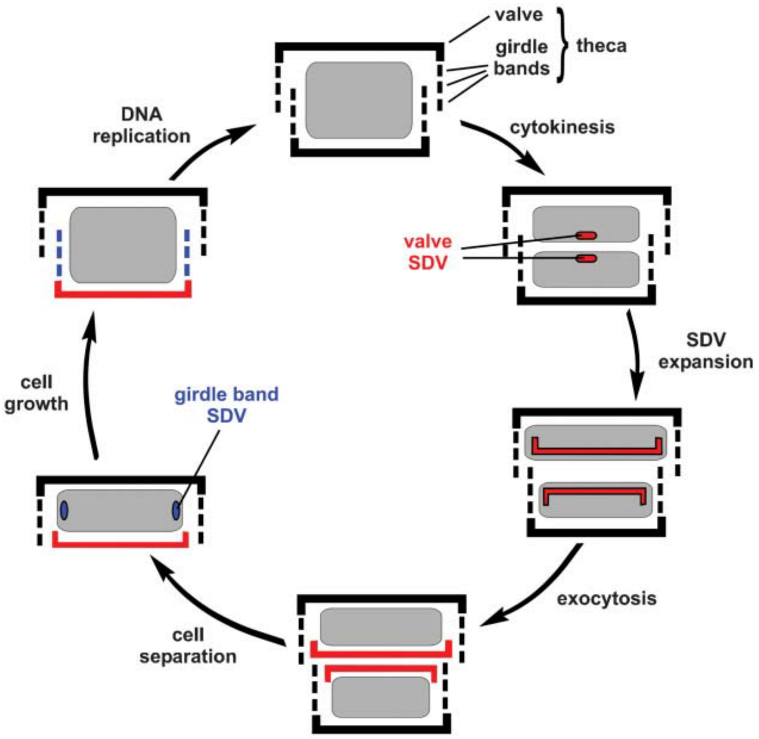

Figure 3.5. Diatom Cell Division [45].

3.2. Diatomaceous Earth

Diatomaceous earth, also known as diatomite or kieselguhr, is a sedimentary siliceous rock that is formed by the accumulation of dead diatom frustules in oceans or fresh waters. The particle size of diatomaceous earth varies between 1 μm and 1 mm. The chemical composition of diatomaceous earth consists of 80%-90% silica, 2%-4% alumina, and 0.5%-2% hematite. Diatomaceous earth has very low density with 80%-90% porosity. Dried diatomite powder (Figure 3.6) can absorb 1.5 to 3 times its weight to water. The melting point of diatomite ranges from 1000^{o}C to 1750^{o}C. Chemical inertness of diatomite is obtained by its siliceous structure and only strong acids like hydrogen fluoride (HF) can solve diatomite. Diatomite was used first by Greeks as an abrasive material for creating building blocks. Diatomite blocks were used for making the 30-meter-diameter dome of Hagia Sophia in İstanbul in 535 AD. Diatomite was used as absorbent material for making dynamite by Alfred Nobel in 1884 [46]. Today, diatomaceous earth is used for 67% of filtration applications, 15% of cement additive and 7% of filler material. In addition to this, abrasives, insecticides, soil conditioner applications are other diatomaceous earth usage areas. Diatomite is produced from open pit mining areas (Figure 3.7). Major diatomite mining areas are in California, Oregon and Washington in the USA [47]. Diatomaceous earth production parameters are affected by the size, shape and type of frustules, silica content and impurities. Calcination is subjected to diatomite to remove organics, increase particle size, and reduce surface area and crystallize silica content. Simple calcination is carried out at 1000^{o}C and flux-calcination is carried out at 1200^{o}C with the addition of sodium components [46].

Figure 3.6. A commercial diatomaceous earth powder [48].

Figure 3.7. An open pit diatomaceous earth mining area in Washington [49].

3.3. Novel Applications of Diatom

Diatoms are interesting research area for scientists because of their intricate amorphous silica structure and the way of silica formation in their cells. Nanotechnologists are trying to create devices similar to diatoms. Photonic crystal properties of girdle bands are giving very important information to make biophotonic crystals. Another optical property of diatoms is the photoluminescence property. This gives an idea to create photoluminescence gas-sensing devices [44]. The light could be coupled into waveguide and photonic resonances were observed in the visible spectral range in diatom cell [42]. The properties like frustule porosity, very high surface area (100 m^2/g), biocompatibility and biodegradability of frustules make diatoms appropriate for drug-delivery applications. Drug release may be from the pores of the diatom or inside the frustule as shown in Figure 3.8 [44]. Diatoms are also used for nutritional applications. High quality vitamins, unsaturated fatty acids, amino acids and food supplements can be synthesized by diatoms [50].

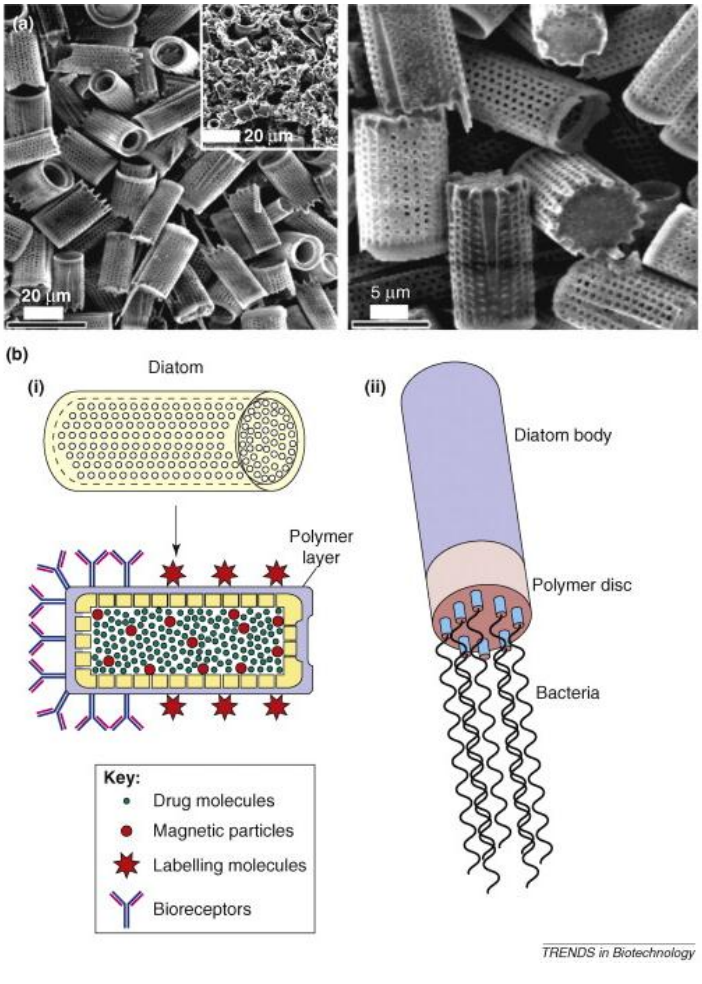

Figure 3.8. Preparation steps of silica capsules from diatomaceous earth for drug delivery [44].

Frustules of diatoms influence micro and nano production as a biomimetic model [51]. The three-dimensional structure of diatoms is advantage for the production of microelectronic devices with lithographic method. The structure of the frustule can be changed by the manipulation of the valves like varying the silicification degree [38].

Studies have also shown that 3D nanostructured networks can be created by copying the diatom nanostructure. The amorphous silica content of frustule is replaced by other chemicals (Figure 3.9). Anderson et al. [52] created a micro-porous material by diatom zeolitization with hydrothermal growth method. Losic et al. [53] applied a method for modification of diatoms by TiO_2 deposition using atomic layer deposition technique (AFD) in different cycles (Figure 3.10). The pore size of frustules was shown to be altered using the same technique (Figure 3.11). The proteins combine with biosilica in diatom frustule allow the dissolution and recovery of biosilica. The silica particles precipitated after dissolving silica in diatom *C.fusiformis* using natSil protein in vitro are shown in Figure 3.12 [54].

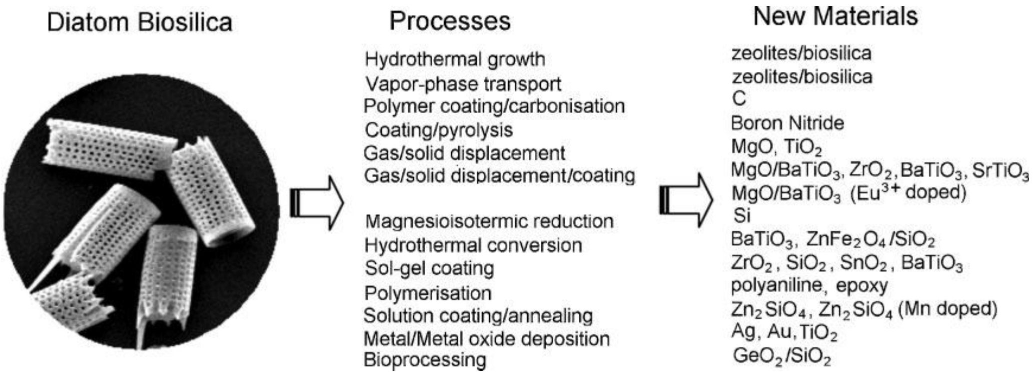

Figure 3.9. Production methods of 3D nanostructured materials created by diatom biosilica [55].

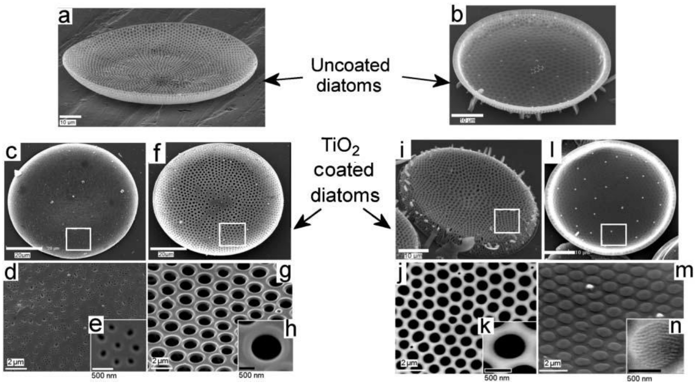

Figure 3.10. SEM images of uncoated frustules (a) *Coscinodiscus sp (b) Thalassiosira eccentric,* Frustules of *Coscinodiscus sp* after TiO_2 coating by ALD (c-e) external porous layer and (f-h) internal porous layer,Frustules of Thalassiosira eccentric (i-k) external porous layer (l-n) internal porous layer [52].

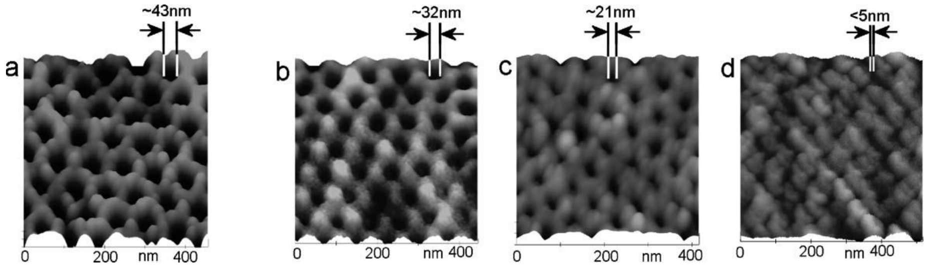

Figure 3.11. Pore reduction of *Thalassiosira eccentric* (a) AFM images of uncoated samples (b-d) TiO_2 coated samples with 250,500 and 1000 AFD cycles [52].

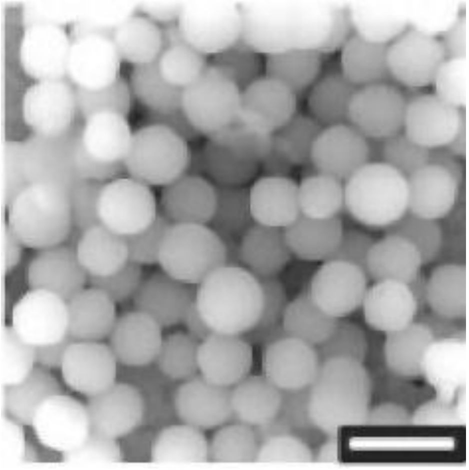

Figure 3.12. Silica particles obtained by diatom *C.fusiformis* [54].

Frustules can also be used as filler in polymer matrices. Gültürk et al. [56] investigated the effect of diatomaceous earth filler addition on the quasi static and high-strain rate compressive behavior of an epoxy matrix. The frustule filling of epoxy with 15wt%, increased both yield strength and elastic modulus of the epoxy both at quasi-static and high strain rates (Figure 3.13).

As a summary, biomineralizitaon in diatoms, intricate 3D morphology of diatoms, their optical properties, and biomimetic approaches make diatoms very interesting fields of work for scientists.

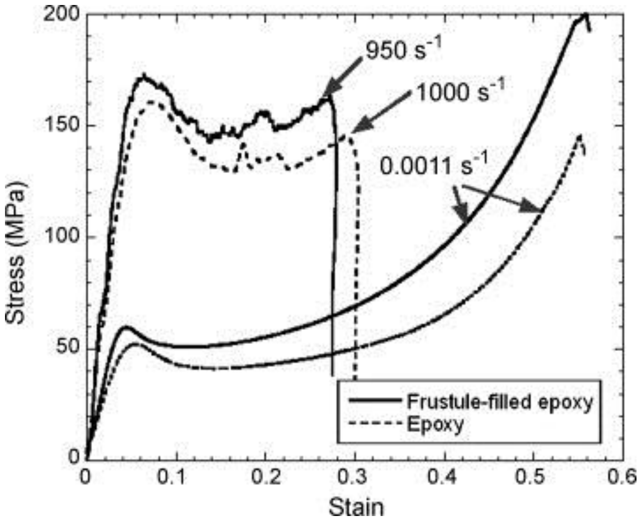

Figure 3.13. Comparison of compressive mechanical properties of neat epoxy and frustule-filled epoxy [56].

CHAPTER 4

MATERIALS AND EXPERIMENTAL ANALYSIS

4.1. Diatom Frustules

Two groups of diatom frustules were investigated for filling polymer matrix. The first group was isolated and cultured in Ege University Hydrobiology Laboratories. These were single species and their geometries had unique shapes. Cultered diatoms were received in the form of biomass shown in Figure 4.1(a). The second grup of diatoms was a commercial diatomaceous earth, known as diatomite and received from Alfa Aesar, Johnson Matthey Co. England (Figure 4.1(b)).

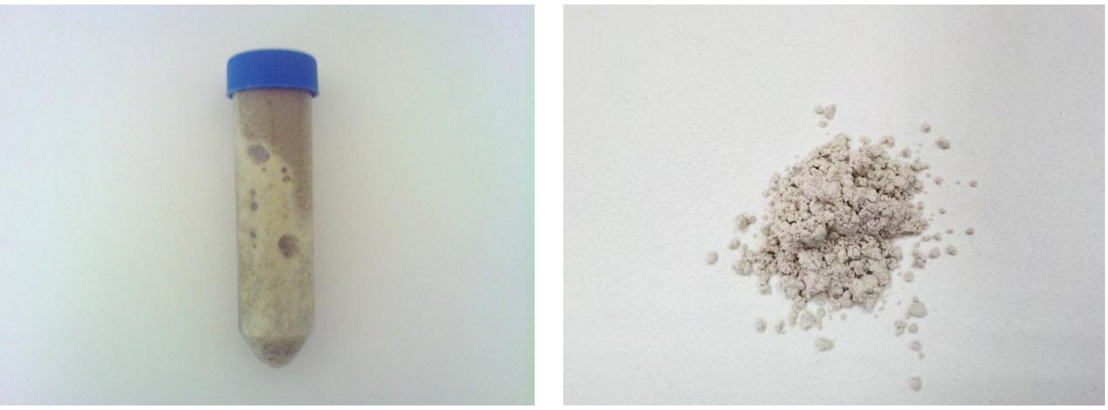

(a) (b)

Figure 4.1. (a)As received diatom biomass and (b)commercial diatomaceous earth.

4.1.1. Isolated and Cultured Diatoms

Various species of diatoms were collected from determined stations in İzmir (Aegen Sea, some fresh waters and some moist areas). Collected species were then filtrated, compacted and kept in their appropriate nutrition environment. Diatom Medium (DM) (Table 4.1) and Allen Medium (Table 4.2) were used to keep fresh water diatoms and LDM-Medium (Table 4.3), and f/2 concentrator medium (Table 4.4) were used to keep sea diatoms. The solutions increased the diatom development in the environment.

Table 4.1. The composition of DM environment

Number	Chemical's Name	Stock	Amount
1	$Ca(NO_3)_2.4H_2O$	4.00 g /200ml dH_2O	1 mL/L
2	KH_2PO_4	2.48 g /200ml dH_2O	1 mL/L
3	$MgSO_4.7H_2O$	5.00 g /200ml dH_2O	1 mL/L
4	$NaHCO_3$	3.18 g /200ml dH_2O	1 mL/L
5	EDTAFeNa $EDTANa_2$	0.450 g/200ml dH_2O 0.450 g/200ml dH_2O	1 mL/L
6	H_3BO_3 $MnCl_2.4H_2O$ $(NH_4)_6Mo_7O_24H_2O$	0,496 g200ml dH_2O 0.278 g /200ml dH_2O 0.200 g200ml dH_2O	1 mL/L
7	Cyanocobalamin Thiamine HCl Biotin	0.008 g200ml dH_2O 0.008 g/200ml dH_2O 0.008 g200ml dH_2O	1 mL/L
8	$Na_2SiO_3 \cdot 9H_2O$	11.40 g /200ml dH_2O	1 mL/L

Table 4.2. The composition of Allen Medium

Number	Chemical's Name	Stock	Amount
1	HEPES buffer (Sigma H-3375)	----	2.3 g/L
2	$NaNO_3$ (Fisher BP360-500)	----	1.5 g/L
3	P-IV metal solution	----	1 mL/L
4	K_2HPO_4 (Sigma P 3786)	1.5 g/200 mL dH_2O	5 mL/L
5	$MgSO_4 \cdot 7H_2O$ (Sigma 230391)	1.5 g/200 mL dH_2O	5 mL/L
6	Na_2CO_3 (Baker 3604)	0.8 g/200 mL dH_2O	5 mL/L
7	$CaCl_2 \cdot 2H_2O$ (Sigma C-3881)	0.5 g/200 mL dH_2O	10 mL/L
8	$Na_2SiO_3 \cdot 9H_2O$ (Sigma 307815)	1.16 g/200 mL dH_2O	10 mL/L
9	Citric Acid·H_2O (Fisher A 104)	1.2 g/200 mL dH_2O	1 mL/L

Table 4.3. The composition of LDM Medium

Number	Chemical's Name	Stock	Amount
1	Sterilized Sea Water		950mL/L
2	$NaNO_3$	10 g/400mL dH_2O	1 mL/L
3	$CaCl_2 \cdot 2H_2O$	1 g/400mL dH_2O	1 mL/L
4	$MgSO_4 \cdot 7H_2O$	3 g/400mL dH_2O	1 mL/L
5	K_2HPO_4	3 g/400mL dH_2O	1 mL/L
6	KH_2PO_4	7 g/400mL dH_2O	1 mL/L
7	NaCl	1 g/400mL dH_2O	1 mL/L
8	P-IV metal solution		6 mL/L
9	Tryptone		1 g/L
10	Vitamin B_{12}		1 mL/L
11	Biotin Vitamin Solution		1 mL/L

Table 4.4. The composition of f/2 Medium

Number	**Chemical's Name**	**Stock**	**Amount**
1	$NaNO_3$	7.5 g/100 mL dH20	1 mL/L
2	$NaH_2PO_4 \cdot H_2O$	0.5 g/100 mL dH20	1 mL/L
3	$Na_2SiO_3 \cdot 9H_2O$	3 g/100 mL dH20	1 mL/L
4	Trace Metals Solution	----	1 mL/L
5	Vitamin B_{12}	----	1 mL/L
6	Biotin Vitamin Solution	----	1 mL/L
7	Thiamine Vitamin Solution	----	1 mL/L

The purpose of the species isolation wasto separate exclusive species from mixed species. In order to do this, various mechanical processes like centrifuging, sonic bathing, rarefactioning and agar disk diffusion techniques were applied. The separate exclusive species were augmented by culturing with sedimentation and centrifuge. Obtained biomass were kept at -20^{o}C. The picture of a cultured diatom biomass is shown in Figure 4.2.

Figure 4.2. Cultured diatom biomass.

As-received pennate diatom biomasses from Ege University are categorized in the systematic of species and listed below with pictures.

4.1.1.1. *Pseudo-nitzschia delicatissima*

Phylum: BACILLARIOPHYTA Engler and Gilg, 1924

Classis: BACILLARIOPHYCEAE Haeckel, 1878
Ordo: Bacillariales Hendey
Familia: BacillariaceaeEhrenberg, 1831
Genus: Pseudo-nitzschia H. Peragallo, 1900
Species: *Pseudo-nitzschia delicatissima (P.T. Cleve) Heiden, 1928*
Syn: *Nitzschia delicatissima P.T. Cleve 1897*
Nitzschia actydrophila Hasle 1965

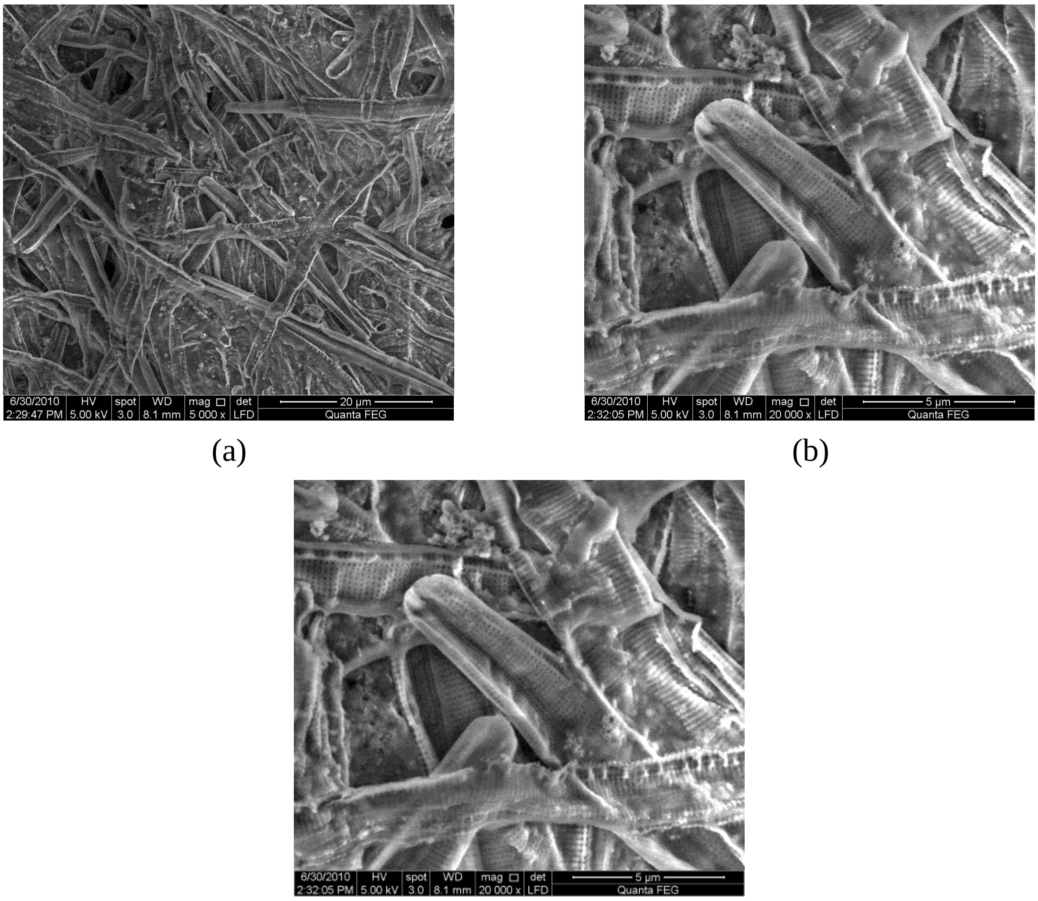

(a) (b)

(c)

Figure 4.3. SEM images of *Pseudo-nitzschia delicatissima* diatom species (a)5000x, (b) 20000x and (c) 50000x.

4.1.1.2. *Achnanthes taeniata*

Phylum: BACILLARIOPHYTA Engler and Gilg, 1924
Classis: BACILLARIOPHYCEAE Haeckel, 1878
Ordo: Achnanthales P.C. Silva
Familia: Achnanthaceae Kützing, 1844
Genus: Achnanthes Bory de Saint-Vincent, 1822
Species: *Achnanthes taeniata* Grunow, 1880
Syn: *Achnanthes taeniata var. hyperborea* Grunow
Achnanthes hyperborea Grunow 1884

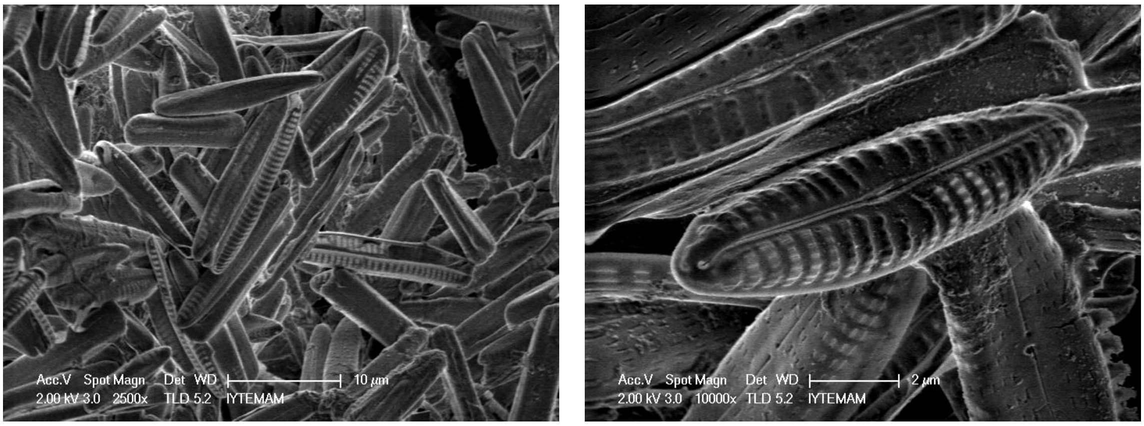

(a) (b)

Figure 4.4. SEM images of *Achnanthes taeniata* diatom species (a)2500x, and (b) 10000x.

4.1.1.3. *Amphora coffeaeformis*

Phylum: BACILLARIOPHYTA Engler and Gilg, 1924

Classis: BACILLARIOPHYCEAE Haeckel, 1878
Ordo: Bacillariales
Familia: Catenulaceae
Genus: Amphora
Species: *Amphora coffeaeformis* (Agardh)

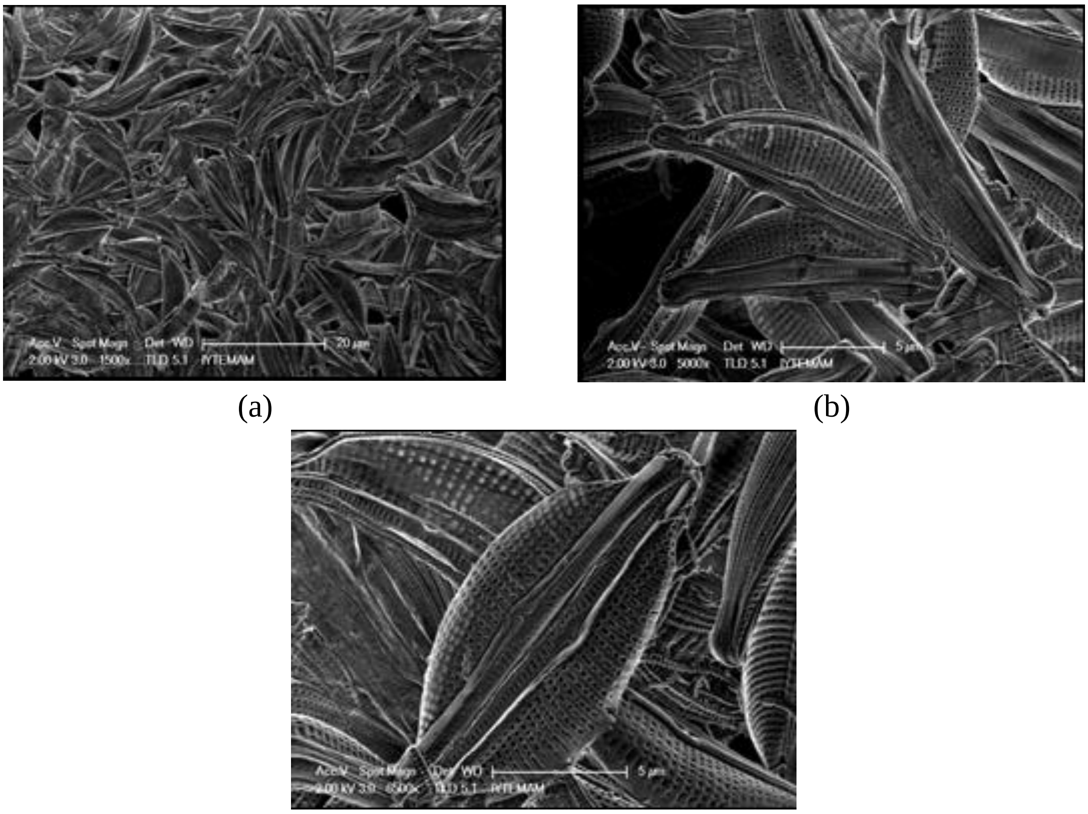

(a) (b)

(c)

Figure 4.5. SEM images of *Amphora coffeaeformis* diatom species (a)1500x, and (b) 5000x (c) 6500x.

4.1.1.4. *Cylindrotheca closterium*

Phylum: BACILLARIOPHYTA Engler and Gilg, 1924
Classis: BACILLARIOPHYCEAE Haeckel, 1878
Ordo: Fragilariales P.C. Silva
Familia: Fragilariaceae Greville, 1833
Genus: Ceratoneis Ehrenberg
Species: *Ceratoneis closterium* Ehrenberg 1841
Syn: *Cylindrotheca closterium* (Ehrenberg) Reimann and J.C. Lewin 1964

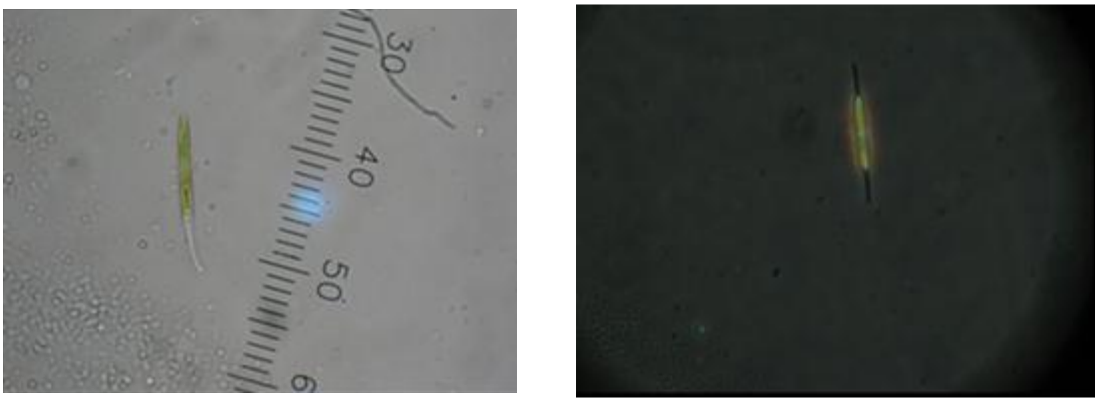

(a) (b)

Figure 4.6. Optical microscope images of *Cylindrotheca closterium.*

4.1.2. Diatomaceous Earth

As-received diatomaceous earth (Alfa Aesar brand) consisted of the mixed diatom species of pennate and centric diatom frustules as seen in Figure 4.7(a). The pennate diatom frustules are circular in shape (Figure 4.7.(b)) and centric diatom frustules are elongated in one axis (Figure 4.7(c)). The pore size on the frustule wall varied between 200 and 1000 nm. The frustules were observed to be broken as a result of the milling process applied by the producer.

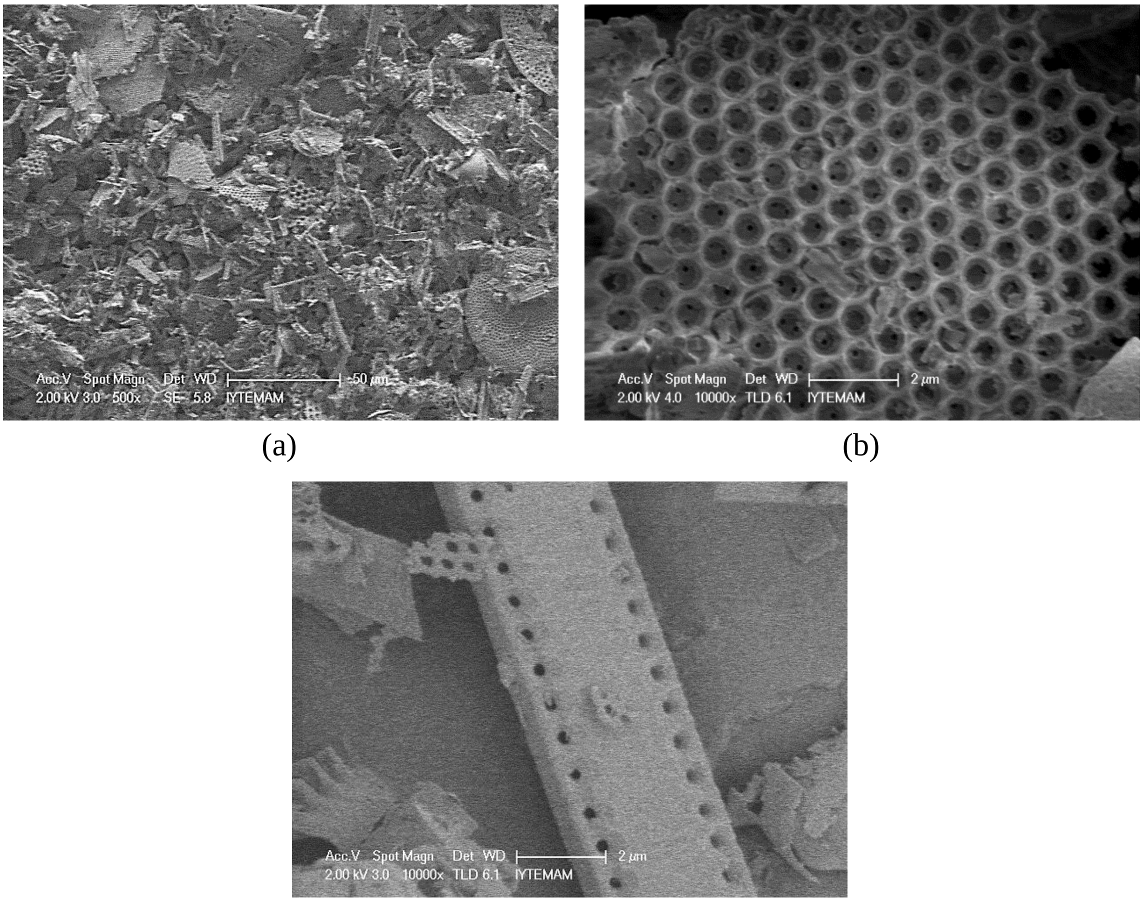

(a) (b)

(c)

Figure 4.7. SEM pictures of diatomaceous earth (a) general view (b) centric diatom and (c) pennate diatom.

4.2. Preparation and Cleaning of Diatom Biomass to Obtain Diatom Frustules

As stated in Chapter 2, diatoms encompasses both extracellular and intracellular organic parts. The organic part is found on the surface of the frustule. This organic layer must be cleaned before the use of the diatom frustules as reinforcement/filler in polymer matrices. In addition, the salts such as NaCl, KCl and $CaCl_2$ derived from diatoms cultural environment should also be also removed as they adversely affect the mechanical properties of the epoxy matrix. Heat treatment and nitric acid digestion routes have been investigated to remove the organic surface layer and salts from the cultured diatom frustules.

4.2.1. Heat Treatment Route

The heat treatment of diatom frustules was performed in a Protherm box furnace (Figure 4.8). The dried frustules were inserted into furnace inside a ceramic crucible. The heating and cooling rate of the furnace was 10^{o}C/min. Before deciding the heat treatment temperature, *Pseudo-nitzschia delicatissima* diatom frustules were heat treated for one hour at 100^{o}C intervals. The resultant XRD spectra of natural and heat treated *Pseudo-nitzschia delicatissima* diatom species are shown in Figure 4.9 as function of heat treatment temperature. As is seen in Figure 4.9 amorphous to crystalline transition of silica frustules starts at about 900^{o}C and is completed at around 1200 ^{o}C. A treatment temperature of 700^{o}C which was lower than the transformation temperature and a duration time of 2 h were selected in the heat treatment process to avoid crystalline phase transformation.

Figure 4.8. Box furnace used in heat tretament.

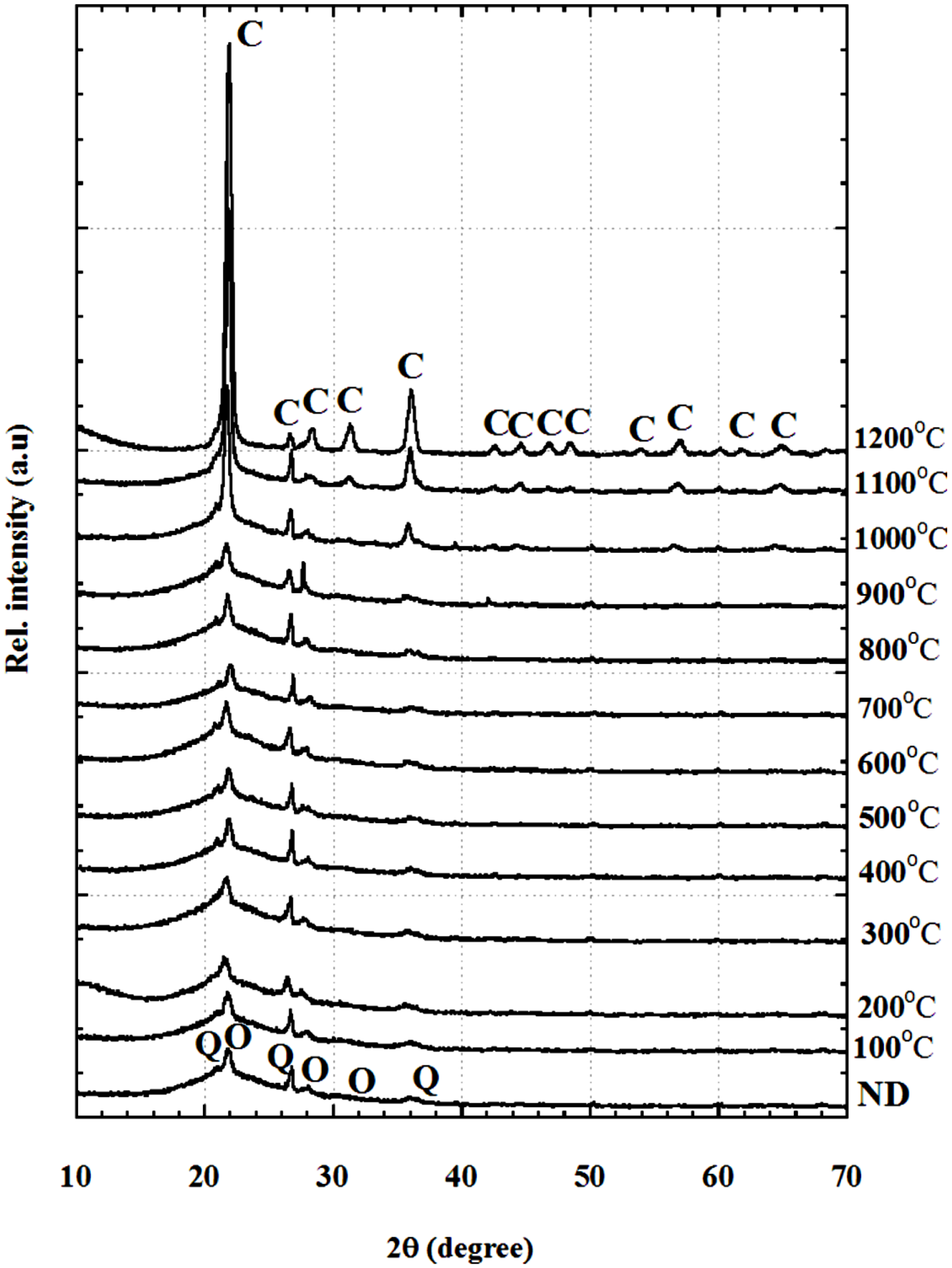

Figure 4.9. XRD spectra of amorphous diatoms and heat-treated diatoms.

4.2.2. Nitric Acid Digestion of Diatom Biomass

The steps of the used nitric acid digestion are summarized in Figure 4.10. In the first step, the living diatom biomass was added into 65% nitric acid (Pancreac) with a 1:1

ratio and the solution was mixed using a Vortex-Velp RX3 mixer at 2400 rpm (Figure 4.11(a)). Following the mixing stage, the mixture was poured into a beaker and stirred and heated simultaneously on a hot plate (Figure 4.11(b)) at 400 rpm above the vapor temperature of the nitric acid (150^{o}C) for 1.5 h. Following the heating stage, the remaining mixture at the bottom of the beaker was allowed to cool down to room temperature. The mixture was then placed into centrifuge tubes and topped up with distilled water. The centrifuge was performed at 4000 rpm for 5 min in Beckman Coulter Allegra 25R centrifuge machine (Figure 4.11(c)). This process was repeated for 3 or 4 times until the diatom frustules were completely cleaned. Finally, the supernatant was pipetted off (Figure 4.11(d)) and the diatom pellets were placed into Labconco brand freeze dryer in order to remove water (Figure 4.11(e)). The picture of cleaned diatom powder is shown in Figure 4.11(f).

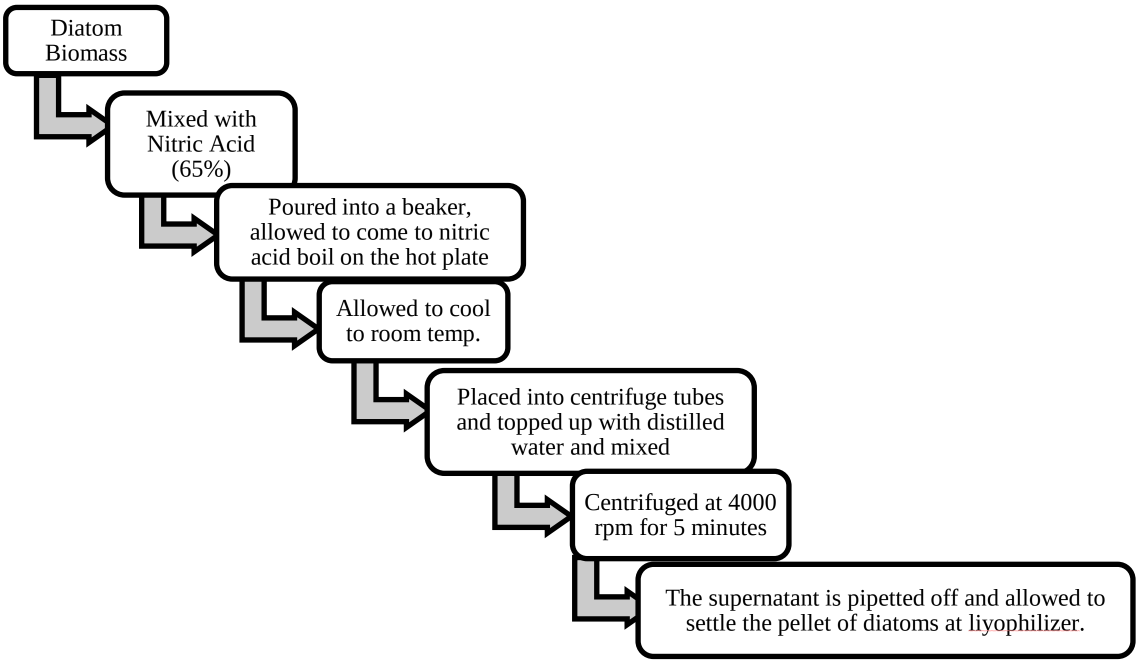

Figure 4.10. Nitric acid digestion steps.

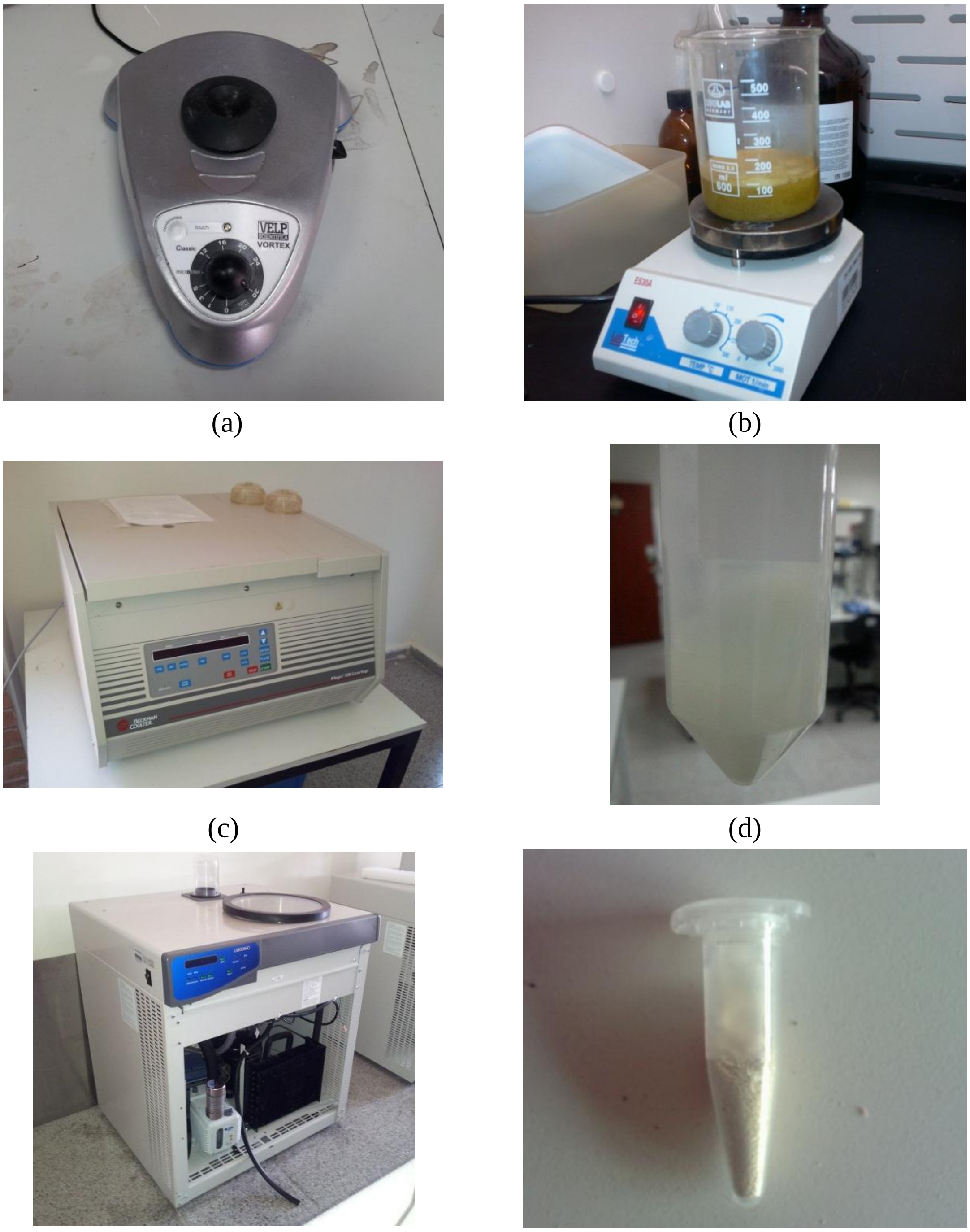

(a) (b)

(c) (d)

(e) (f)

Figure 4.11. Nitric acid digestion equipment and resultant diatom frustule powder; (a) mixer, (b) hot plate, (c) centrifuge, (d) diatom in solution, (e) freeze drier and (f) diatom powder.

4.3. Heat Treatment of Diatom Frustules

Alfa Aesar brand commercial diatomaceous earth was heat-treated at varying temperatures in a box furnace. The heating and cooling rate of the furnace was

10^oC/min. The diatomaceous earth was heat treated for two hours at 100^oC intervals. Change of crystallography of diatom filling will give different mechanical properties.

4.4. Characterization of Diatom Frustules

The crystallographic structure of diatom frustules was determined using Philips X'Pert Pro X Ray Diffraction (XRD) device (Cu-Kα radiation, λ=1.54 A° and 40 kV, 5-80^o general scanning). The elemental composition of diatom frustules was determined using Spectro IQ II X Ray Fluorescence (XRF) device. The chemical bonding of frustules was determined with Perkin Elmer FT-IR System Spectrum BX Fourier Transform Infrared Spectroscopy (FT-IR) device. FT-IR analysis was performed in a range of 400-4000 cm^{-1} wavenumbers. The morphological properties and surface topography of frustules and frustule filled composite samples were investigated using (FEI Quanta 205 FEG and Philips XL-30S FEG Scanning Electron Microscopies in secondary electron (SE) and back scattered electron (BSE) modes.

4.5. Preparation of Diatom Frustule Filled Polymer Matrices

An epoxy resin (Grandmer VN-111) was chosen as the matrix for diatom frustule filling due to its high strength and dimensional stabilization after thermal curing. Nitric acid treated or heat-treated commercial diatom frustules were mixed with epoxy resin using an Ultra-Turrax T 25 IKA digitally controllable mechanical disperser (Figure 4.12(a)) at 20000 rpm. Mixing process was continued until a homogeneous mixture was obtained (approximately 3-4 minutes). The mixture was then subjected to vacuum (-1 Pa) in order to remove the trapped gas bubbles. The air bubbles risen to the surface of the mixture was burst after a while as a result of the vacuum environment (Figure 4.12 (b)). Then the hardener with an amount 25% of epoxy resin was added to the mixture. Then, the mixture was stirred gently not to create new air bubbles and poured into a silicon mold (4x4x1 cm) (Figure 4.12(c)). The mixture was allowed to wait in the mold at room temperature for 24 h. After the polymerization reaction, the sample was removed from the mold and placed into an oven for thermal curing at 110°C for 5 h.

The compression test samples were core drilled from the molded composite plates. During core drilling water was used as coolant. The test samples were 9.80 mm in diameter and 12 mm in length with an aspect ratio of 1.22. For comparison unfilled epoxy samples were also prepared using the same procedure outlined above. Figure 4.13 shows the pictures of the unfilled and filled core drilled epoxy test samples.

(a) (b) (c)

Figure 4.12. (a) Ultra-Turrax mechanical disperser, (b) vacuum set-up and (c) silica mold.

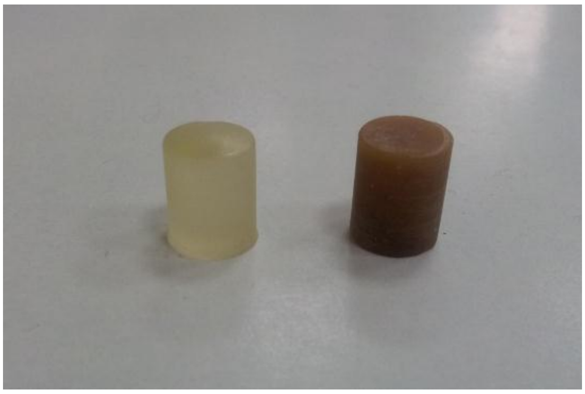

Figure 4.13. Unfilled epoxy compression test sample (left) and diatom frustule filled epoxy compression test sample (right).

The compression tests were performed using Shimadzu universal testing machine (Figure 4.14) at a crosshead speed of 5 mm/min corresponding to a strain rate 1×10^{-3} s^{-1}. Before each test the compression platens were lubricated using grease. The composite samples for microscopy were prepared by mounting the samples in Buehler epo-wick branded fast curing epoxy. Samples were grinded with Buehler Met-II SiC grinding papers through 800, 1000, 1200, 2000 and 2400 grids. Then, the samples were polished sequentially 9 µm, 6 µm, 3 µm and 1 µm diamond solution.

Figure 4.14. Quasi-static testing device.

CHAPTER 5

RESULTS AND DISCUSSIONS

5.1. Materials Characterization Results of Frustules

5.1.1. *Pseudo-nitzschia delicatissima* Diatom Frustules

The picture of *Pseudo-nitzschia delicatissima* diatom frustule powder after heat treatment is shown in Figure 5.1. The color of the powder changes from white to grey after the heat treatment. The ignition loss of heat-treated *Pseudo-nitzschia delicatissima* diatom species is measured as ~16% at 1000^{o}C. This is due to the burning of the organic matters of the diatom biomass [57]. The organic matter on the frustules consists of proteins, carbohydrates and fats [58]; therefore heating to 1000^{o}C burns the organic compounds. The XRF analyses results of *Pseudo-nitzschia delicatissima* diatom powder are tabulated in Table 5.1. Relatively high contents of Na, Cl and Ca in the heat-treated frustule powder are due to the presence of salts, which remain in the structure. The typical diatom frustule powder composition is tabulated in Table 5.2 and contains 80-90% of SiO_2. The XRF analysis results of the heat treated *Pseudo-nitzschia delicatissima* do not match with the typical composition of the diatom frustules, the SiO_2 content (about 20%) is relatively lower than the typical concentration. This is mainly because of the salts including NaCl, MgO and CaO remaining in the diatom powder after heat treatment. The boiling points of NaCl, MgO and CaO are sequentially 1413^{o}C [59], 3600^{o}C [60] and 2850^{o}C [61] and therefore heat treatment at 700^{o}C cannot remove these salts. XRD spectra of *Pseudo-nitzschia delicatissima* diatom species after heat treatment process at 700^{o}C is shown in Figure 5.2. The peaks in Figure 5.2 belong to the halide form crystalline NaCl, confirming the presence of salts in the powder.

Table 5.1. XRF analysis of the heat treated (700^{o}C, 2 h) *Pseudo-nitzschia delicatissima* frustules

Component	**Na_2O**	**MgO**	**SiO_2**	**P_2O_5**	**SO_3**	**Cl**	**K_2O**	**CaO**
Concentration (%)	14.84	9.302	19.23	1.645	2.231	11.92	1.622	19.43

Table 5.2. The composition of the diatom frustule [46]

Component	**Al_2O_3**	**MgO**	**SiO_2**	**CaO**	**Fe_2O_3**
Concentration (%)	1.5-4	1-2	80-90	0.5-1	1-4

Figure 5.1. *Pseudo-nitzschia delicatissima* diatom frustules powder after heat treatment.

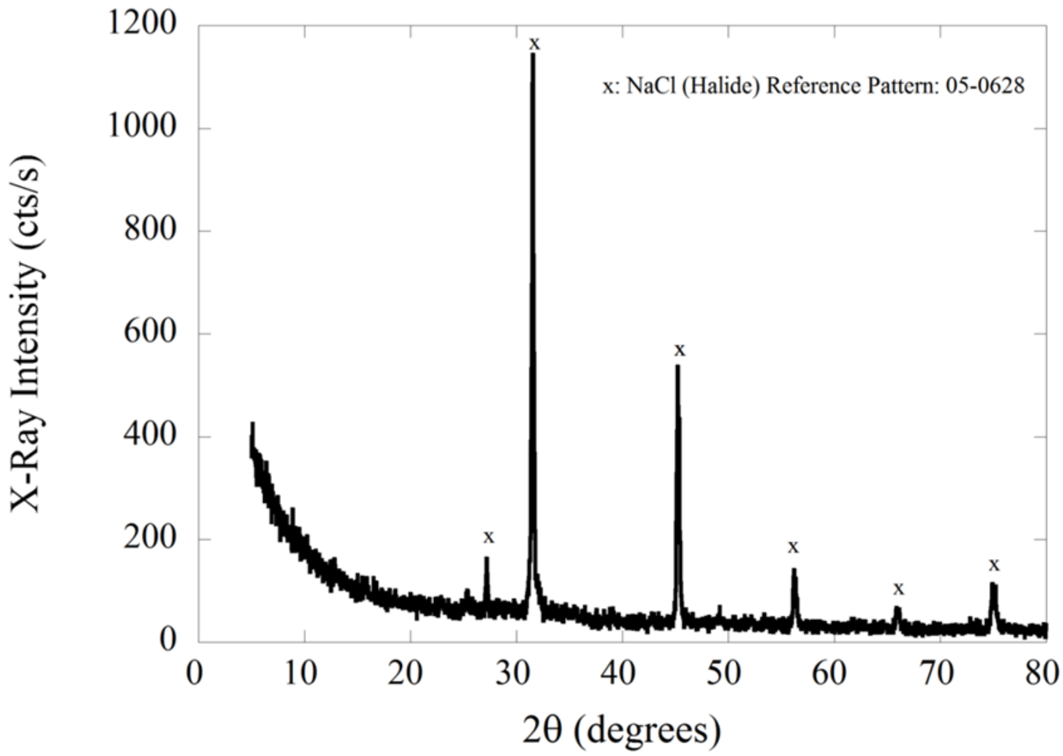

Figure 5.2. XRD pattern of *Pseudo-nitzschia delicatissima* diatom species after heat treatment at 700^{o}C for 2 h.

The SEM images of untreated *Pseudo-nitzschia delicatissima* frustules at 3 different magnifications are shown in Figures 5.3(a-c). As seen in the same micrographs, frustules are bilateral symmetrical and the length of the frustules ranges between 15 and 20 μm and the width between 2 and 2.5 μm. These are pennate type diatoms. The SEM images of *Pseudo-nitzschia delicatissima* diatom species after the heat treatment are shown in Figures 5.4(a) and (b). As seen in the same micrographs, the frustules are fractured significantly after the heat-treatment process. It is believed that the thermal residual stresses result in the fracture of the frustules. The fracture of the frustules might be due to the weak structures of these frustules. The mechanical properties of frustules highly depend on difference in pore size, pore distances, porosity of frustules and biomineralization process. The quality of nutrition (Si concentration) during culturing could affect the resultant mechanical properties of frustules. It is also noted heat treatment of the *Pseudo-nitzschia delicatissima* diatom frustules following by fast cooling may be used to obtain nano SiO_2. It is observed that the broken frustule parts are in the size range between 60 nm and 300 nm (Figure 5.4(b)).

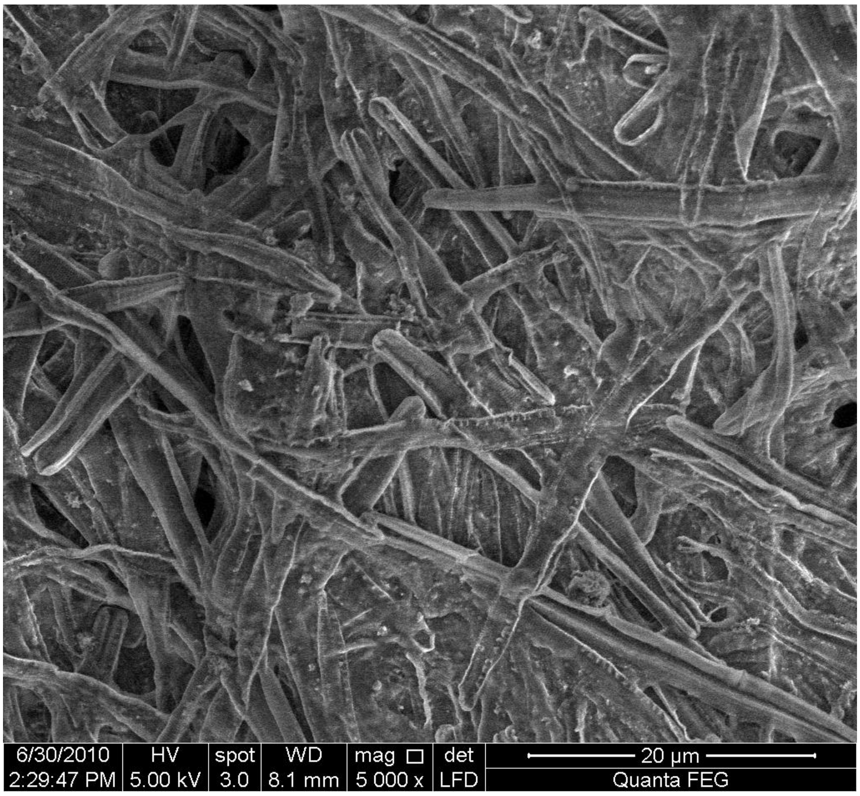

(a)

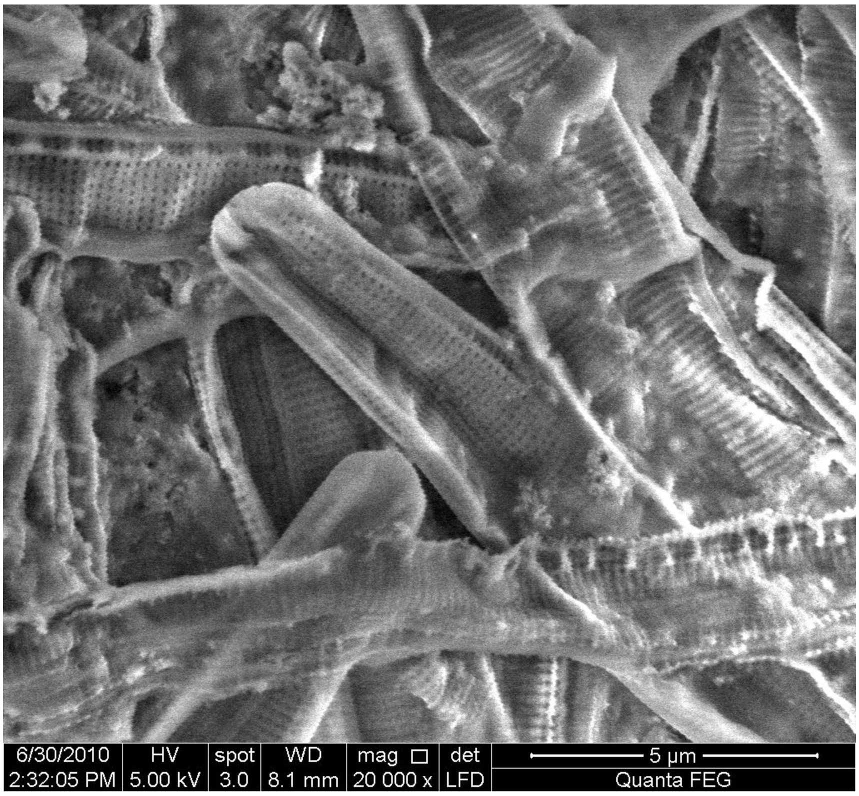

(b)

Figure 5.3. SEM images of *Pseudo-nitzschia delicatissima* diatom species before the heat treatment: (a) 5000x, (b) 20000x and (c) 50000x.

(cont. on next page)

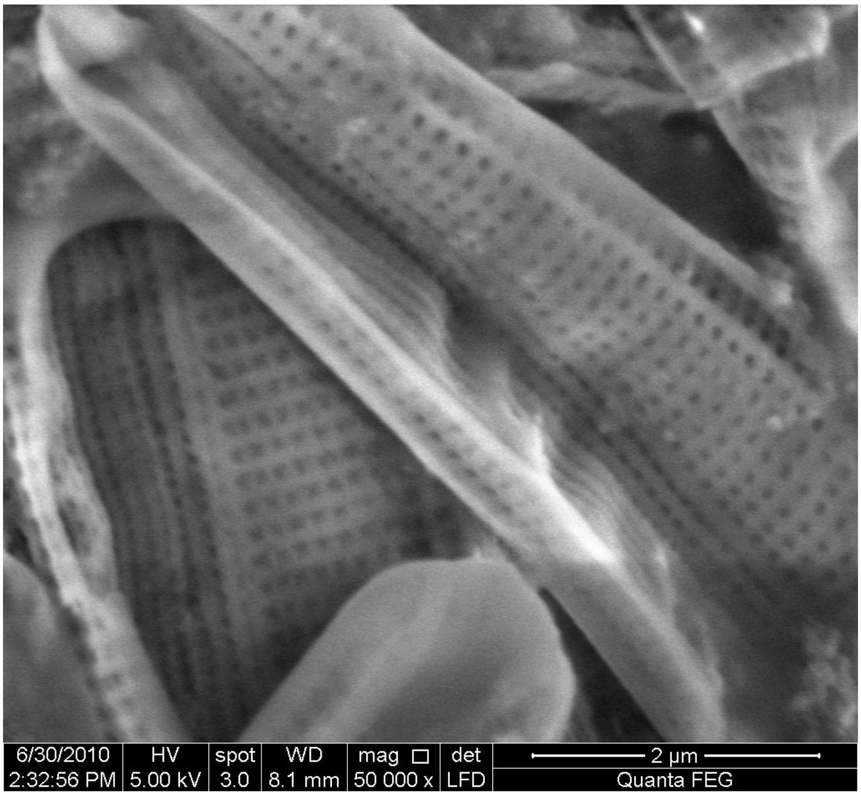

(c)

Figure 5.3.(cont.)

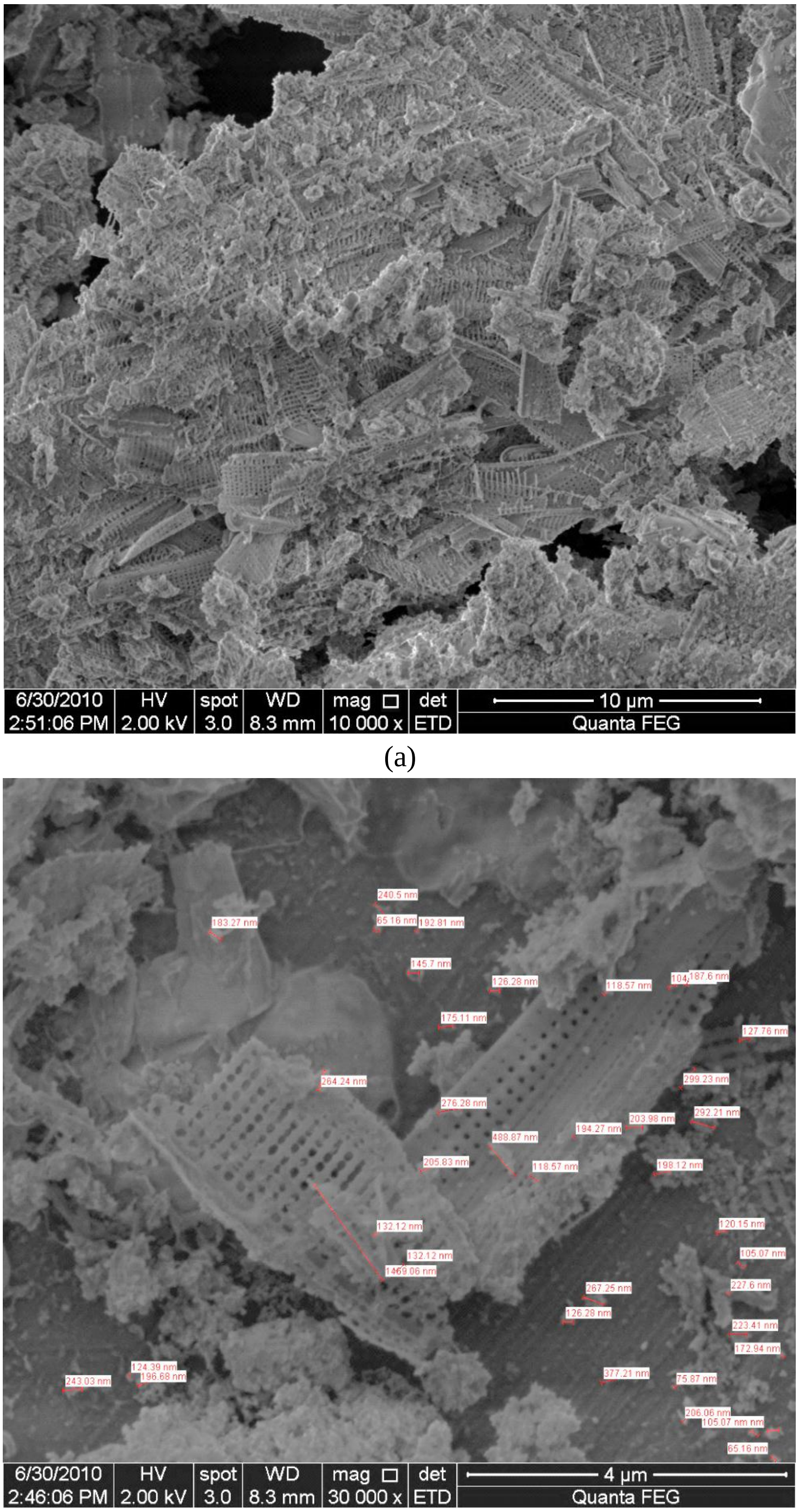

(a)

(b)

Figure 5.4. SEM images of *Pseudo-nitzschia delicatissima* diatom species after the heat treatment (a) 10000x and (b) 30000x.

The composition of *Pseudo-nitzschia delicatissima* diatom frustules after the nitric acid digestion is tabulated in Table 5.3. The silica content is about 83%. Very low concentrations of Cl, Ca and K are found, indicating that that nitric acid digestion dissolves the salts efficiently. The XRD spectra of *Pseudo-nitzschia delicatissima* diatom frustules after nitric acid digestion are shown in Figure 5.5. The silica is found both in amorphous opal-A and quartz structures. The SEM images of Pseudo-*nitzschia delicatissima* diatom frustules after nitric acid digestion are shown in Figures 5.6 (a) and (b). As seen in the same figures, the walls of diatom frustules remain unfractured after the nitric acid digestion. In addition, the organic layer on the surfaces of the frustules is completely removed following the nitric acid digestion as the surface topography of the frustules is seen in detail in the same micrographs.

Table 5.3. XRF analysis of *Pseudo-nitzschia delicatissima* diatom species after nitric acid digestion

Component	**Na_2O**	**MgO**	**SiO_2**	**P_2O_5**	**SO_3**	**Cl**	**K_2O**	**CaO**
Concentration (%)	1.4	1.2	83	<1	<1	<1	<1	<1

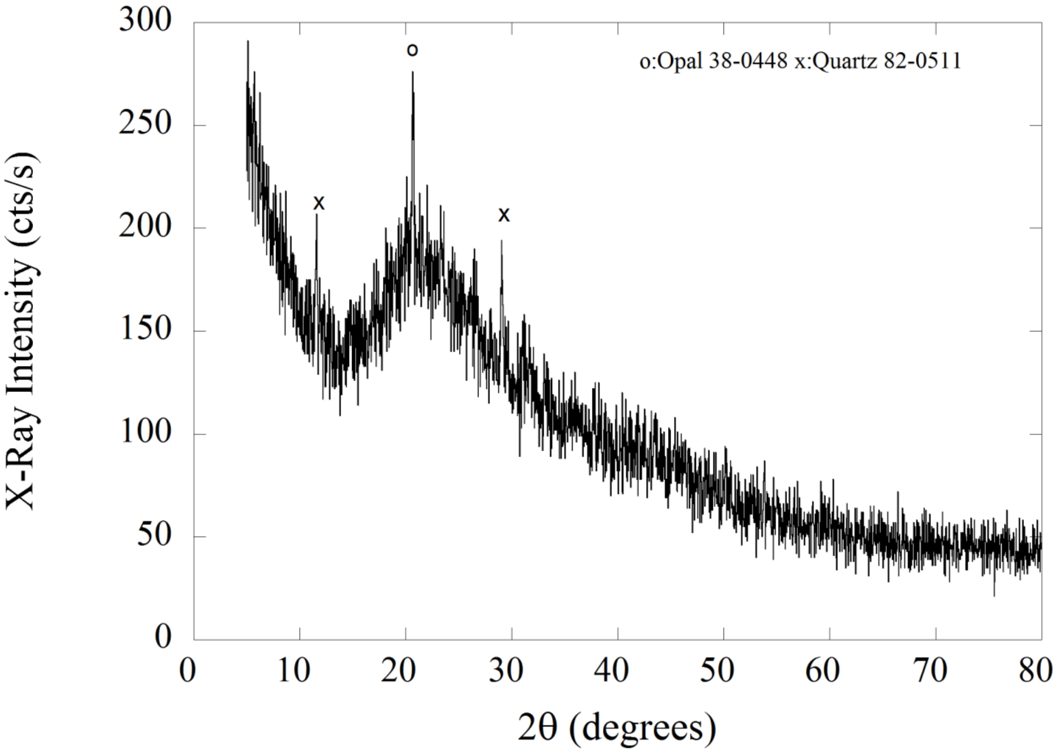

Figure 5.5. XRD spectra of *Pseudo-nitzschia delicatissima* diatom species after nitric acid digestion.

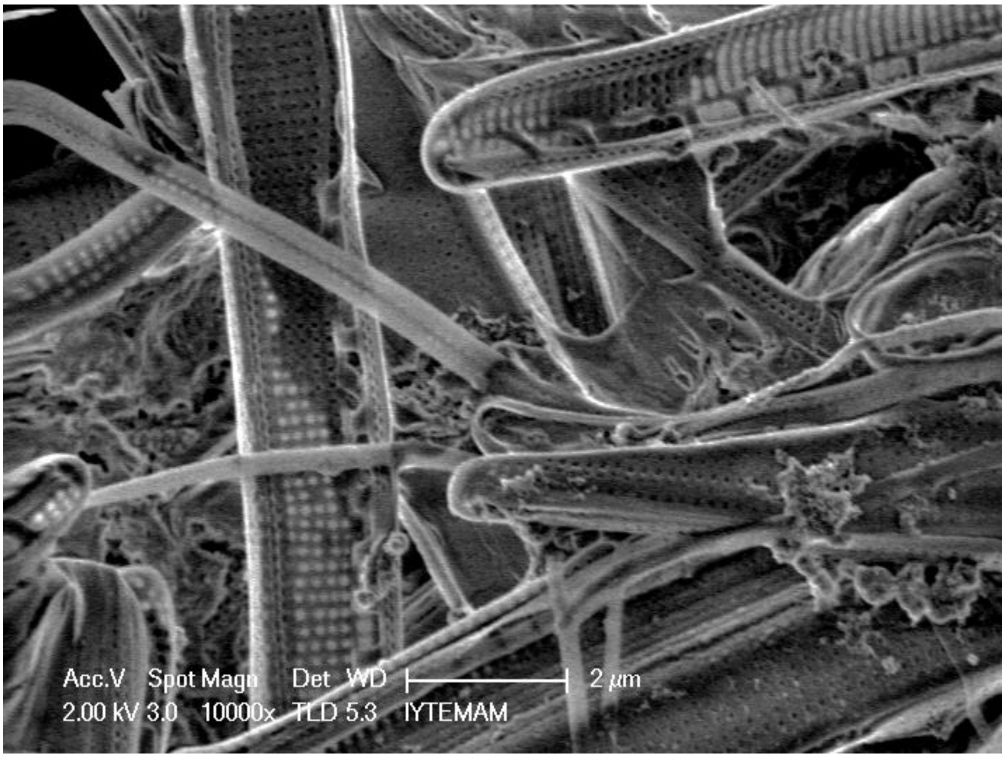

(a)

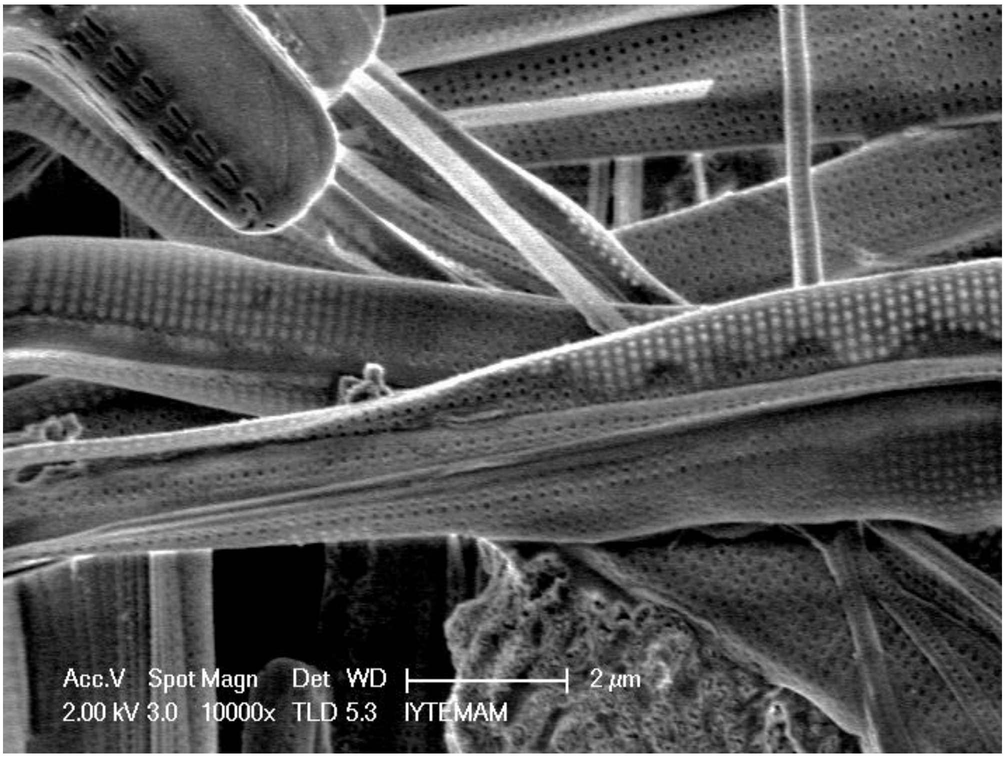

(b)

Figure 5.6. The SEM images of Pseudo-*nitzschia delicatissima* diatom frustules after the nitric acid digestion, (a) 10000x and (b) 10000x.

The FT-IR analysis of Pseudo-*nitzschia delicatissima* diatom frustules after nitric acid digestion is shown in Figure 5.7. As tabulated in Table 5.4, the peaks at 463.48, 545.08, 953.14 and 1080.11 cm^{-1} correspond to Si-O bonding, while the peak at 798.99 cm^{-1} to Si-O-Si bonding. The other peaks are taught to be residual organic structural peaks which cannot be removed with acid treatment (Table 5.3).

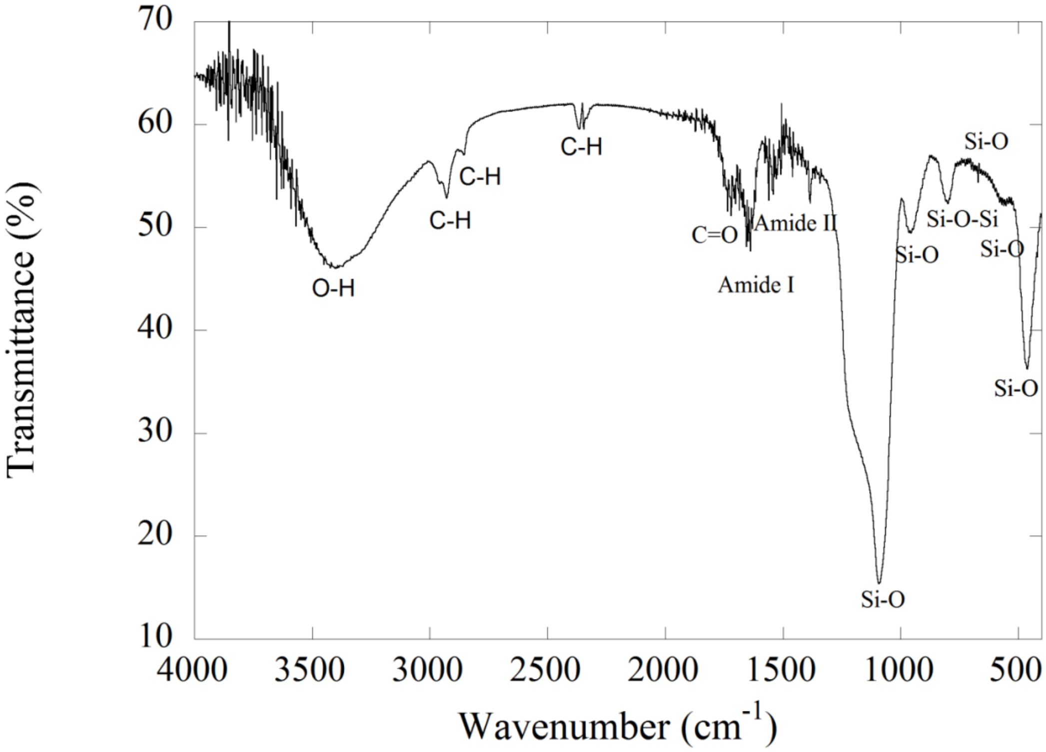

Figure 5.7. FT-IR analysis of *Pseudo-nitzschia delicatissima* after nitric acid digestion.

Table 5.4. FT-IR peaks of *Pseudo-nitzschia delicatissima*

Wavenumber (cm^{-1})	**Chemical Bonding**
~463,48	Si-O
~545,08	Si-O
~672,04	Si-O
~798,99	Si-O-Si
~953,14	Si-O
~1080,11	Si-O
~1216,12	P=O
~1543,56	Amide II
~1642,31	Amide I
~1732,98	C=O
~2306	C-H
~2857,43	C-H
~2920,907	C-H
~3400	O-H

Nitric acid is a strong acid and the residual salts from the culture environment of diatoms dissolve in nitric acid. The chemical reactions between nitric acid and NaCl, CaO and MgO are sequentially as,

$$\mathbf{NaCl + HNO_3 \rightarrow HCl + NaNO_3} \tag{5.1}$$

$$\mathbf{CaO + 2\ HNO_3 \rightarrow Ca(NO_3)_2 + H_2O} \tag{5.2}$$

$$\mathbf{MgO + 2\ HNO_3 \rightarrow H_2O + Mg(NO_3)_2} \tag{5.3}$$

After the chemical reactions, the nitrates, HCl and water form. Nitrates and HCl are soluble in the water. Thus, the salts are removed when the centrifuge is applied. There is no reaction between SiO_2 and nitric acid as SiO_2 is only soluble in HF and alkalies (80-100^{o}C) [62]. Hence, the siliceous frustules are not destructed by the nitric acid treatment. Also, the organic component of the frustule is solved in the nitric acid by the following reaction [63],

$$\mathbf{C + 4\ HNO_3 \rightarrow CO_2 + 4\ NO_2 + 2\ H_2O} \tag{5.4}$$

The obtained powder color is white (see Figure 4.11-d) due to not existing oxide components much. The XRD spectra of *Pseudo-nitzschia delicatissima* diatom frustules after nitric acid digestion proved that no crystalline structures of halides existed. The SEM images of cleaned *Pseudo-nitzschia delicatissima* frustules also showed that I destructions of the frustules occurred after nitric acid digestion. Also, the structures observed in SEM were well matched with those of *Pseudo-nitzschia* family in the literature [64]. The FT-IR analysis of *Pseudo-nitzschia delicatissima* after nitric acid digestion is also well matched with that of the diatoms cleaned with nitric acid [65].

5.1.2. *Achnanthes taeniata* Diatom Frustules

The chemical composition of *Achnanthes taeniata* diatom frustules after nitric acid digestion is very much similar to that of *Pseudo-nitzschia delicatissima* diatom as tabulated in Table 5.5. The silica content of *Achnanthes taeniata* diatom frustules is however slightly lower, 81%. The XRD spectra show that *Achnanthes taeniata* frustules silica has amorphous opal-A structure as shown in Figure 5.8. The SEM images of *Achnanthes taeniata* diatom frustules are shown in Figures 5.9. The length and width of *Achnanthes taeniata* diatom frustules range between 5 µm and 12 µm and 3 and 4 µm, respectively. The size of the pores on the frustule walls ranges between 100 nm and 200 nm.

Table 5.5. XRF analysis of *Achnanthes taeniata* diatom species after nitric acid digestion

Component	**Na_2O**	**MgO**	**SiO_2**	**P_2O_5**	**SO_3**	**Cl**	**K_2O**	**CaO**
Concentration (%)	1.1	1.4	81	<1	<1	<1	<1	<1

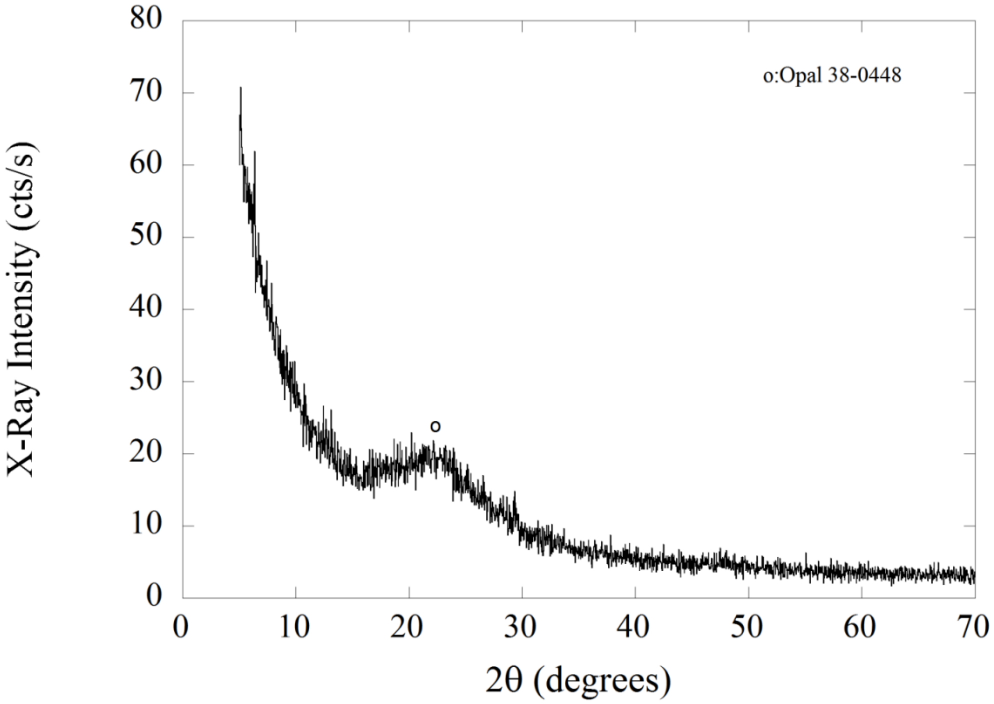

Figure 5.8. The XRD spectra of *Achnanthes taeniata* diatom frustules after nitric acid digestion.

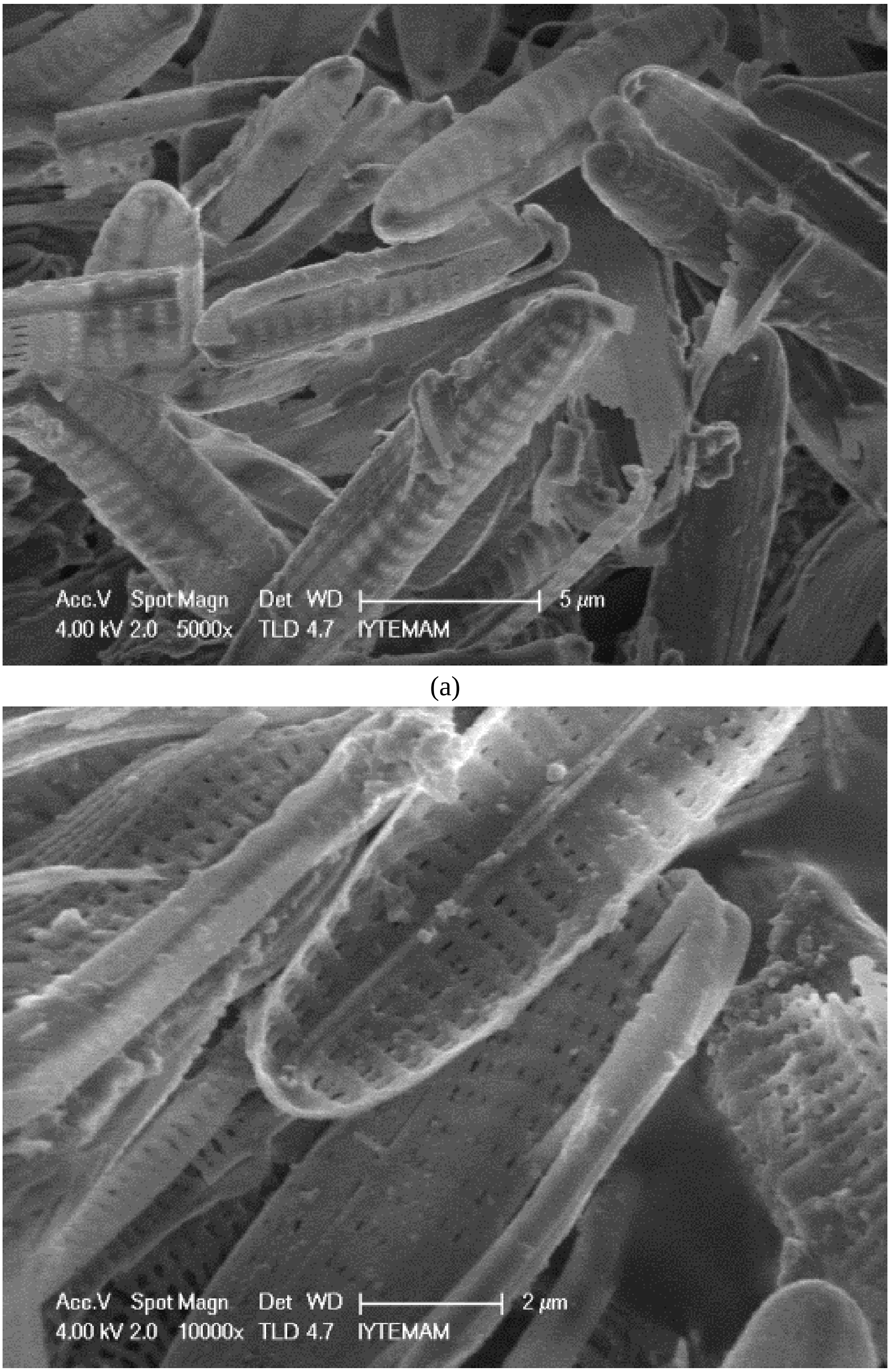

(a)

(b)

Figure 5.9. SEM images of *Achnanthes taeniata* diatom frustules after nitric acid digestion (a) 5000x and (b) 10000x.

The FTIR analysis of *Achnanthes taeniata* diatom frustules is shown in Figure 5.10. Peaks at 468.11, 548.11, 857.29, 844.86 and 1081.08 cm^{-1} correspond to the Si-O bonding, the peak at 779.45 cm^{-1} to Si-O-Si bonding (Table 5.6). The remaining peaks are taught to be due to residual organics in the powder (Table 5.6). Lastly, the SEM, XRD, XRF and FT-IR analyses of *Achnanthes taeniata* diatom frustules cleaned with nitric acid are also matched with literature [46, 65-67].

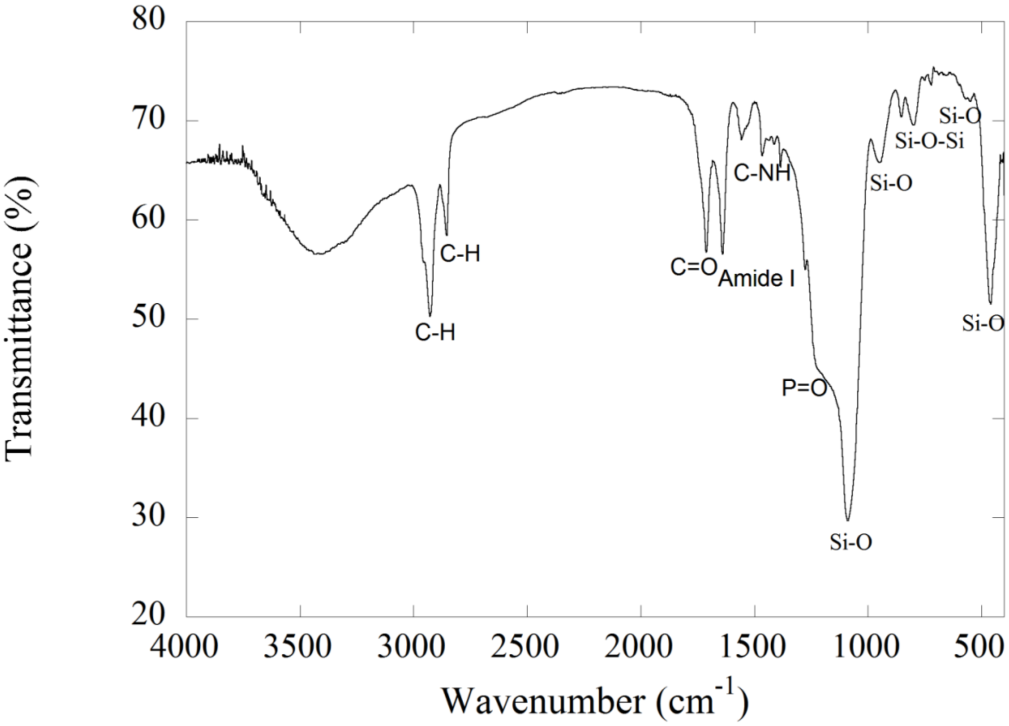

Figure 5.10. FT-IR analysis of *Achnanthes taeniata* diatom frustules after nitric acid digestion.

Table 5.6. FT-IR peaks of *Achnanthes taeniata* diatom frustules

Wavenumber (cm^{-1})	**Chemical Bonding**
~468.11	Si-O
~548.11	Si-O
~779.45	Si-O-Si
~857.29	Si-O
~944.86	Si-O
~1081.08	Si-O
~1227.02	P=O
~1470.27	C-NH
~1557,83	C-NH
~1635.67	Amide I
~1713.51	C=O
~2857.43	C-H
~2923.73	C-H

5.1.3. *Amphora coffeaeformis* Diatom Frustules

The XRF analysis of *Amphora coffeaeformis* diatom frustules after 2 h nitric acid digestion results in an SiO_2 content of 79% and an MgO content of 1.2%. The silica is again in amorphous opal-A form (Figure 5.11). The length and width of *Amphora coffeaeformis* diatom frustules shown in Figures 5.12 (a-c) range between 10 and 15 µm and 3 and 5 µm, respectively. The FTIR analysis of *Amphora coffeaeformis* diatom frustules is shown in Figure 5.13. Different from Pseudo-*nitzschia delicatissima* and *Achnanthes taeniata* diatom frustule, *Amphora coffeaeformis* diatom frustules do not show organic bonding peaks, confirming that nitric acid digestion completely remove the organic components (Table 5.7). Interaction of diatoms with nitric acid was changed as 2 hours for Amphora coffeaformis. This interaction change did not affect XRD, XRF and SEM results. However, FT-IR results were affected by this interaction change. Lesser organic peaks were observed due to the change of holding time [68]. Increasing the interaction time solved more organic matter. It can be said that 2 hours of interaction is appropriate for this cleaning method. The SEM images and XRD and XRF results were well agreed with the literature [46, 66].

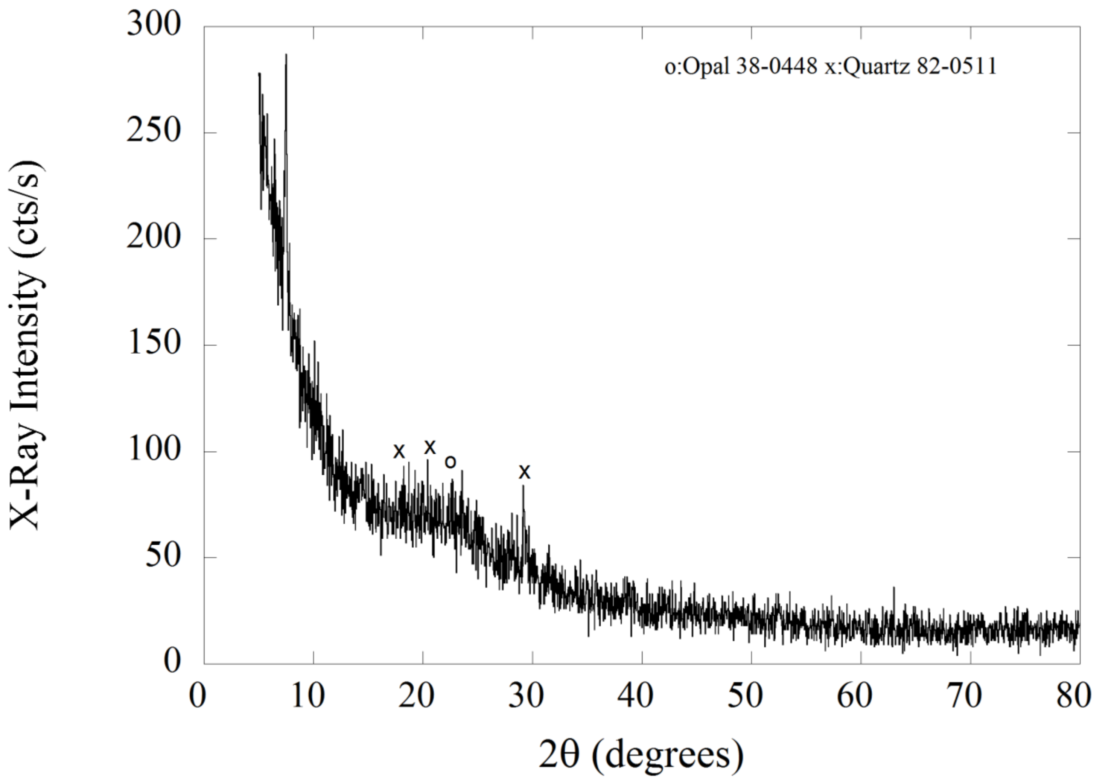

Figure 5.11. XRD patterns of *Amphora coffeaeformis* diatom frustules after nitric acid digestion.

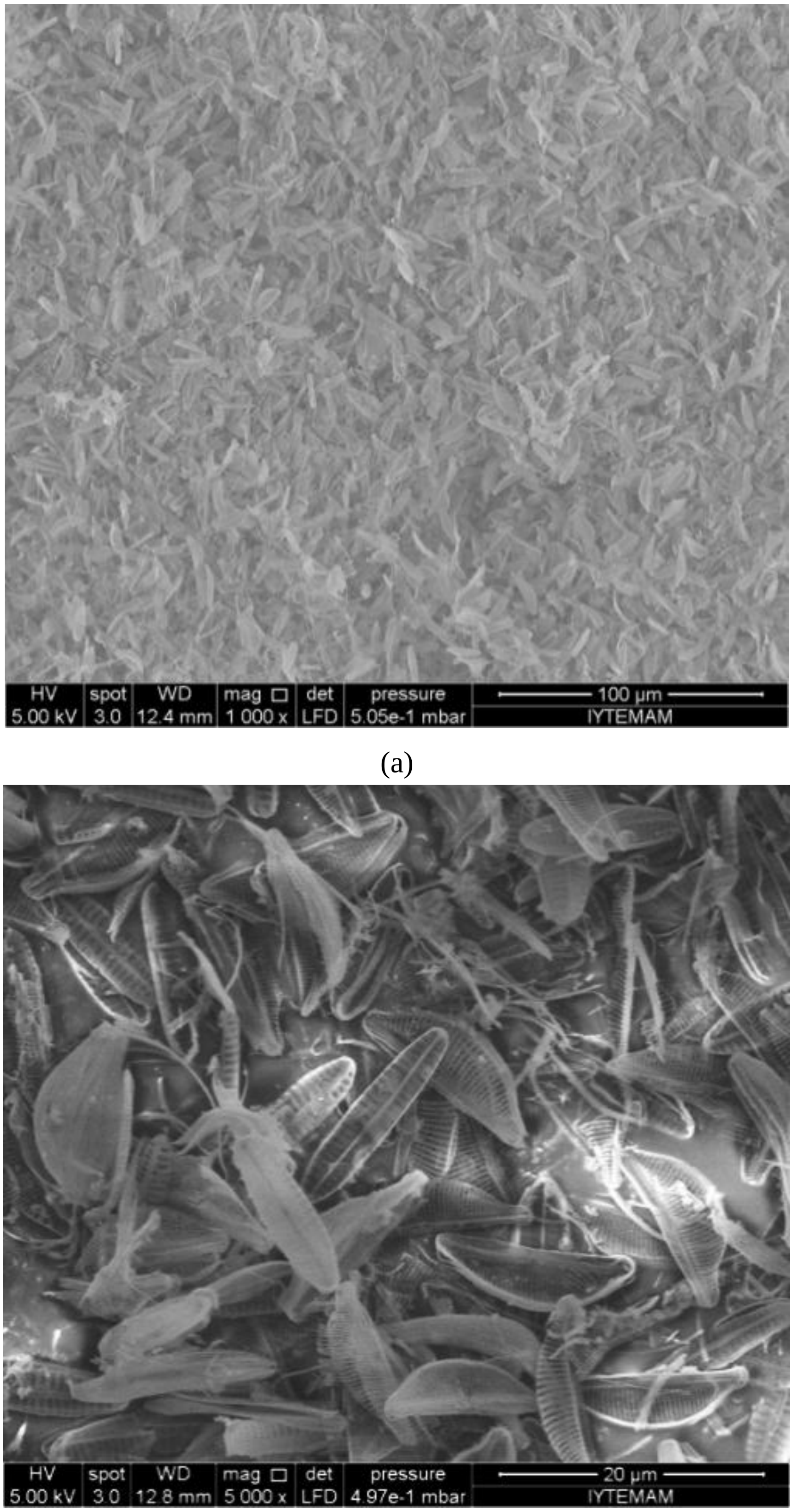

(a)

(b)

Figure 5.12. SEM images of *Amphora coffeaeformis* diatom frustules after nitric acid digestion in different magnification ratios (a)1000x (b) 5000x (c) 20000x.

(cont. on next page)

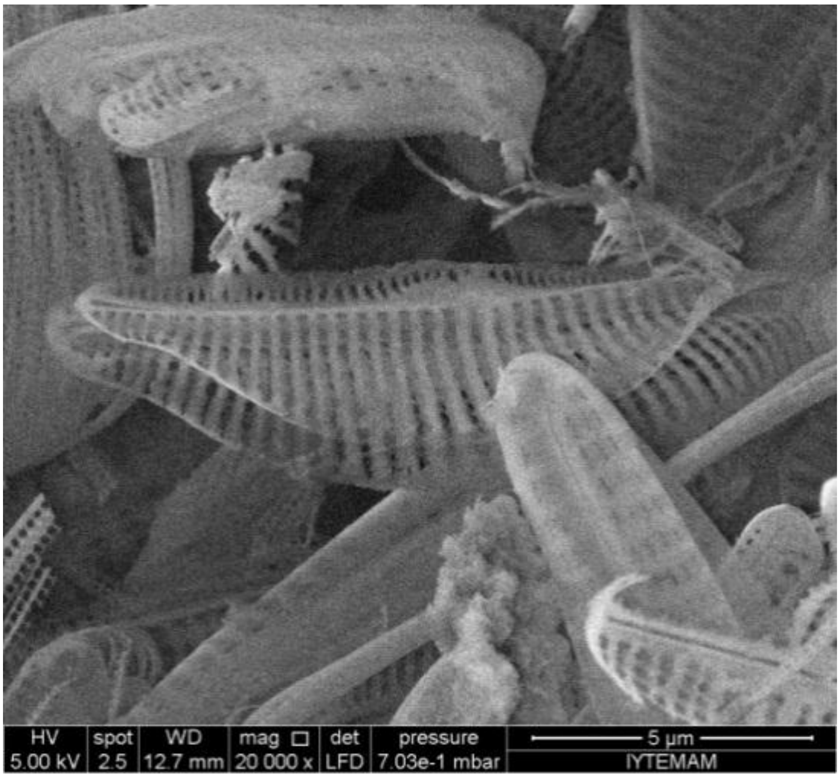

(c)

Figure 5.12. (cont.)

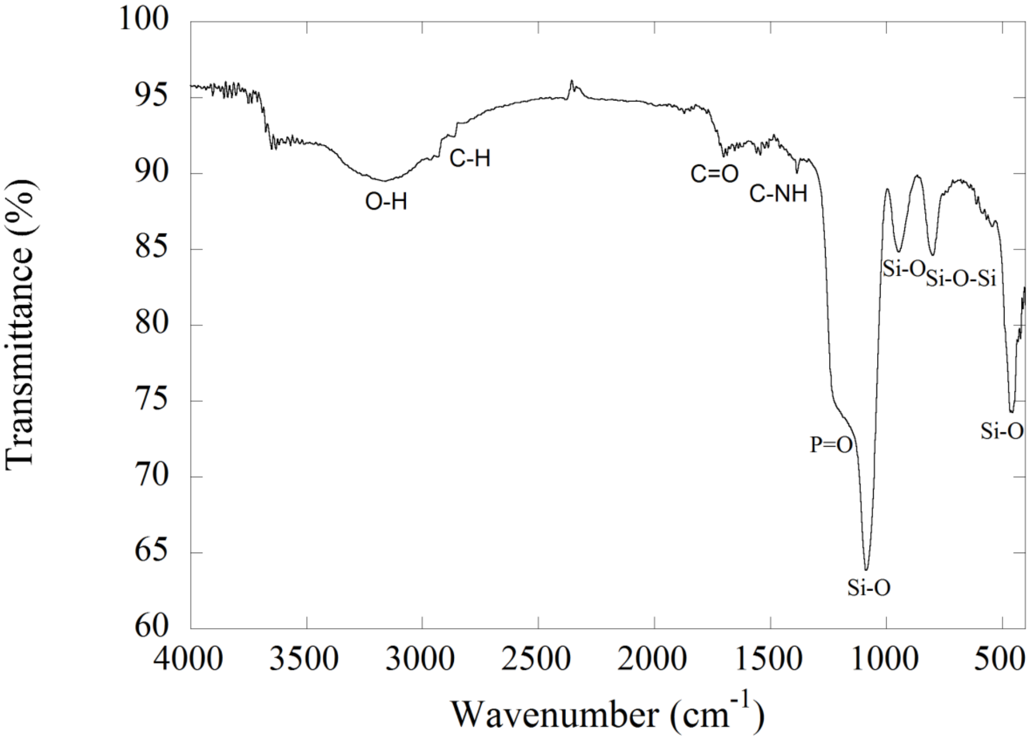

Figure 5.13. FT-IR analysis of *Amphora coffeaeformis* diatom frustules after nitric acid digestion.

Table 5.7. FT-IR peaks of *Amphora coffeaeformis* diatom frustules

Wavenumber (cm^{-1})	Chemical Bonding
~460	Si-O
~789	Si-O-Si
~931	Si-O
~1084	Si-O
~1227,02	P=O
~1369	C-NH
~1545	C-NH
~1701	C=O
~2850	C-H
~3150	O-H

5.1.4. *Cylindrotheca closterium* Diatom Frustules

The XRD spectra of *Cylindrotheca closterium* after nitric acid digestion are shown in Figure 5.14. The silica is found in amorphous opal-A and quartz form as depicted in Figure 5.14. *Cylindrotheca closterium* frustule consists of 80% silica and less than 1% Mg, Cl and Na. The SEM images of *Cylindrotheca closterium* diatom frustules after acid digestion are shown in Figures 5.15 (a) and (b). The width of *Cylindrotheca closterium* diatom frustules is 85nm on the average after nitric acid digestion.

The XRD, XRF and SEM results of *Cylindrotheca closterium* diatom frustules were also well matched with literature [46, 66, 69]. These diatom species resemble nano-fibers and their extraordinary forms could be very important for nano material processing and characterization. *Cylindrotheca closterium* diatom frustule filled epoxy composites could not be processed with epoxy matrix due to difficult in obtaining homogeneous mixing.

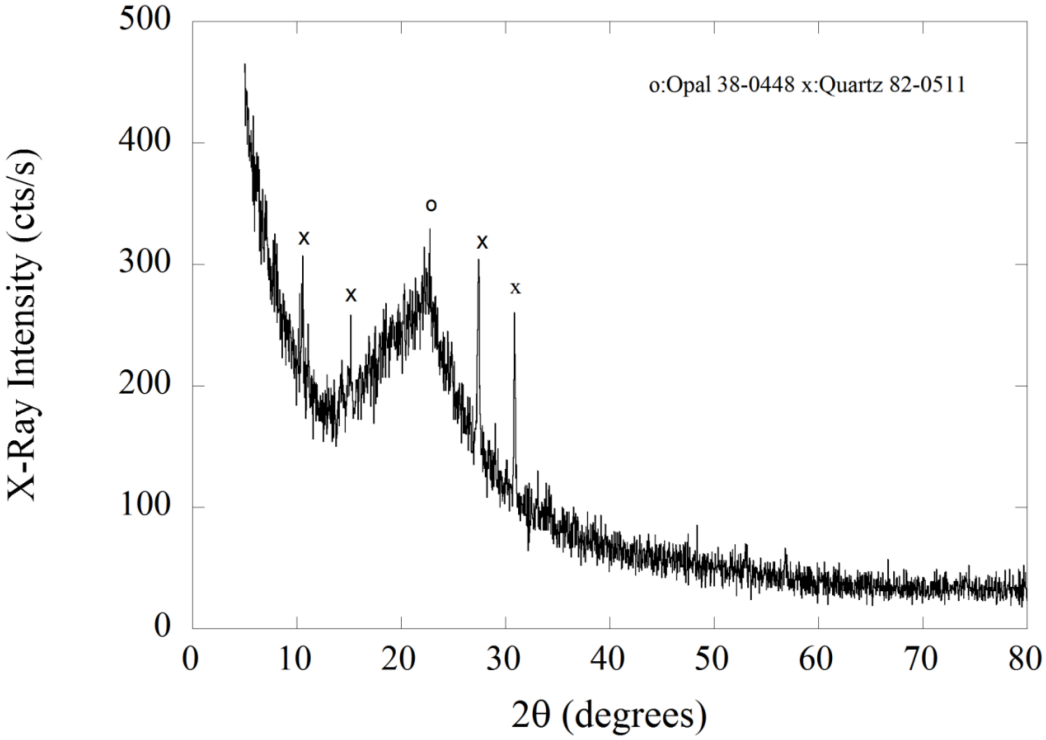

Figure 5.14. XRD patterns of *Cylindrotheca closterium* diatom frustules after nitric acid digestion.

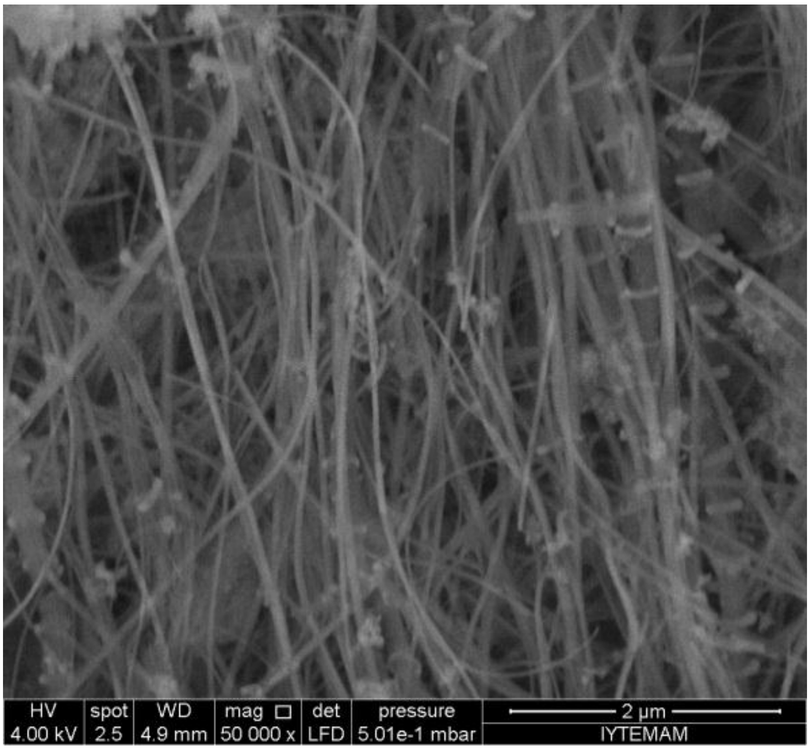

(a)

Figure 5.15. SEM images of *Cylindrotheca closterium* diatom frustules after nitric acid digestion (a)50000x and (c)100000x.

(cont. on next page)

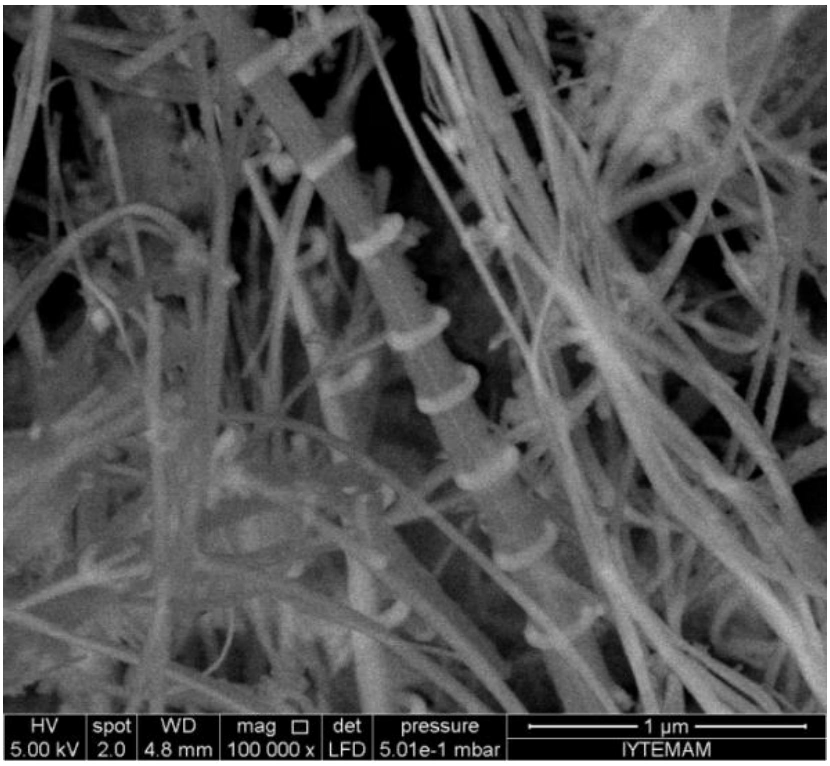

(b)

Figure 5.15. (cont.)

5.1.5. Characterization of the Commercial Diatomaceous Earth

The XRF analyses showed that the commercial diatomaceous earth powder consisted of 90% of SiO_2, %5 of Al_2O_3, 1.5% of Fe_2O_3, %1 of MgO, and 0.5% of CaO. The pictures of untreated and heat treated (700, 800, 900, 1000, 1100, and 1200^oC) commercial diatomaceous earth powders are shown Figure 5.16. The powder color changes from grey to pink after heat treatment process.

The XRF analysis of natural diatomite was well-matched with the literature [66]. The powder color of diatomite powder with heat treatment changed from grey to pink due to the oxidation of iron in the raw material with increasing the temperature and elemental iron transformed into Fe_2O_3 compound [70, 71].

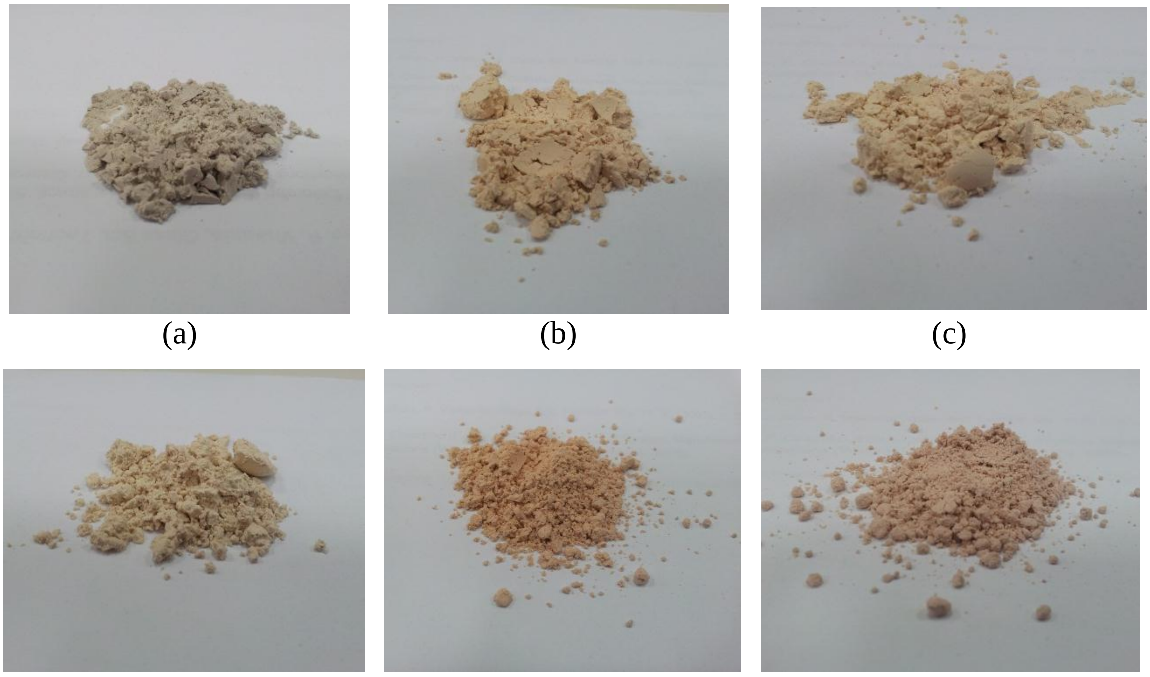
(a) (b) (c)

(d) (e) (f)

Figure 5.16. The pictures of (a) non-heat treated and heat treated commercial diatomaceous earth at (b) 700^{o}C (c) 800^{o}C (d) 900^{o}C (e)1000^{o}C and (f) 1200^{o}C.

The XRD spectrum of non-heat treated commercial diatomaceous earth powder is shown in Figure 5.17. The silica structure is amorphous in opal (Ref. 38-0448) and quartz (Ref. 82-0511) form. The XRD spectra of heat-treated commercial diatomite at different temperatures are shown in Figure 5.18. The amorphous to crystalline transition temperature is determined 1000^{o}C and silica structure shifts from quartz to cristobalite form. FTIR analysis of the non-heat treated commercial diatomite is shown in Figure 5.19. The peaks at 779 cm^{-1} and 1025 cm^{-1} belong to Si-O-Si chemical bonding. FTIR analyses of commercial diatomaceous earth heat treated powder are shown in Figure 5.20. A new peak was observed in the sample heat treated at 1000^{o}C at around 610 cm^{-1} wavenumber. This peak was also observed at 1200^{o}C.

The XRD spectrum of non-heat treated commercial diatomite is well matched with the literature [46]. According to the Figure 5.18, X-Ray Intensity at 21^{o} increases with increasing the temperature. Also, opal and quartz form silica transformed into cristobalite form. The FT-IR analysis of heat treated natural diatomite samples showed the same characteristic silica peaks at 470, 790 and 1090 cm^{-}1. The FT-IR analysis of heat treated diatomite powders showed a new peak occurred at 1000^{o}C due to the fact that crystal structure of the powder transformed from amorphous to crystalline and the typical of cristobalite phase. The bands at the intervals between 1896 cm^{-1} and 2274 cm^{-1} refer to the presence of CO_2 in the medium. (Figure 5.20) [71, 72].

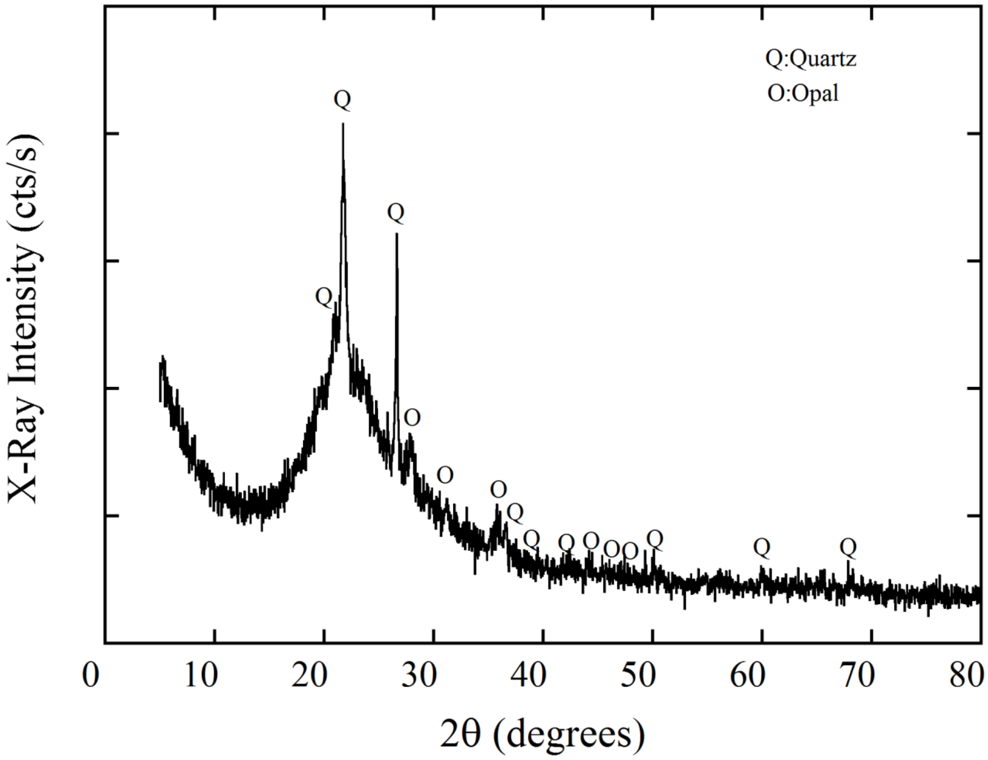

Figure 5.17. The XRD spectrum of non-heat treated commercial diatomaceous earth powder.

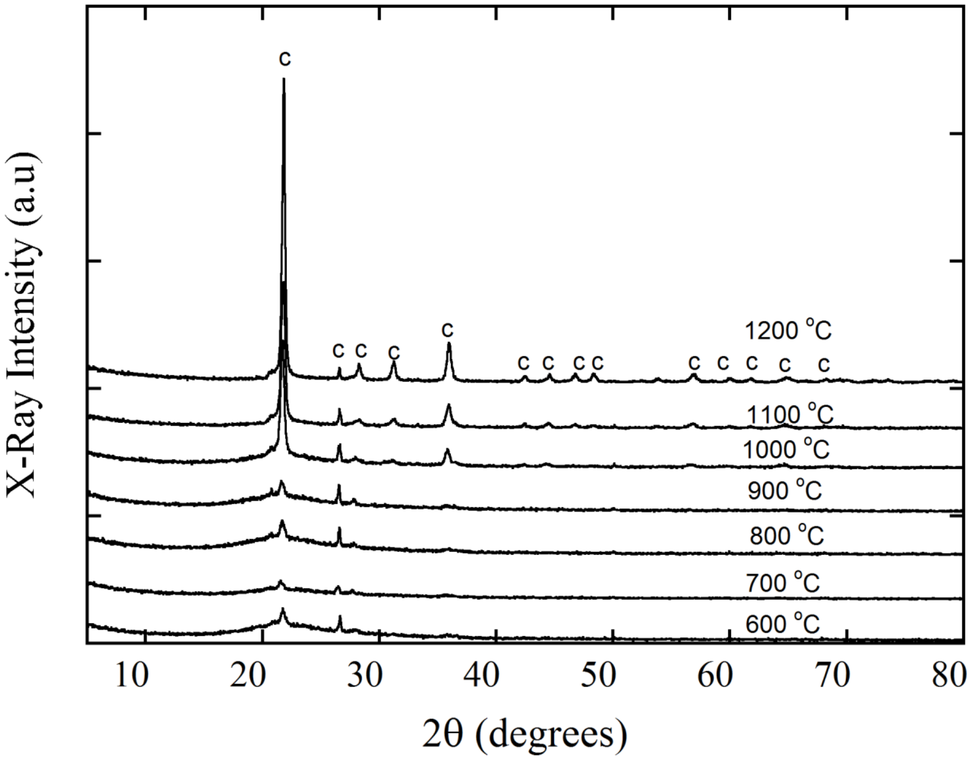

Figure 5.18. XRD spectrum of heat treated commercial diatomite at different temperatures (C: cristobalite).

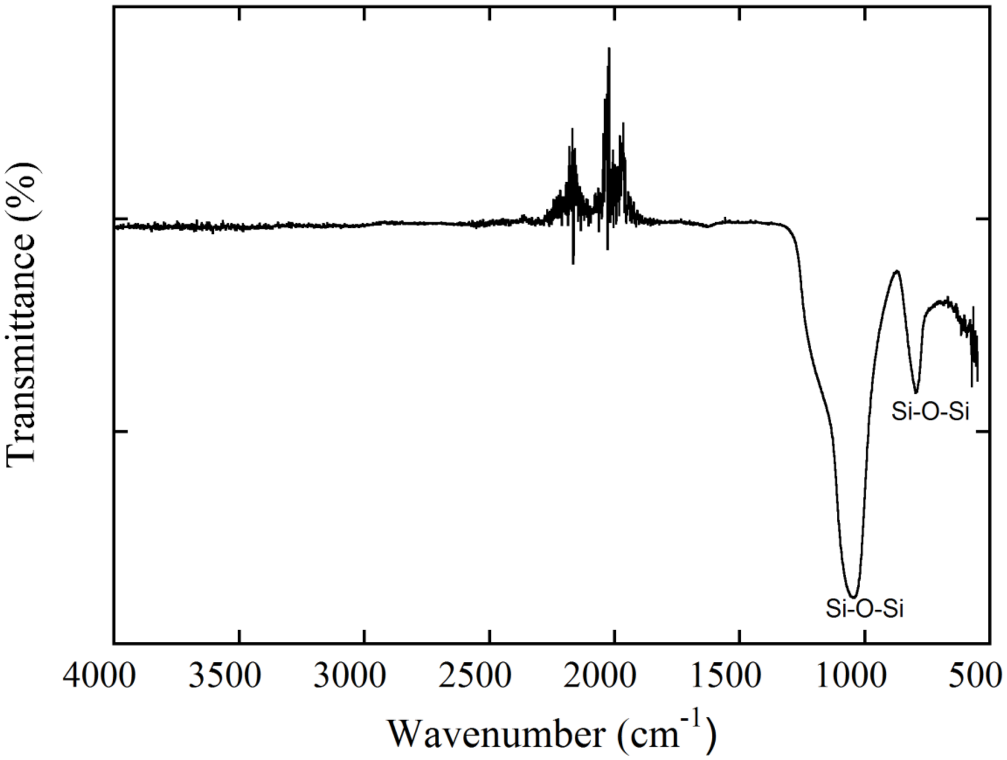

Figure 5.19. FTIR analysis of non-heat treated commercial diatomite powder.

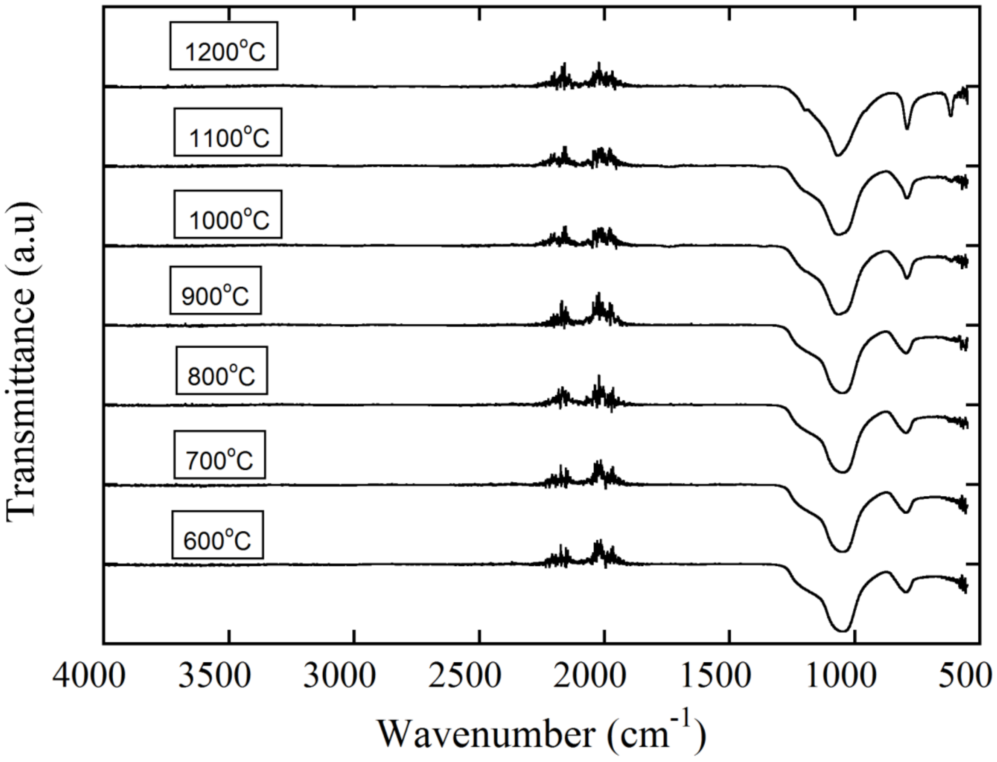

Figure 5.20. FTIR analysis of heat treated commercial diatomaceous earth powder.

The powder size analysis (Figure 5.21) shows that ninety percent of the ND frustules diameters are less than or equal to 54.4 µm, 10% is less than or equal to 3.9

μm and the mean size of frustules are 16.8 μm. The SEM images of non-heat treated and heat treated diatomaceous earth samples are shown in Figures 5.22(a-x).

As received diatomaceous earth powder are composed of different frustules types, pennate and centric types of diatoms. The crushed frustule pieces are seen in the same pictures and mainly resulted from the milling operation applied by the producer. It is further noted that heat treatment at 1100 and 1200°C results in agglomeration of the powder as depicted in Figures 5.22(s) and (v). The pore diameter is measured to change between 200 and 1000 nm depending of the species of diatom frustules. In the SEM images of heat treated diatomite samples, the pores of the frustules can be clearly seen in the sample heat-treated at 600, 700, 800, 900 and 1000°C and the destruction of the pores did not occur at these temperatures (Figure 5.21-a-o). After 1000°C, the collapse of the pores can be seen at 1100°C and 1200°C. This collapse is due to the fact that the surface of the frustules initiates to melt. The melting of surfaces was attributed by the complete dehydration process of diatomite structure with increasing the temperature [73].

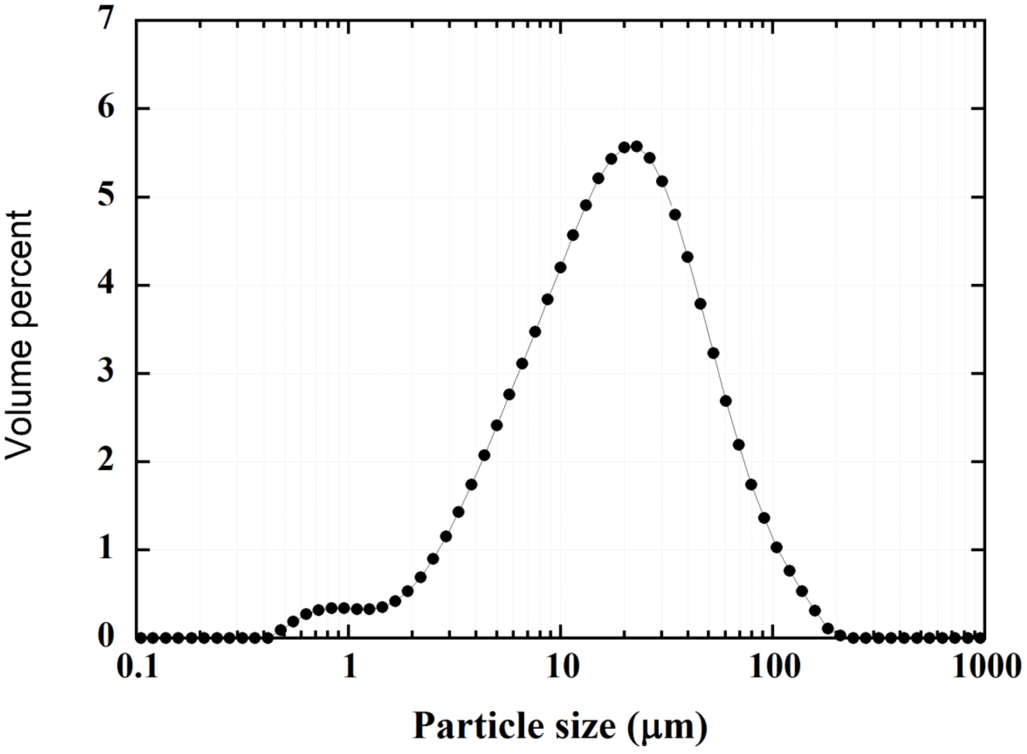

Figure 5.21. The particle size distribution of ND frustules.

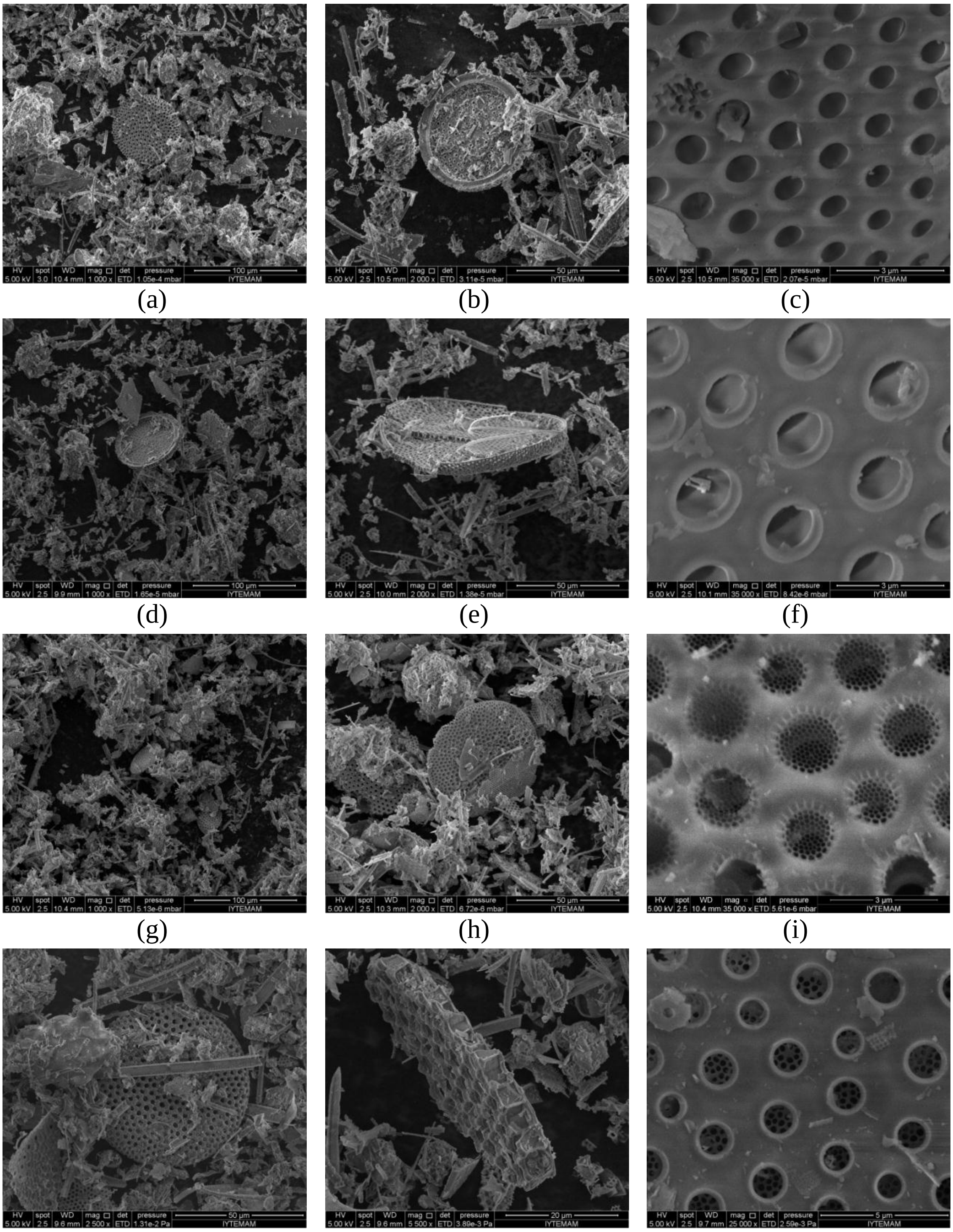

(a) (b) (c)

(d) (e) (f)

(g) (h) (i)

(j) (k) (l)

Figure 5.22. SEM images of the non-heat treated commercial diatomaceous (a-c) and heat treated at 600°C (d-f), 700°C (g-i), 800°C (j-l), 900°C (m-o), 1000°C (p-r), 1100°C (s-u), 1200°C (v-x).

(cont. on next page)

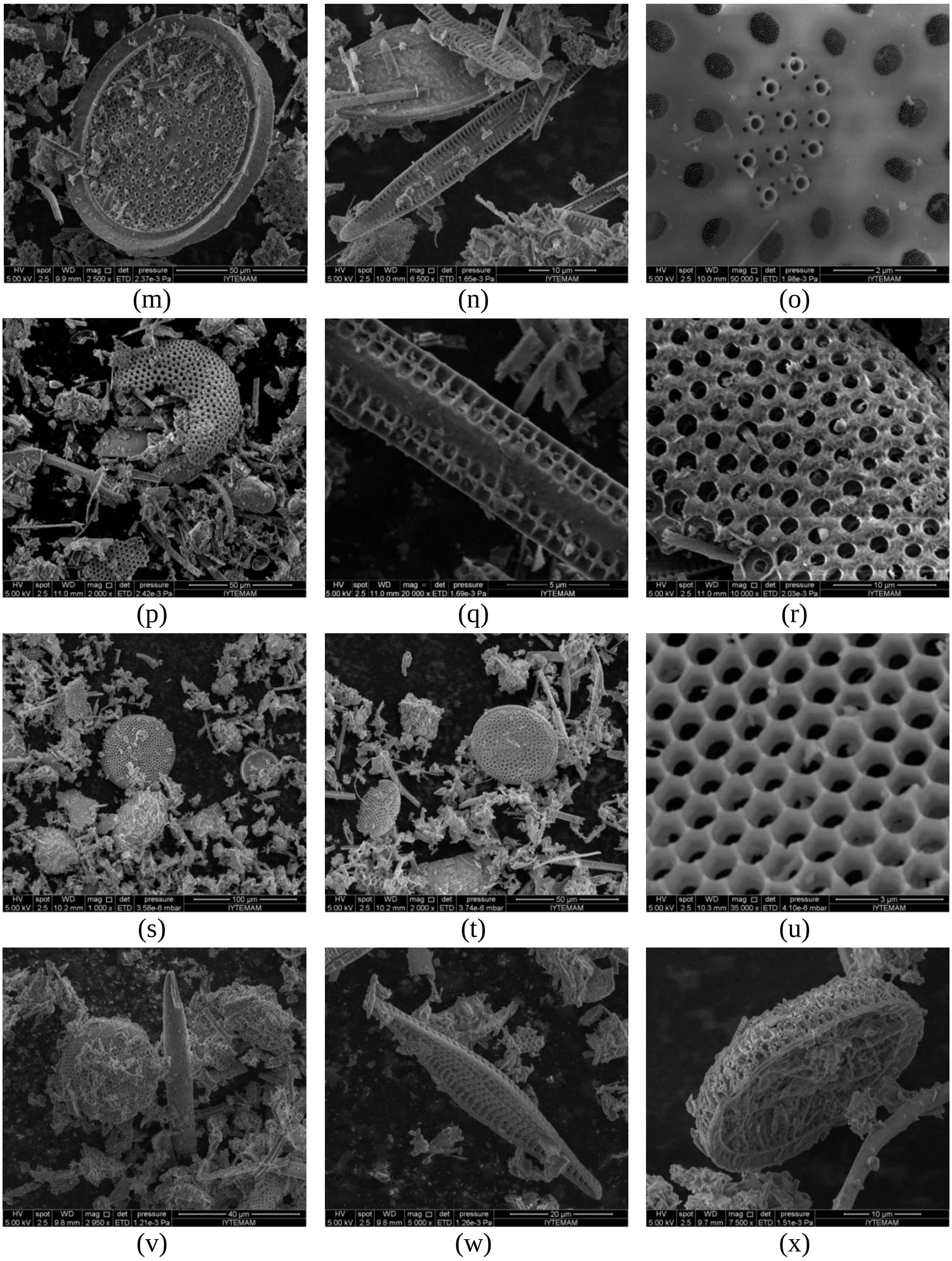

(m) (n) (o)

(p) (q) (r)

(s) (t) (u)

(v) (w) (x)

Figure 5.22. (cont.)

5.2. Mechanical Properties of Diatom Frustule Filled Epoxy

5.2.1. *Achnanthes taeniata* Frustule Filled Epoxy

The compression stress-strain curves of ND commercial diatomite frustule filled, *Achnanthes taeniata* frustule filled and unfilled epoxy are shown in Figures 5.23(a) and (b). The filler content of the filled epoxy is ~6 wt% and the filler *Achnanthes taeniata* frustules are obtained by nitric acid digestion. The compressive strengths of the filled and unfilled epoxies are further tabulated in Table 5.8. The filling epoxy matrix with ND commercial diatomite *and Achnanthes taeniata* frustule increases the compressive strength from about 60 MPa to 67 and 79 MPa on the average, respectively. A higher strengthening ~10 MPa and moduli with *Achnanthes taeniata* frustule addition is detected (Figure 5.23(b)). Figure 5.24 shows the SEM micrographs of the polished surface of *Achnanthes taeniata* frustule filled epoxy matrix composite samples. The picture was taken normal to the thickness of the plate (normal to the compression axis). The frustules are seen in the same picture are nearly randomly distributed on the plane. The long axes of the frustules are therefore almost normal to the compression axis, showing nearly planar random orientation. Figures 5.25(a) and (b) are the SEM micrographs of the surfaces of the compression tested and fractured samples. Both fractured and debonded frustules are seen in the fracture surfaces.

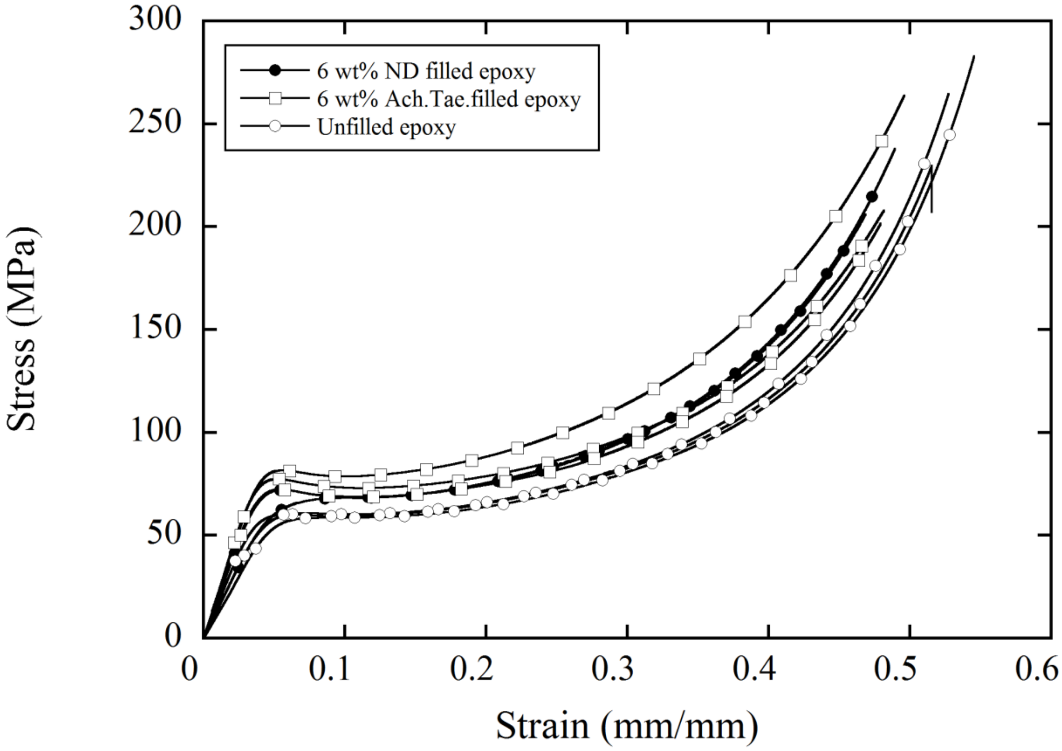

(a)

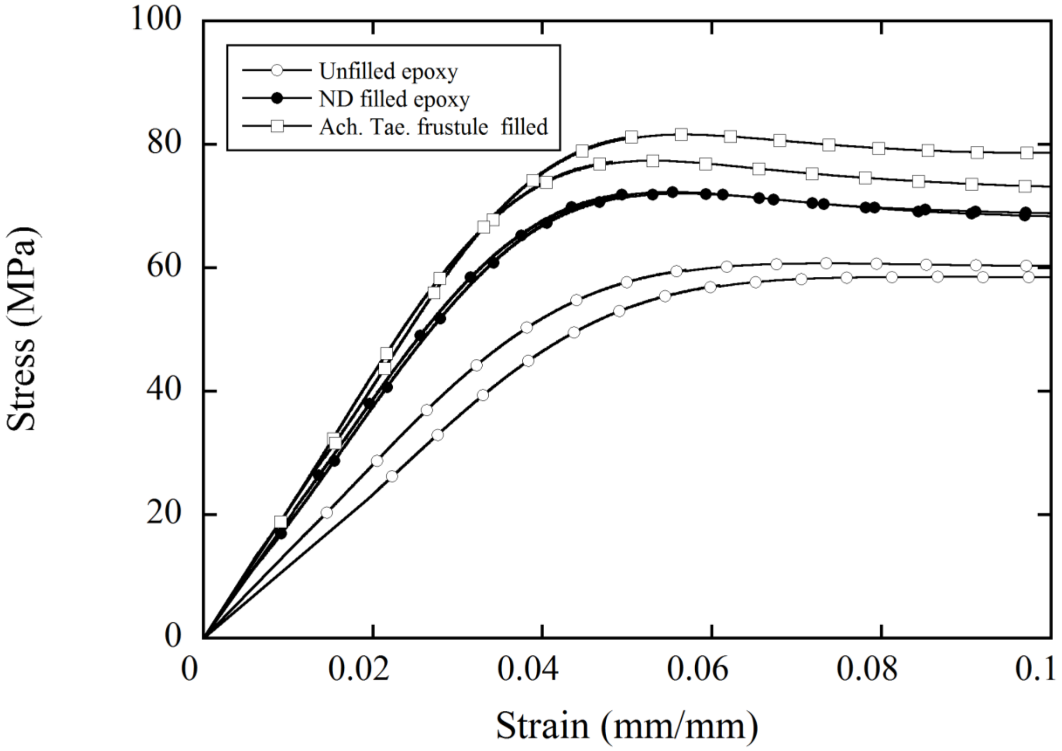

(b)

Figure 5.23. Comparison of 6.04 wt% *Achnanthes taeniata* frustule filled epoxy and 6.04 wt% diatomaceous earth filled epoxy.

Table 5.8. Compressive Strength values of *Achnanthes taeniata* frustule filled epoxy samples and commercial diatomite filled epoxy

Sample	**Compressive Strength (MPa)**
Unfilled epoxy	58
Unfilled epoxy	60
Unfilled epoxy	61
6.04 wt% ND filled epoxy Test-1	63
6.04 wt% ND filled epoxy Test-2	68
6.04 wt% ND filled epoxy Test-3	69
6.04 wt% *Achnanthes taeniata* frustule filled epoxy Test-1	83
6.04 wt% *Achnanthes taeniata* frustule filled epoxy Test-2	80
6.04 wt% *Achnanthes taeniata* frustule filled epoxy Test-3	73

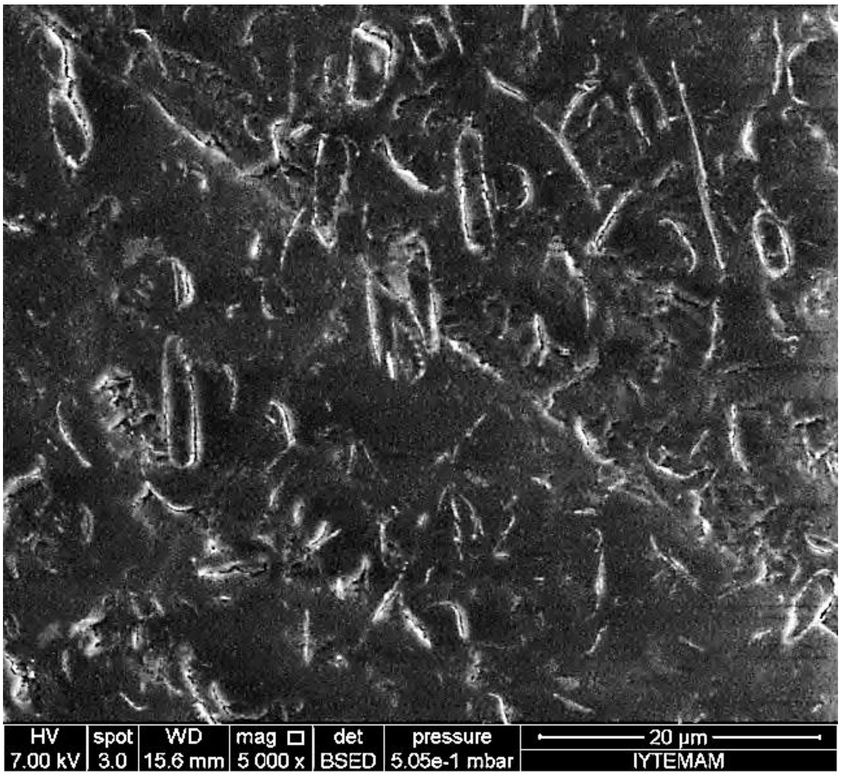

Figure 5.24. SEM micrographs of polished surface of *Achnanthes taeniata* filled epoxy matrix composite sample.

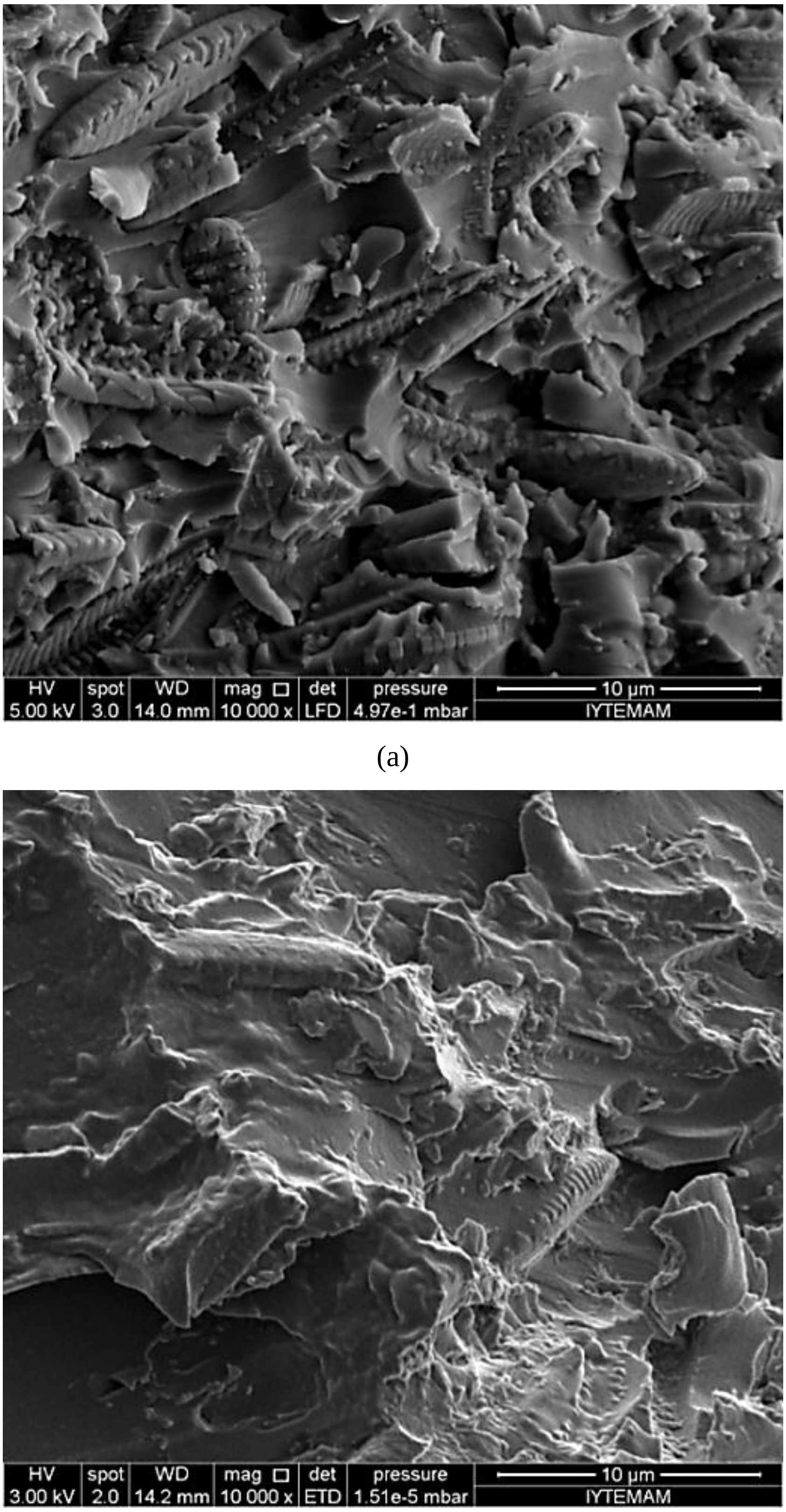

(a)

(b)

Figure 5.25. SEM fractographs of 6.04 wt% *Achnanthes taeniata* frustule filled epoxy (a) and (b)10000x.

5.2.2. Heat Treated Natural Diatomite Filled Samples

The compression stress-strain curves of neat epoxy and heat-treated frustule filled epoxy matrices are shown in Figure 5.26. The samples contain 15wt% of frustules. Heat treatment at 800^{o}C has no significant effect on the stress-strain behavior of the filled matrices, while heat treatment at 900^{o}C increases the stress values of the filled epoxy matrices, without any significant effect on the compressive strength. The heat treatment of frustules at 1000^{o}C however both increases compressive strength and stress values of the epoxy matrices. The compressive strength increased from 50 to 90 MPa with the heat-treatment, providing 50% of increase in the compressive strength of neat epoxy. Compressive strength however decreases with increasing heat treatment temperature after 1000^{o}C (Table 5.9). Figures 5.28(a-d) shows the SEM micrographs of the polished surfaces of heat treated diatomite frustule powder pores. It is noted that the pores are partially closed in the powder heat treated at 1100^{o}C (Figure 5.27(d)). The heat treatment at elevated temperatures tends to reduce the surface area. The epoxy infiltrates efficiently through the pores of the frustules. Figures 5.29(a-o) show the fracture surfaces of heat-treated diatom frustule powder filled epoxy samples. As seen in the same micrographs, the frustules heat treated at 800-1000^{o}C temperatures fracture into few pieces, while frustules heat treated at 1100 and 1200^{o}C fracture into many pieces in the tested filled composites. The fractures of frustules show essentially a good bonding between matrix and an efficient loading of the frustules during compression testing.

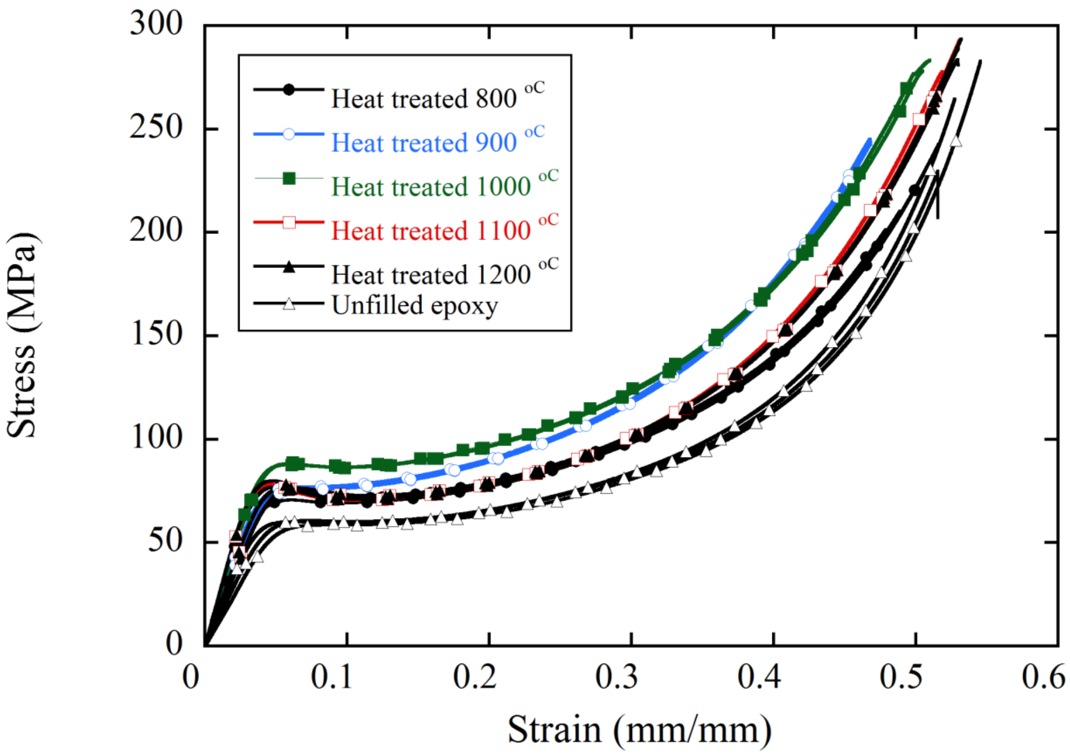

Figure 5.26. Comparison of heat treated diatomite filled epoxy samples and unfilled epoxy samples.

Table 5.9. Compressive Strength values of heat treated diatomite filled epoxy samples

Sample	**Compressive Strength (MPa)**
Unfilled epoxy	58
Unfilled epoxy	60
Unfilled epoxy	61
Heat Treated at 800°C Test-1	77
Heat Treated at 800°C Test-2	71
Heat Treated at 800°C Test-3	76
Heat Treated at 900°C Test-1	75
Heat Treated at 900°C Test-2	78
Heat Treated at 900°C Test-3	75
Heat Treated at 1000°C Test-1	89
Heat Treated at 1000°C Test-2	90
Heat Treated at 1000°C Test-3	90
Heat Treated at 1100°C Test-1	76
Heat Treated at 1100°C Test-2	78
Heat Treated at 1100°C Test-3	76
Heat Treated at 1200°C Test-1	77
Heat Treated at 1200°C Test-2	80
Heat Treated at 1200°C Test-3	79

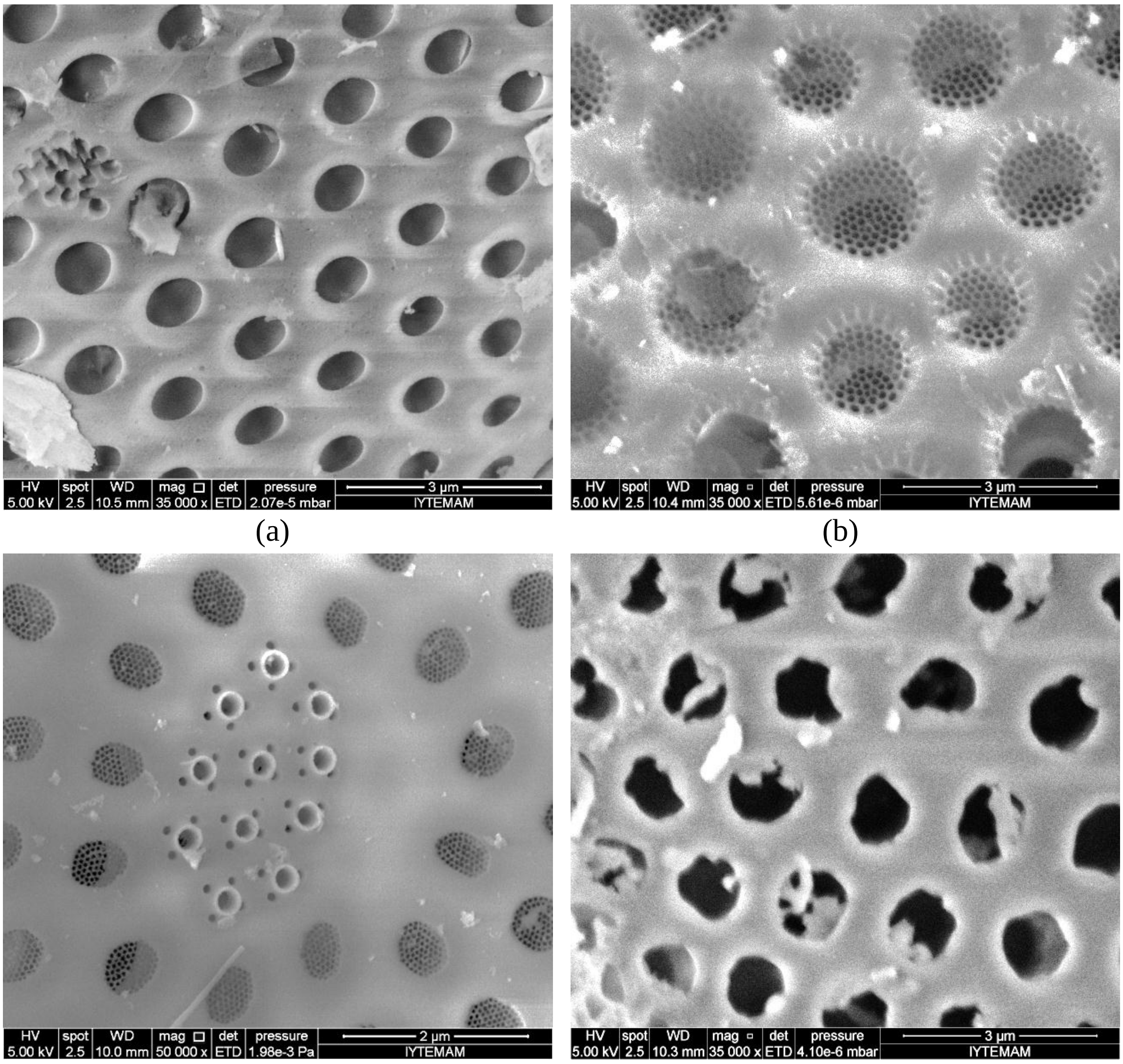

(a) (b)

(c) (d)

Figure 5.27. The SEM pictures of diatom frutules (a) unheat-treated and heat tretaed at (b)700°C, (c)900°C (c) 800°C and (d) 1100°C.

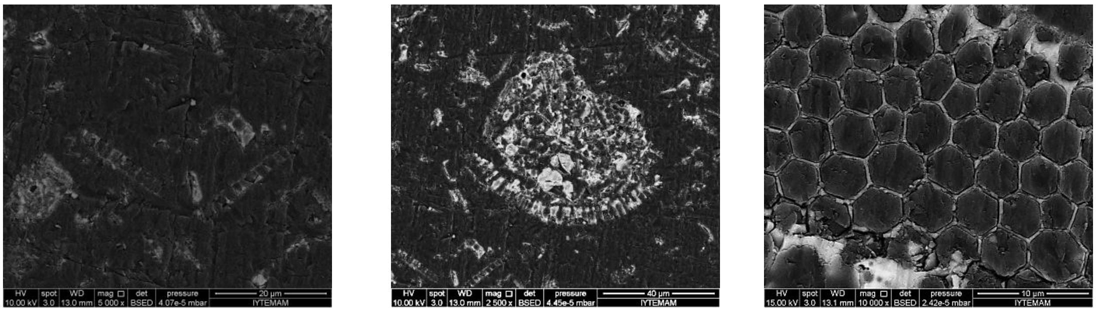

(a) (b) (c)

Figure 5.28. SEM micrographs of the polished surfaces of diatomite, heat treated at 800°C (a-c), 900°C (d-f), 1000°C (g-i), 1100°C (j-l), 1200°C (m-o), filled epoxy matrix composite samples.

(cont. on next page)

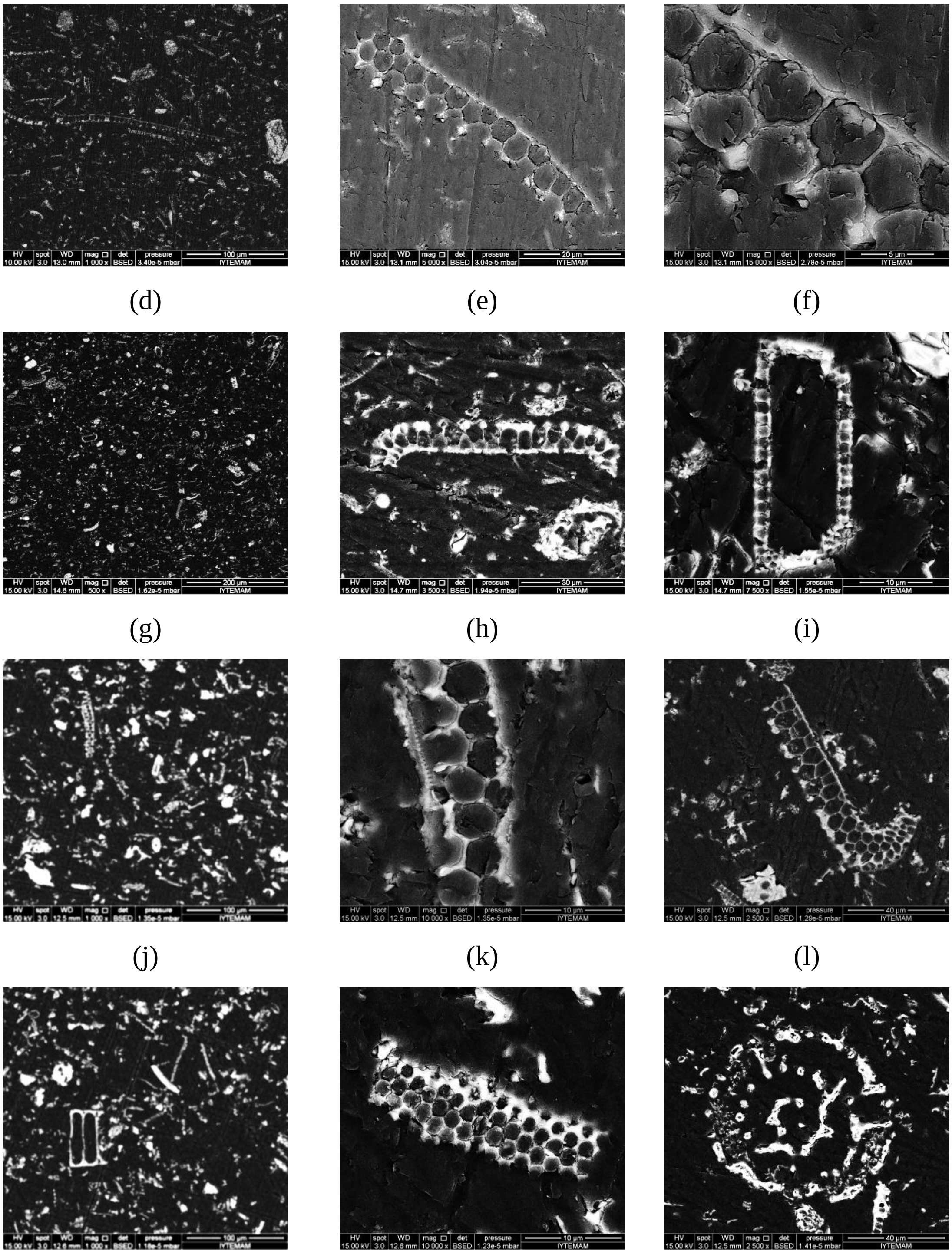

(d) (e) (f)

(g) (h) (i)

(j) (k) (l)

(m) (n) (o)

Figure 5.28. (cont.)

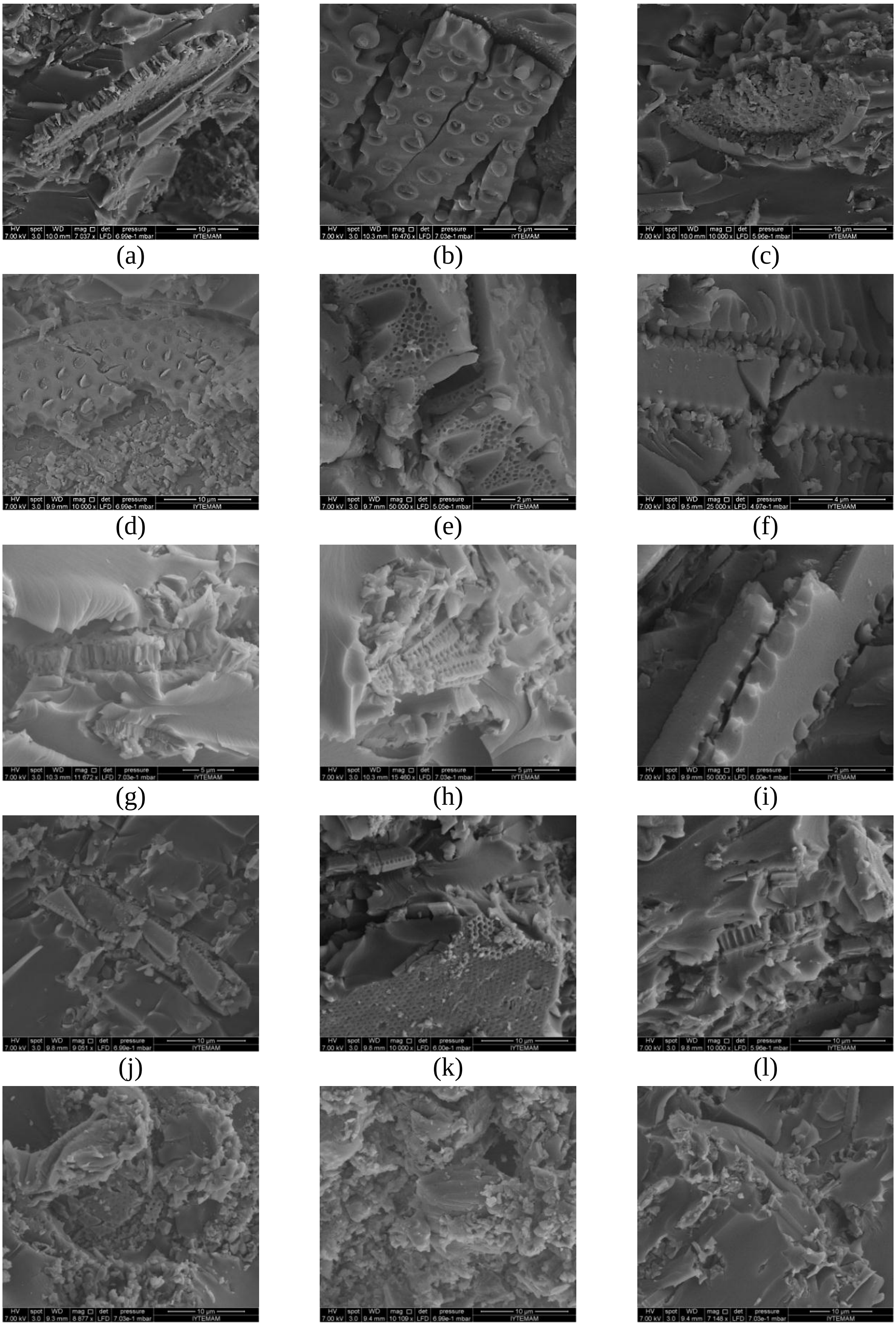

(a) (b) (c)

(d) (e) (f)

(g) (h) (i)

(j) (k) (l)

(m) (n) (o)

Figure 5.29. SEM fractographs of diatomite, heat treated at 800^{o}C (a-c), 900^{o}C (d-f), 1000^{o}C (g-i), 1100^{o}C (j-l), 1200^{o}C (m-o) filled epoxy composites from their fracture surfaces after compression tests done.

5.3. Prediction of Mechanical Behavior of Frustule Filled Polymer Matrix Composites

A typical stress-strain curve of polymer based material is shown in Figure 5.30. S_B corresponds to strength at break, γ_B corresponds to ultimate elongation (failure strain), S_y corresponds to yield strength, γ_y corresponds to elongation at yield and E corresponds to modulus of elasticity. Between A and B, Hooke's law is valid and the slope of this line gives modulus of elasticity. Stiffer materials have higher modulus. Point C corresponds to yielding point. Between C and D strain softening occurs and between D and E strain hardening occurs. Fracture occurs at the point E [74]. The whole compression test results were well suited with the typical stress-strain curve of polymers.

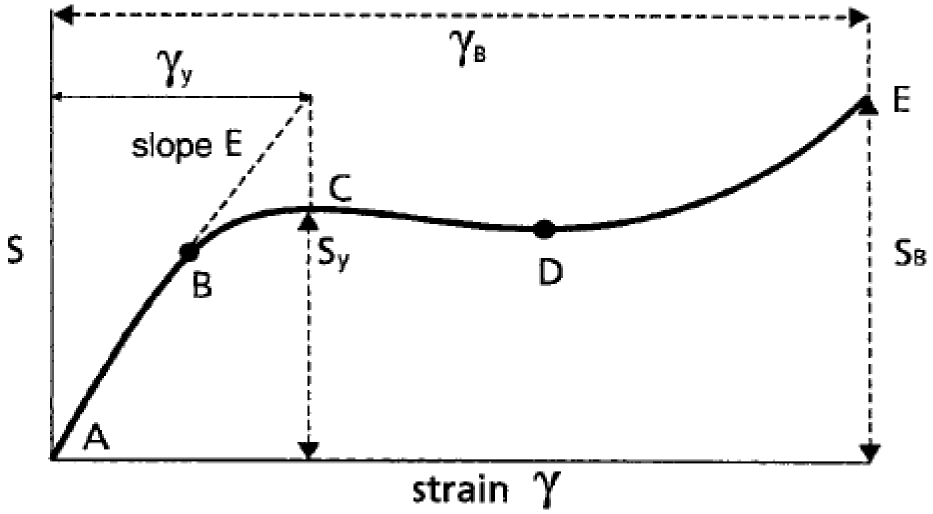

Figure 5.30. Typical stress-strain curve of polymer based materials [74].

There have been numerous studies, micromechanical theories and models developed to predict the strength and elastic modulus of fiber-reinforced composites. Most of them have concentrated to the continuous, unidirectional composites. However, some of them such as Halpin-Tsai model are able to predict the strength of elastic modulus of discontinuous-randomly oriented fiber composites [75, 76].

The Halphin-Tsai equations use the mechanical properties of the fiber and the matrix to calculate the resultant mechanical properties of the composite. The equation can be defined as follows [75-77],

$$\frac{P}{P_m} = \frac{1+\zeta\eta V_f}{1-\eta V_f} \tag{5.5}$$

$$n = \frac{\frac{P_f}{P_m}-1}{\frac{P_f}{P_m}+1} \tag{5.6}$$

In the equations, P corresponds to one of the composite modulus listed in Table 5.10. P_f and P_m correspond to modulus of the fiber and matrix respectively. ζ is a parameter that depends on the particular elastic property which is being considered. [75-77]

Table 5.10. Traditional Halpin-Tsai parameters for short-fiber composites [75]

P	P_f	P_m	ζ	**Comments**
E_{11}	E_f	E_m	$2(l/d)$	Longitudinal modulus
E_{22}	E_f	E_m	2	Transverse modulus
G_{12}	G_f	G_m	1	Longitudinal shear modulus

(l/d is the fiber aspect ratio)

Depending on the predictions of E_{11} and E_{22}, theories were planned to predict the modulus of the random fiber composite which is used the same fiber/resin and had the same fiber volume fraction [75-77].

Nielson et al. [78] modified the Halpin-Tsai model to predict the modulus and the strength of randomly oriented discontinuous fiber composites as follows

$$E_c = E_m\left(\frac{1+A\eta V_f}{1-n\psi V_f}\right) \tag{5.7}$$

$$T_c = T_m\left(\frac{1+A\eta^o V_f}{1-n^o\psi V_f}\right) \tag{5.8}$$

$$\psi = 1+\left(\frac{1+\phi_{\max}}{\phi_{\max}^2}\right)V_f \tag{5.9}$$

$$A = K - 1 = 2l/d \tag{5.10}$$

$$K = 1 + 2l/d \tag{5.11}$$

$$\eta = \frac{E_f / E_m - 1}{E_f / E_m + A} \tag{5.12}$$

$$\eta^o = \frac{T_f / T_m - 1}{T_f / T_m + A} \tag{5.13}$$

In the equations, E_c, E_f and E_m are the modulus of the composite, fiber and matrix respectively. T_c, T_f and T_m are the strength of the composite, fiber and the matrix respectively. Equation (5.9) and Equation (5.10) include the parameter $\phi_{\max}$, which is the maximum packing fraction of the reinforcement. For random packing of fibers, $\phi_{\max}$ =0.82. Aspect ratio has very significant effect on the elastic modulus of the resultant composites even at low volume fraction of the filler [75-77].

5.3.1. Shape Effect of Diatom Frustule Filling on Mechanical Properties

The compression test results of 6 wt% *Achnanthes taeniata* frustule filled epoxy samples showed higher mechanical properties than unfilled epoxy samples. Compressive strength of the material increased to approximately 33%. Also, modulus of elasticity increases with this filling due to the matrix strengthening. Porosity of diatom plays big role in the mechanical properties of resultant composites. Matrix penetration into the porous frustules and the interaction of pores and matrix provides mechanical gripping. Thus, mechanical gripping is mainly responsible for the strength increase. According to the Figure 5.24, it can be said that diatom frustules are well distributed on the matrix. Pores on the walls of diatom frustules are filled with epoxy matrix. Agglomeration of diatom frustules did not occur in these samples. Thus, homogeneity in the distribution was provided. According to SEM fractographs of 6 wt% *Achnanthes taeniata* frustule filled epoxy, interfacial debonding and fracture of the frustules occur and in these samples. In the debonding region, local stresses increased and therefore, it can be said that stress had transferred to the filler from matrix. Because, high stiffness and high aspect ratio of frustules performed high debonding stress, so frustules took the stress from the matrix [79, 80]. Quick proof of debonding in composites is shown in Figure 5.31.

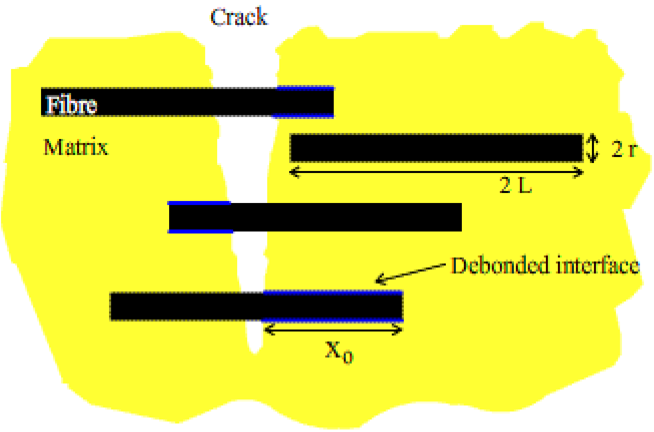

Figure 5.31. Debonding in composites fracture [81] (r: fiber radius, L: fiber length, x_0: debonded interface).

Shape effect of diatom frustule filling on epoxy were provided experimentally by the comparison of the compression test results of *Achnanthes Taeniata* frustule filled epoxy samples and commercial diatomite filled epoxy samples with the same filling amount. *Achnanthes Taeniata* frustules, which are pennate type diatoms, have homogeneous geometry and almost same aspect ratio. As-received commercial diatomite is composed of different types of diatoms which are the mixture of pennate and centric type diatoms and as a result of that, geometry of these diatoms can be thought as non-homogeneous. According to Figure 5.23, *Achnanthes Taeniata* frustule filled epoxy samples presented better mechanical properties than commercial diatomite filled epoxy samples with the same filling amount. The reason is that Achnanthes *Taeniata* frustules are almost same aspect ratio and their geometry is considered as homogeneous. Their short fiber shape, which is due to being pennate diatoms, might affect the mechanical properties positively. They might behave like discontinuous random-oriented fiber reinforcement. Also, planar randomly oriented frustules might affect the mechanical properties positively in the compression axis (see Figure 5.24). Commercial diatoms have non-homogeneous geometry and their aspect ratio is varying. Hence, their effect was found to be lesser than Achnanthes *Taeniata* frustules on epoxy matrix.

As a result, shape effect of diatoms on the mechanical properties of epoxy matrix composite was provided with the comparison of the different types of diatoms with the same quantity of filling. Ahmad et al [23] studied the effect of particle shape of silica structures on the mechanical properties of epoxy composites. Different filler shapes with same chemical structure present different mechanical properties on matrix material.

As a future study, *Achnanthes Taeniata* frustules can be preferentially aligned to the load direction and maximum strength can be provided in this direction. A new research subject would be about how this alignment occurs. Also, higher filling ratio of *Achnanthes Taeniata* frustules can be tried on epoxy matrices with the increasing of the diatom biomass production.

5.3.2. Heat Treatment Effect of Diatomite Filling

Whole heat treated commercial diatomite powders affected the mechanical properties of epoxy composites positively. Matrix penetration into the porous frustules and the interaction of pores and matrix provides mechanical gripping in these composites too. According to the compression tests of these samples, heat treatment at 800^{o}C and 900^{o}C gave rise to the compressive strength and elastic modulus. Heat treatment at 1000^{o}C of diatomite presented highest mechanical properties due to the crystal structure change of the diatomite powder (see Figure 5.26). The reason is that complete crystallization of diatom frustules might affect the interfacial properties by increasing the surface roughness and surface energy of diatom frustules with heat treatment. Therefore, good interaction of matrix and filler affected mechanical properties positively [27]. According to the Figure 5.27, this heat treatment of diatom frustules at 1000^{o}C increased compressive strength by 50%. Also, elastic modulus, failure strain and failure strength increased. Thus, it can be said that the resultant material is tougher than the unfilled epoxy samples. Heat treatment at 1100^{o}C and 1200^{o}C has lesser effect on the mechanical properties due to the collapsed pores of the frustule after the heat treatment at 1100^{o}C and 1200^{o}C (see Figure 5.27-d). Collapsed pores, which are due to the melting of frustule surface, might prevent the mechanical gripping on the frustules surface. Thus, compressive strength slightly decreased after the heat treatment at 1000^{o}C. Also, increased amount of cristobalite phase might be the reason the lower strength of frustules heat treated above 1000^{o}C [82].

According to the SEM images of polished surfaces of heat treated diatomite filled epoxy matrices, it can be said that whole heat treated frustules are well distributed on the matrix and agglomeration did not observed.

According to the SEM fractographs of heat treated diatomite, interfacial debonding and crushing of frustules can be seen. Crack propogation on the frustules (see Figure 5.29), might be evidence that stress is transferred from matrix to filler material. Also, the surface of the frustules is filled with matrix material in the heat treatments at 800,900 and 1000^{o}C so good filler and matrix adhesion can be thought from this situation. Frustules are completely crushed in the heat treated sample at 1100 and 1200^{o}C due to the fact that frustules become brittle in these temperature. Also, the matrix and filler adhesion is not as good as heat treatment at 1000^{o}C due to the collapsed pores of the frustules heat treated at 1200^{o}C.

As a result of this study, heat treatment of diatom frustules is an effective way to increase the mechanical properties of epoxy composites. Heat treatment at 1000^{o}C was found to be the most suitable temperature for this study. As a future work, high strain rate mechanical behavior of heat treated samples can be tested.

CHAPTER 6

CONCLUSIONS

The effect of diatom frustule shape on the compression mechanical properties of epoxy matrix was determined. Pennate diatoms, in various fiber geometries, were used as filler. The effect of heat treatment on the mechanical properties was also investigated. For that, a commercial diatomite was heat treated at different temperatures to increase the crystallinity. Basic materials characterization techniques including SEM, XRD, XRF and FTIR were used to characterize the diatom frustules. The effect of the diatom frustule addition on the mechanical behavior of the filled matrix was determined through quasi-static compression tests. Followings are concluded,

1. Two different cleaning routes, heat treatment and nitric acid digestion, were applied to the diatom biomass. The nitric acid digestion was found to be appropriate for the cleaning cultured diatoms.
2. The results showed that heat treatment of *Pseudo-nitzschia delicatissima* diatom frustules could be used for the production of nano sized SiO_2 powder from diatom frustules.
3. The XRD, XRF, SEM and FT-IR analyses of *Pseudo-nitzschia delicatissima, Achnanthes taeniata, Amphora coffeaeformis* and *Cylindrotheca closterium* after nitric acid digestion were found to be closely matched with those published in the literature.
4. The amorphous to crystalline transition temperature of the heat treated natural diatomaceous earth was determined as 1000^oC by XRD spectra of the diatoms heat-treated between 600 and 1200^oC.
5. The heat treatment of natural diatomaceous earth material between 1100 and 1200^oC resulted in the reduced surface area and the agglomeration of the powder.
6. The filling epoxy matrix with natural commercial diatomite *and Achnanthes taeniata* frustule with ~6 wt% increased the compressive strength from about 60

MPa to 67 and 79 MPa on the average, respectively. A higher strengthening ~10 MPa, and moduli with *Achnanthes taeniata* frustule addition was detected.

7. Polished surfaces of *Achnanthes taeniata* frustule filled epoxy matrix composite samples revealed that frustules were nearly randomly distributed on the plane. The long axes of the frustules were mostly normal to the compression axis, showing nearly planar random orientation. Both fractured and debonded frustules were seen in the fracture surfaces.
8. Heat treatment at 800^{o}C had no significant effect on the stress-strain behavior of the natural diatomite filled matrices, while heat treatment at 900^{o}C increased the stress values of the filled epoxy matrices, without any significant effect on the compressive strength. The heat treatment of natural diatomite frustules at 1000^{o}C increased both compressive strength and stress values of the epoxy matrices. The compressive strength increased from 60 to 90 MPa with the heat-treatment, providing 50% of increase in the compressive strength of neat epoxy. On the other side, the compressive strength decreased with increasing heat treatment temperature after 1000^{o}C.
9. The epoxy infiltrated efficiently through the pores of the frustules. The frustules heat treated between 800 and 1000^{o}C fractured into few pieces, while frustules heat treated at 1100 and 1200^{o}C fractured into many pieces in the filled composites.

REFERENCES

[1] E. Agnantopoulou, V. Tserki, S. Marras, J. Philippou, and C. Panayiotou, "Development of biodegradable composites based on wood waste flour and thermoplastic starch," *Journal of Applied Polymer Science,* vol. 126, pp. E272-E280, Oct 2012.

[2] C. Way, K. Dean, D. Y. Wu, and E. Palombo, "Biodegradation of sequentially surface treated lignocellulose reinforced polylactic acid composites: Carbon dioxide evolution and morphology," *Polymer Degradation and Stability,* vol. 97, pp. 430-438, Mar 2012.

[3] M. W. Chai, S. Bickerton, D. Bhattacharyya, and R. Das, "Influence of natural fibre reinforcements on the flammability of bio-derived composite materials," *Composites Part B-Engineering,* vol. 43, pp. 2867-2874, Oct 2012.

[4] S. Rao, K. Jayaraman, and D. Bhattacharyya, "Micro and macro analysis of sisal fibre composites hollow core sandwich panels," *Composites Part B-Engineering,* vol. 43, pp. 2738-2745, Oct 2012.

[5] H. N. Dhakal, Z. Y. Zhang, N. Bennett, and P. N. B. Reis, "Low-velocity impact response of non-woven hemp fibre reinforced unsaturated polyester composites: Influence of impactor geometry and impact velocity," *Composite Structures,* vol. 94, pp. 2756-2763, Sep 2012.

[6] D. A. B. Strong, *Fundamentals of Composites Manufacturing: Materials, Methods and Applications*, 1st ed.: Society of Manufacturing, 1989.

[7] A. Moropoulou, A. Bakolas, and S. Anagnostopoulou, "Composite materials in ancient structures," *Cement and Concrete Composites,* vol. 27, pp. 295-300, 2005.

[8] A. S. Hemdan Abou-Taleb, "Low Velocity Impact of Composite Crop Straw Panels," *AUTEX Research Journal,* vol. 9, pp. 21-28, 2009.

[9] J. Wadsworth and D. R. Lesuer, "Ancient and modern laminated composites — from the Great Pyramid of Gizeh to Y2K," *Materials Characterization,* vol. 45, pp. 289-313, 2000.

[10] N. S. David Hon, *Wood and cellulose chemistry*, 2 ed.: New York: Marcel Dekker, 2001.

[11] T. Johnson. (2012). *History of Composites*. Available: http://composite.about.com/od/aboutcompositesplastics/a/HistoryofComposites.htm

[12] (2012). *Glass Fibers*. Available: http://en.wikipedia.org/wiki/File:Glasfaser_Roving.jpg

[13] C. University. (2010). *Introduction to Composites*. Available: http://www.mrl.columbia.edu/ntm/level1/ch05/html/l1c05s03.html

[14] D. Kopeliovich. (2012). *Polymer Matrix Composites (Introduction)*. Available: http://www.substech.com/dokuwiki/doku.php?id=polymer_matrix_composites_introduction

[15] H. Ku, H. Wang, N. Pattarachaiyakoop, and M. Trada, "A review on the tensile properties of natural fiber reinforced polymer composites," *Composites Part B: Engineering,* vol. 42, pp. 856-873, 2011.

[16] R. B. Seymour, *Polymer Composites*: VSP, 1990.

[17] S. R. a. S. P. Ltd. (2012). *Reinforcement Types*. Available: http://www.rapra.net/composites/material-selection/reinforcement-types.asp

[18] (2012). *Glass Fiber Reinforced Structural Profiles*. Available: http://www.fibergrate.com/frp-products/dynaform-structural-shapes.aspx

[19] (2012). *Carbon Fiber Reinforced Left Side Automobile Engine Cover* Available: http://www.pureperformancecycles.com/Brand/Ducati/Ducati-Monster/Carbon-Fiber/Sato-Left-Side-Engine-Cover-Monster---S2R--SS

[20] (2012). *Carbon Fiber Reinforced Mobile Phone Case*. Available: http://www.zazzle.com/carbon_fiber_reinforced_polymer_iphone_5_cover-179039128905320755

[21] (2012). *Blackbird Guitar Models*. Available: http://www.blackbirdguitar.com/models.html

[22] S. Ahmed and F. R. Jones, "A review of particulate reinforcement theories for polymer composites," *Journal of Materials Science,* vol. 25, pp. 4933-4942, 1990.

[23] F. N. Ahmad, M. Jaafar, S. Palaniandy, and K. A. M. Azizli, "Effect of particle shape of silica mineral on the properties of epoxy composites," *Composites Science and Technology,* vol. 68, pp. 346-353, 2008.

[24] T. T. Erik and C. Tsu-Wei, "On the elastic properties of carbon nanotube-based composites: modelling and characterization," *Journal of Physics D: Applied Physics,* vol. 36, p. 573, 2003.

[25] F. H. Gojny, M. H. G. Wichmann, U. Köpke, B. Fiedler, and K. Schulte, "Carbon nanotube-reinforced epoxy-composites: enhanced stiffness and fracture toughness at low nanotube content," *Composites Science and Technology,* vol. 64, pp. 2363-2371, 2004.

[26] Y. J. Shi, X. Feng, H. Y. Wang, C. Liu, and X. H. Lu, "Effects of filler crystal structure and shape on the tribological properties of PTFE composites," *Tribology International,* vol. 40, pp. 1195-1203, 2007.

[27] O. Peitl, R. L. Oréfice, L. L. Hench, and A. B. Brennan, "Effect of the crystallization of bioactive glass reinforcing agents on the mechanical properties of polymer composites," *Materials Science and Engineering: A,* vol. 372, pp. 245-251, 2004.

[28] M. Xanthos, "Polymers and Polymer Composites," in *Functional Fillers for Plastics*, ed: Wiley-VCH Verlag GmbH & Co. KGaA, 2005, pp. 1-16.

[29] R. N. Rothon, *Particulate Fillers for Polymers*: Rapra Technology, 2001.

[30] F. P. La Mantia and M. Morreale, "Green composites: A brief review," *Composites Part A: Applied Science and Manufacturing,* vol. 42, pp. 579-588, 2011.

[31] S. V. Joshi, L. T. Drzal, A. K. Mohanty, and S. Arora, "Are natural fiber composites environmentally superior to glass fiber reinforced composites?," *Composites Part A: Applied Science and Manufacturing,* vol. 35, pp. 371-376, 2004.

[32] P. Wambua, J. Ivens, and I. Verpoest, "Natural fibres: can they replace glass in fibre reinforced plastics?," *Composites Science and Technology,* vol. 63, pp. 1259-1264, 2003.

[33] M. Amar, M. Manjusri, D. Lawrence, S. Susan, H. Bruce, and H. Georg, "Natural Fibers, Biopolymers, and Biocomposites," in *Natural Fibers, Biopolymers, and Biocomposites*, ed: CRC Press, 2005.

[34] G. Koronis, A. Silva, and M. Fontul, "Green composites: A review of adequate materials for automotive applications," *Composites Part B: Engineering*.

[35] S. Marais, F. Gouanvé, A. Bonnesoeur, J. Grenet, F. Poncin-Epaillard, C. Morvan, and M. Métayer, "Unsaturated polyester composites reinforced with flax fibers: effect of cold plasma and autoclave treatments on mechanical and permeation properties," *Composites Part A: Applied Science and Manufacturing,* vol. 36, pp. 975-986, 2005.

[36] B. Singh, M. Gupta, and A. Verma, "Influence of fiber surface treatment on the properties of sisal-polyester composites," *Polymer Composites,* vol. 17, pp. 910-918, 1996.

[37] A. Falciatore and C. Bowler, "Revealing the molecular secrets of marine diatoms," *Annu Rev Plant Biol,* vol. 53, pp. 109-130, 2002.

[38] R. Gordon and J. Parkinson, "Potential roles for diatomists in nanotechnology," *Journal of nanoscience and nanotechnology,* vol. 5, pp. 35-40, 2005.

[39] D. P. Allison, Y. F. Dufrêne, M. J. Doktycz, and M. Hildebrand, "Chapter 4 Biomineralization at the Nanoscale: Learning from Diatoms," in *Methods in Cell Biology*. vol. Volume 90, P. J. Bhanu, Ed., ed: Academic Press, 2008, pp. 61-86.

[40] (2012, 10/08). *Diatoms*. Available: http://www.sms.si.edu/irlspec/phyl_chryso1.htm

[41] U. o. California. (2012, 10/08). *Diatoms*. Available: http://earthguide.ucsd.edu/diatom/d3b.html

[42] T. Fuhrmann, S. Landwehr, M. El Rharbi-Kucki, and M. Sumper, "Diatoms as living photonic crystals," *Applied Physics B: Lasers and Optics,* vol. 78, pp. 257-260, 2004.

[43] C. E. Stickley, J. Pike, and A. Leventer, "Productivity events of the marine diatom Thalassiosira tumida (Janisch) Hasle recorded in deglacial varves from the East Antarctic Margin," *Marine Micropaleontology,* vol. 59, pp. 184-196, 2006.

[44] R. Gordon, D. Losic, M. A. Tiffany, S. S. Nagy, and F. A. S. Sterrenburg, "The Glass Menagerie: diatoms for novel applications in nanotechnology," *Trends in Biotechnology,* vol. 27, pp. 116-127, 2009.

[45] M. Sumper and N. Kroger, "Silica formation in diatoms: the function of long-chain polyamines and silaffins," *Journal of Materials Chemistry,* vol. 14, pp. 2059-2065, 2004.

[46] L. E. Antonides, "Diatomite," *The United States Geological Survey,* pp. 24.1-24.6, 1997.

[47] J. Robert D.Crangle, "Diatomite," *2010 Minerals Yearbook,* vol. September 2011, pp. 22.1-22.6, 2010.

[48] (2012, 10/09). *Diatomaceous Earth*. Available: http://geopolymerhouses.wordpress.com/2011/06/11/diatomaceous-earth/

[49] (2012, 10/09). *Open pit Mining Area for Diatomacous Earth Production*. Available: http://atshq.org/boards/viewtopic.php?f=23&t=22201&view=next

[50] E. W. Becker, "Micro-algae as a source of protein," *Biotechnology Advances,* vol. 25, pp. 207-210, 2007.

[51] A. Bozarth, U. G. Maier, and S. Zauner, "Diatoms in biotechnology: modern tools and applications," *Applied microbiology and biotechnology,* vol. 82, pp. 195-201, 2009.

[52] M. W. Anderson, S. M. Holmes, N. Hanif, and C. S. Cundy, "Hierarchical Pore Structures through Diatom Zeolitization," *Angewandte Chemie International Edition,* vol. 39, pp. 2707-2710, 2000.

[53] D. Losic, G. Triani, P. J. Evans, A. Atanacio, J. G. Mitchell, and N. H. Voelcker, "Controlled pore structure modification of diatoms by atomic layer deposition of TiO2," *Journal of Materials Chemistry,* vol. 16, pp. 4029-4034, 2006.

[54] A. S. Abd-El-Aziz, C. E. Carraher, C. U. Pittman, and M. Zeldin, *Macromolecules Containing Metal and Metal-Like Elements, Group IVA Polymers*: Wiley, 2005.

[55] D. Losic, J. G. Mitchell, and N. H. Voelcker, "Diatomaceous Lessons in Nanotechnology and Advanced Materials," *Advanced Materials,* vol. 21, pp. 2947-2958, 2009.

[56] A. Taşdemirci, S. Yüksel, D. Karsu, E. Gültürk, I. W. Hall, and M. Güden, "Diatom frustule-filled epoxy: Experimental and numerical study of the quasi-static and high strain rate compression behavior," *Materials Science and Engineering: A,* vol. 480, pp. 373-382, 2008.

[57] M. C. Bridoux, R. G. Keil, and A. E. Ingalls, "Analysis of natural diatom communities reveals novel insights into the diversity of long chain polyamine (LCPA) structures involved in silica precipitation," *Organic Geochemistry,* vol. 47, pp. 9-21, 2012.

[58] (2012, 11/08/2012). *Chemical Composition of Particulate and Macromolecular Dissolved Organic Matter in the Delaware Estuary and Experimental Diatom Blooms: Sources and Reactivity Patterns*. Available: http://www.cbl.umces.edu/~harvey/MOGEL/delaware.htm

[59] D. B. Sirdeshmukh, L. Sirdeshmukh, and K. G. Subhadra, *Alkali halides : a handbook of physical properties ; with 202 tables*. Berlin [u.a.]: Springer, 2001.

[60] M. A. Shand, *The Chemistry and Technology of Magnesia*: Wiley, 2006.

[61] C. o. W. T. Chemicals, Food, N. Board, A. o. L. Sciences, and N. R. Council, *Water Chemicals Codex*: The National Academies Press, 1982.

[62] (1985, 11/08). *Silicon Dioxide, Amorphous*. Available: http://www.fao.org/ag/agn/jecfa-additives/specs/Monograph1/Additive-385.pdf

[63] C. T. Reviews, *e-Study Guide for: Chemical Principles, Enhanced Edition by Steven S. Zumdahl, ISBN 9781439043981*: Cram101, 2012.

[64] S. M. Méndez, M. Ferrario, and A. O. Cefarelli, "Description of toxigenic species of the genus Pseudo-nitzschia in coastal waters of Uruguay: Morphology and distribution," *Harmful Algae,* vol. 19, pp. 53-60, 2012.

[65] M. Schmidt, R. Botz, D. Rickert, G. Bohrmann, S. R. Hall, and S. Mann, "Oxygen isotopes of marine diatoms and relations to opal-A maturation," *Geochimica et Cosmochimica Acta,* vol. 65, pp. 201-211, 2001.

[66] M. G. E.Gulturk, "Thermal and acid treatment of diatom frustules," *Journal of Achievements in Materials and Manufacturing Engineering,* vol. 46/2, pp. 196-203, 2011.

[67] (2000, 11/08). *Diatom Image Database*. Available: http://fcelter.fiu.edu/data/database/diatom/index.htm?species=3416

[68] A. Alvarez-Ordonez and M. Prieto, "Changes in ultrastructure and Fourier transform infrared spectrum of Salmonella enterica serovar typhimurium cells after exposure to stress conditions," *Appl Environ Microbiol,* vol. 76, pp. 7598-607, Nov 2010.

[69] M. Hoppenrath. (2012, 11/08). *Cylindrotheca closterium (Ehrenberg) Reimann and J.C Lewin, 1964*. Available: http://planktonnet.awi.de/index.php?contenttype=image_details&itemid=13662#content

[70] U. S. E. P. Agency. (2012, 11/01). *Diatomite Processing*. Available: http://www.epa.gov/ttnchie1/ap42/ch11/final/c11s22.pdf

[71] K. Rangsriwatananon, A. Chaisena, and C. Thongkasam, "Thermal and acid treatment on natural raw diatomite influencing in synthesis of sodium zeolites," *Journal of Porous Materials,* vol. 15, pp. 499-505, 2008/10/01 2008.

[72] P. W. Xiao WS, Wang GX, Wang FY, Weng KN, "Infrared spectroscopic study of Changbaishan diatomite," *Spectroscopy and Specrtal Analysis,* vol. 24, pp. 690-693, 2004.

[73] A. S. S.Ibrahim, "Heat Treatment of Natural Diatomite," *Physochemical Problems of Mineral Processing,* vol. 48, pp. 413-424, 2012.

[74] A. Ram, *Fundamentals of Polymer Engineering*: Springer, 1997.

[75] J. C. Halpin, "Stiffness and Expansion Estimates for Oriented Short Fiber Composites," *Journal of Composite Materials,* vol. 3, pp. 732-734, October 1, 1969 1969.

[76] J. C. Halpin and K. M. Finlayson, *Primer on Composite Materials Analysis, Second Edition (Revised)*: CRC PressINC, 1992.

[77] Y. Lu, "Mechanical Properties of Random Discontinuous Fiber Composites Manufactured from Wetlay Process," Master of Science, Engineering Mechanics, Virginia Polytechnic Institute and State University, 2002.

[78] L. E. Nielsen, *Mechanical properties of polymers*: Van Nostrand Reinhold, 1962.

[79] S. Ghosh, Y. Ling, B. Majumdar, and R. Kim, "Interfacial debonding analysis in multiple fiber reinforced composites," *Mechanics of Materials*, vol. 32, pp. 561-591, 2000.

[80] J. K. Wells and P. W. R. Beaumont, "Debonding and pull-out processes in fibrous composites," *Journal of Materials Science*, vol. 20, pp. 1275-1284, 1985/04/01 1985.

[81] (2012, 11/09). *Interfacial Debonding*. Available: http://www.doitpoms.ac.uk/tlplib/fibre_composites/interfacial_debonding.php

[82] J. P. Nayak and J. Bera, "Effect of sintering temperature on phase-formation behavior and mechanical properties of silica ceramics prepared from rice husk ash," *Phase Transitions*, vol. 82, pp. 879-888, 2009/12/01 2009.